UNIVERSIDAD DE CHILE

FACULTAD DE CIENCIAS FÍSICAS Y MATEMÁTICAS

DEPARTAMENTO DE INGENIERÍA ELÉCTRICA

IDENTIFICATION OF WEAK AREAS IN LOW-INERTIA POWER SYSTEMS WITH HIGH SHARES OF CONVERTER-BASED GENERATION

TESIS PARA OPTAR AL GRADO DE MAGÍSTER EN CIENCIAS DE LA INGENIERÍA,MENCIÓN ELÉCTRICA

MEMORIA PARA OPTAR AL TÍTULO DE INGENIERO CIVIL ELÉCTRICO

IGNACIO ANDRÉS PONCE ARANCIBIA

PROFESORA GUÍA:

CLAUDIA RAHMANN ZÚÑIGA

MIEMBROS DE LA COMISIÓN:

RODRIGO PALMA BEHNKE

POUYAN POURBEIK

Este trabajo ha sido parcialmente financiado por:

Agencia Nacional de Investigación y Desarrollo (ANID) a través del proyecto:

Fondecyt Regular N°1201676

SANTIAGO DE CHILE

2022

RESUMEN DE LA TESIS PARA OPTAR AL GRADO DE MAGÍSTER EN CIENCIAS DE LA INGENIERÍA, MENCIÓN ELÉCTRICA y MEMORIA PARA OPTAR AL TÍTULO DE INGENIERO CIVIL ELÉCTRICO.
POR: IGNACIO ANDRÉS PONCE ARANCIBIA
FECHA: 2022
PROFESORA GUÍA: CLAUDIA RAHMANN ZÚÑIGA

IDENTIFICACIÓN DE ÁREAS DÉBILES EN SISTEMAS DE POTENCIA DE BAJA INERCIA CON ALTOS NIVELES DE GENERACIÓN BASADA EN CONVERTIDORES

El reemplazo de generación sincrónica por tecnologías de generación conectadas con convertidores disminuye la robustez de los sistemas de potencia. Diversos desafíos técnicos aparecen con esta evolución, especialmente desde una perspectiva de frecuencia. Particularmente, investigaciones recientes han demostrado que una distribución espacial de la inercia desigual puede deteriorar el RoCoF local e incrementar oscilaciones locales de frecuencia. En este contexto, identificar áreas débiles de frecuencia surge como una tarea de seguridad críticia para superar estos problemas.

Esta tesis propone una herramienta offline capaz de identificar automáticamente áreas débiles de frecuencia a partir de la información del despacho. Para esto, se ha implementado una metodología de seis etapas en el Sistema Eléctrico Nacional chileno. El desarrollo involucra primero identificar áreas coherentes de frecuencia y luego cuantificar su nivel de robustez a través del índice LEEII, que considera la distribución espacial de la inercia.

Los resultados evidencian un correcto desempeño del LEEII y validan la herramienta propuesta. Además, se han derivado condiciones que podrían derivar en una activación indeseada de protecciones en términos de la métrica propuesta. En el caso del sistema y condiciones analizadas, un valor mínimo del LEEII de 5 s garantiza evitar la aparición de los problemas estudiados.

RESUMEN DE LA TESIS PARA OPTAR AL GRADO DE MAGÍSTER EN CIENCIAS DE LA INGENIERÍA, MENCIÓN ELÉCTRICA y MEMORIA PARA OPTAR AL TÍTULO DE INGENIERO CIVIL ELÉCTRICO.
POR: IGNACIO ANDRÉS PONCE ARANCIBIA
FECHA: 2022
PROFESORA GUÍA: CLAUDIA RAHMANN ZÚÑIGA

IDENTIFICATION OF WEAK AREAS IN LOW-INERTIA POWER SYSTEMSWITH HIGH SHARES OF CONVERTER-BASED GENERATION

The replacement of synchronous generation by converter-interfaced generation technologies decreases power system robustness. Several technical challenges arise with this evolution, especially from a frequency perspective. In particular, recent investigations have demonstrated that an uneven spatial distribution of inertia can significantly deteriorate local RoCoF and increase local frequency oscillations. In this context, identifying weak frequency areas emerges as a critical security task for successfully overcoming the issues that low-inertia power systems may experience.

This thesis proposes an offline tool that automatically identifies weak f-areas from the unit commitment information. A six-stage methodology was successfully implemented to develop the tool in a real power system case: the Chilean NES. The development involves identifying coherent f-areas and then quantifying its f-robustness level through the novel LEEII index that considers the spatial distribution of the inertia.

The results show the correct performance of the LEEII index and validate the proposed solution. Further, conditions by which the system can fall into undesirable activation of protections have been derived from the proposed metric. In the case of the analyzed system and conditions, a minimum LEEII value of 5 s guarantees avoiding the studied issues.

Para mi familia, mis amigos y en especial, Moira.

Agradecimientos

En primer lugar, me gustaría agradecer a mi familia más cercana, mi padre, mi madre y mi hermana, que me han brindado un incondicional apoyo desde siempre. Estoy profundamente agradecido por haberme inculcado los valores que me han permitido crecer y desarrollarme a todo nivel. Siento enorme admiración por el esfuerzo, disciplina y alegría que me han transmitido desde niño y que les han permitido alcanzar sus sueños. Espero poder retribuir todo lo que me han entregado.

También quiero agradecer a quienes me han acompañado en esta aventura. En primer lugar, a mis amigos del colegio, que han sido fundamentales durante mi crecimiento y maduración. En segundo lugar, a profesores clave de la enseñanza media que comenzaron a despertar mi pasión por la matemática y el campo de la ingeniería, especialmente a los profesores Camus de matemática y Mariani de física.

Imposible no destacar al excepcional grupo de amigos que tuve el privilegio y la suerte de encontrar en los primeros días de universidad. Bruno, Piero, Andrés y Chris, no me imagino la experiencia de la universidad sin ustedes, muchas gracias por su compañía y espero que nuestra amistad perdure por siempre. También quiero destacar a los amigos que me acompañaron en eléctrica, en especial a Pancho, Mati y Joseph, cuyo apoyo y amistad ha tenido un enorme valor durante esta etapa final.

Quisiera agradecer de forma muy especial a Moira, quien llegó inesperadamente a mi vida en los primeros años de universidad y ha sido la mejor compañera de vida desde entonces. Te agradezco muchísimo por haber sido mi soporte incondicional en momentos malos y buenos de este proceso. A pesar de la enorme dificultad y carga del último tiempo, hemos sabido mantener el balance y apoyarnos mutuamente. Estoy seguro de que juntos llegaremos al final de esta etapa y podremos contar con el otro en los emocionantes desafíos que se nos vienen en adelante.

Agradezco también a las excelentes personas que me he encontrado en mi primera experiencia laboral. Su profesionalismo y excelencia han contribuido mucho a mi desarrollo y estaré siempre muy agradecido por la flexibilidad y oportunidad que me brindaron. Mención especial para Bernal, que siempre demostró una voluntad extraordinaria para enseñarme y apoyarme en lo que necesitara.

Por último, quisiera agradecer a quien ha sido el pilar de mi desarrollo académico en los últimos años. A la profesora Claudia, quien desde su primer curso despertó en mí un gran interés por el campo de investigación en sistemas de potencia, y que por supuesto, bajo la guía de esta tesis, ha sido fundamental para llevar a cabo esta investigación. Muchas gracias profe por la excepcional dedicación que tuvo conmigo, y me consta, que lo tiene en general con sus alumnos. Espero que en el futuro volvamos a trabajar juntos.

Agracezco el apoyo brindado por ANID financiando parcialmente esta investigación a través del proyecto Fondecyt Regular N°1201676.

Table of Contents

List of Tables

List of Figures

1 Introduction

1.1 Motivation

Motivated by environmental goals, consistent tech development, and cost reduction, the energy matrices of bulk power systems (BPSs) around the globe are relegating its coal-based generation in favor of renewable energy sources (RESs). The total installed capacity of solar photovoltaics has increased from 40 GW to 700 GW in the last decade [1]. Wind energy has increased from 180 GW to 730 GW in the same period [2]. This transition has been followed by introducing new technologies to BPS, including storage systems, FACTS devices, distributed energy resources (DERs), HVDC transmission lines, among other power electronic interfaced devices.

The transition mentioned above is changing how BPSs are designed, planned, controlled, and operated. From the control and operation point of view, as more converter interfaced devices are being connected to BPSs, its control architecture becomes more complex since many different control mechanisms must be coordinated and managed [3]. Additionally, several technical challenges arise with this evolution, especially from a frequency perspective. They come from the difference in the dynamic behavior between converter interfaced generation technologies (CIGTs) and conventional synchronous generation facilities. Further, CIGTs are usually controlled to inject their maximum available active power into the grid. This configuration means that they do not keep power reserves to maintain the power balance in the system during normal operating conditions. On the other hand, CIGTs do not naturally provide inertial response to the system as the conventional synchronous generators (SGs) do [3][4].

The replacement of conventional SGs by inertia-less CIGTs can deteriorate both system frequency control and inertial response, which significantly worsens the dynamic behavior of the system frequency [3][4]. This problem can be especially critical in the case of small islanded systems, where inertia is already low. In such a scenario, after the loss of a generating unit, the Rate of Change of Frequency (RoCoF) becomes steeper and the frequency nadir lower. Consequently, the frequency dynamic becomes faster, resulting in more frequent and deeper excursions following a sudden power imbalance. These consequences increase the likelihood of experiencing frequency instabilities and triggering Under Frequency Load Shedding Schemes (UFLSSs) [3][4]. Although CIGTs do not naturally provide inertial response, additional control loops can be implemented in the converters to counteract this problem. They must be specifically designed to force the electronic power converters to react to frequency variations [9][10]. These particular configurations allow CIGTs to provide Fast Frequency Response (FFR) to support the grid during significant power imbalances as SGs do [10]. Up to date, these control strategies are based on the traditional (well-known) post-fault frequency behavior using local measurements, mainly the voltage reference to synchronize their controllers and estimate the frequency through a Phase Locked Loop (PLL), which has been used as the main control signal to reflect the active power balance of the BPS. These approaches may successfully overcome compromising situations regarding frequency stability in traditional SG-dominated BPSs [11]. However, future CIGTs-dominated BPSs will have less stable voltage references, faster dynamics, and more complex control mechanisms, meaning similar frequency dynamics should not be expected [3]. Accordingly, traditional decentralized and uncoordinated frequency control strategies using local feedback may become too slow for preventing large frequency deviations in future power systems [6]

In addition, some researchers have demonstrated that in future CIGTs-dominated BPSs, the spatial distribution of the inertia strongly influences the post fault local frequency dynamics and not only the total system inertia [6][7]. Uneven spatial distributions of inertia can significantly deteriorate local RoCoF, increase local frequency oscillations, and provoke undesirable control interactions [7]. Thus, there is a paradigm change since frequency control strategies assume the frequency is a whole system variable. Since hydro power plants will probably remain in future BPSs as the main synchronous generation technology, inertia will be highly concentrated according to the locations of hydro resources [3]. This is the expected scenario for 2050 in the Chilean National Electricity System, a highly longitudinal and low-meshed system, where photovoltaic and wind power plants will dominate the North and central regions of the country while hydro generation will be concentrated in the South.

In the aforementioned context, wide-area coordinated controllers will become essential for successfully overcoming the control complexities and underlying stability problems that low-inertia power systems may experience. In such an approach, identifying weak frequency areas emerges as a critical security task by facilitating the design and tunning of system frequency controllers in BPSs characterized by an uneven spatial distribution of inertia. Identifying weak areas also supports monitoring the system state in daily operation. This thesis contributes to this critical task by evaluating the following hypothesis and achieving the goals presented afterward.

1.2 Hypothesis

H1: The total inertia of power systems with high levels of CIGTs is not enough as an indicator of frequency performance during contingencies (f-robustness).

H2: Is it possible to define a meaningful index to measure the dynamic frequency performance of f-areas during contingencies.

1.3 General objective

GO: Develop a screening method able to identify weak frequency areas in low-inertia power systems.

1.4 Specific objectives

SO1: Define novel indexes to quantify power system robustness in terms of frequency (f-robustness) considering the spatial distribution of inertia.

SO2: Derive sufficient conditions by which power systems can fall into undesirable activation of RoCoF-based protections as a last resort to prevent system instability in terms of the novel indexes defined.

SO3: Develop an offline tool that, based on the system generation dispatch, can automatically identify weak areas of the system in terms of frequency.

SO4: Validate the proposed tool in a detailed dynamic model of the Chilean National Electricity System for 2022 through time-domain simulations.

This document continues organized as follows: In chapter 2, a detailed theoretical background is included to present the main concepts to fully understand this work and the current research contributions that precede this investigation. In chapter 3, the methodology developed is

described in detail. In chapter 4, the Chilean National Electric System for 2022 is presented as the case study to validate the proposed solution. In chapter 5, the results of the implementation of the methodology on the case study are presented. Finally, in chapter 6, the conclusions of this thesis are announced.

2 Theoretical Background

2.1 Power systems robustness in terms of frequency

In power systems, the term "system robustness" is typically used to roughly characterize the system's dynamic performance under all possible operating conditions. It indicates how well the system can ride through different contingencies and sustain a stable behavior. Since this work focuses on frequency stability, robustness will be used to refer to the ability of a power system to ride through power imbalances and maintain a stable frequency.

To assess the robustness of power systems in terms of their frequency, a review of the dynamic behavior of SGs as the main components affecting frequency performance is presented [11]. SGs rotor speed is proportional to the frequency. Then, the values of electric frequency and speed are the same in per unit. If a machine is running at nominal speed, let's say 3600 revolutions per minute (rpm) for a 2-pole machine, the corresponding stator electric frequency is determined by Faraday's Law, resulting in 60 Hz. If the flux linked to the stator circuits is sinusoidal and has a frequency ω, then the induced voltage will be sinusoidal with frequency ω. In the following sections, a review of the electromechanical equations which describe the dynamics of SGs and the traditional way to quantify systems robustness in terms of frequency is presented.

2.1.1 Swing equation of synchronous generators

The swing equation comes from Newton's Second Law for a rotating mass. In the case of a SG, the rotating mass refers to the rotor. Newton's Law states that the acceleration speed is proportional to the net torque:

$$\mathrm{J} \cdot \frac{\mathrm{d}\omega_\mathrm{m}}{\mathrm{dt}} = \mathrm{T_a} = \mathrm{T_m} - \mathrm{T_e} \qquad (1)$$

where

- J = moment of inertia of the generator and turbine together in $kg \cdot m^2$.
- ω_m = angular speed of the rotor in $mech \cdot \mathrm{rad/s}$.
- t = time in s.
- T_a = accelerating torque in $N \cdot m$.
- T_m = mechanical torque in $N \cdot m$.
- T_e = electromagnetic torque in $N \cdot m$.

The mechanical torque T_m is the input generated by the machine's turbine, and T_e is the output torque which is transformed into electric power by the generator. In steady-state, the rotational speed is constant, implying an equilibrium of torques in the generator's shaft. Otherwise, the difference will generate an accelerating torque T_a.

The above equation can be normalized to get a per-unit representation. This introduces the concept of inertia constant H, defined as the kinetic energy stored in the generator's rotating masses at nominal speed divided by its rated apparent power:

$$H = \frac{1}{2} \cdot \frac{J \cdot \omega_{0m}^2}{S_0} \quad (2)$$

where

- H = per unit inertia constant of the generator in s.
- ω_{0m} = nominal angular speed of the generator in $mech \cdot rad/s$.
- S_0 = rated apparent power of the generator in VA.

The constant *H* represents the time in seconds that a generator can provide its nominal power based on the kinetic energy stored in its rotating masses. Typical ranges for this constant are listed in Table 1.

Type of generator	H [s]
Thermal unit	
3600 r/min (2-pole)	2.5 to 6.0
1800 r/min (4-pole)	4.0 to 10.0
Hydraulic unit	2.0 to 4.0

Table 1: Typical ranges for H constant depending on the generating unit type [11].

In general, thermal units have more prominent inertia constants than hydraulic units because of the shape of the turbines used in each case.

Isolating the moment of inertia J from (2) leads to:

$$J = \frac{2 \cdot H}{\omega_{0m}^2 \cdot S_0} \quad (3)$$

By substituting (3) in (1) and rearranging some terms yields:

$$2 \cdot H \cdot \frac{d}{dt}\left(\frac{\omega_m}{\omega_{0m}}\right) = \omega_{0m} \cdot \frac{T_m - T_e}{S_0} \quad (4)$$

Since $\frac{S_0}{\omega_{0m}}$ corresponds to the torque base T_0, converting (4) to per-unit values leads to:

$$2 \cdot H \cdot \frac{d\overline{\omega_m}}{dt} = \overline{T_m} - \overline{T_e} \quad (5)$$

where

- $\overline{\omega_m}$ = angular speed of the generator in pu.
- $\overline{T_m}$ = mechanical torque in pu.
- $\overline{T_e}$ = electromagnetic torque in pu.

In power systems, it is more desirable to express the above equation in terms of power instead of torque. For this aim, the above equation is multiplied by the angular speed $\overline{\omega_e}$:

$$2 \cdot H \cdot \overline{\omega_e} \cdot \frac{d\overline{\omega_e}}{dt} = \overline{P_m} - \overline{P_e} \quad (6)$$

where

- $\overline{P_m}$ = mechanical power in pu, which is the input of the generator.
- $\overline{P_e}$ = electrical power in pu, which is the output of the generator.

The mechanical angular speed of SGs is proportional to the electrical angular speed or frequency of the balanced three-phase current waves at the stator [11]. Then, both variables are equal in pu. Therefore, the above equation can be expressed in terms of the frequency of the grid:

$$2 \cdot H \cdot \overline{f_e} \cdot \frac{d\overline{f_e}}{dt} = \overline{P_m} - \overline{P_e} \quad (7)$$

where

- $\overline{f_e}$ = frequency of the point of connection to the grid in pu, equal to the electrical angular speed of the generator.

By assuming small deviations around its nominal value, the frequency can be approximated by 1 ($\overline{f_e} \approx 1$), which leads finally to:

$$2 \cdot H \cdot \frac{d\overline{f_e}}{dt} = \overline{P_m} - \overline{P_e} \quad (8)$$

Equation (8) is commonly referred as the "swing equation" of a single SG in per unit. In some cases, it is expressed in terms of the rotor angle δ instead of the frequency f_e. Moreover, a proportional term to frequency deviation can be included to represent a damping component [11].

From (8), it can be noted that for a given power imbalance, the generator's angular speed (or frequency) will change since its derivative will not be null anymore. Moreover, the rate of change of frequency (RoCoF) will be more pronounced for smaller values of H and less pronounced for higher values of H. Equation (8) clearly shows the relevance of the inertia constant as an indicator of the "resistance" of a SG to frequency deviations. Inertia can be used to measure how well the system can ride through power imbalances and still maintain a stable frequency. Therefore, the inertia represents a good indicator of system robustness. The inertial response is naturally provided by the rotating masses of power systems such as SGs and motors. As demonstrated in the next section, the inertia of SGs influences both the activation of Under Frequency Load Shedding Schemes (UFLSS) during contingencies and the performance of the system frequency control in a steady-state (small load/generation fluctuations).

2.1.2 Traditional definition of total inertia of a power system

In traditional large power systems with large amounts of SGs the frequency at different locations is the same in steady-state (without considering transmission constraints). If there is a

load change, generators will react towards the change by adjusting their speeds. However, all speeds should be the same in per unit since they are all electrically interconnected through the transmission system [12]. Thus, it is usually assumed that the frequency is the same at every network busbar in power systems, meaning the frequency is treated as a single state variable of the whole system [11].

The above assumption can determine the Swing equation for a power system composed of N SGs. Since $\overline{f_e}$ is a global system variable, all generators can be aggregated into a single unit, and similarly, all loads into a single demand. Consequently, a single equation to describe the frequency behavior of the whole system can be written as follows:

$$2 \cdot H_{sys} \cdot \frac{d\overline{f_e}}{dt} = \overline{P_g} - \overline{P_l} \quad (9)$$

where

- H_{sys} = total system inertia in s, given by (10).
- $\overline{P_g}$ = total system generation in pu.
- $\overline{P_l}$ = total system load including losses in pu.

The above introduces the key concept of total system inertia, defined as the sum of the kinetic energy stored in all SGs, divided by the total generation capacity connected to the system at some operating point.

$$H_{sys} = \frac{\sum_i^N H_i \cdot S_i}{\sum_i^N S_i} = \frac{\sum_i^N E_i}{S_{sys}} \quad (10)$$

where

- N = number of SGs connected to the system.
- H_i = per unit inertia constant of the generator i in s.
- S_i = rated apparent power of the generator i in VA.
- E_i = kinetic energy stored in the rotating masses of the generator i in J.
- S_{sys} = total generation capacity of the system in VA.

The above definition neglects the inertia of loads and CIGTs since their effects are minimal compared with synchronous inertia's influence. This assumption is usually made when studying conventional (large scale) power systems dominated by SGs.

To summarize, three main assumptions are commonly made when studying the frequency behavior of traditional power systems:

1. Frequency is considered as a single variable at every point of the system

2. Frequency deviations around its nominal value are small, then $\overline{f_e} \approx 1$.

3. Inertia coming from loads and CIGTs is negligible compared with the one from synchronous machines.

2.1.3 Typical response of power systems facing active power imbalances

Power systems are exposed to suffer different events, which can trigger power imbalances. Some examples are the loss of a generation unit or the sudden connection (or disconnection) of large load blocks. In general, it is more critical for a power system to face a generation deficit than an excess of it [11]. This critical case will be referred as a negative power imbalance due to the sign of the right side in the swing equation.

After major power imbalances, the frequency response of a power system can be roughly divided into three main phases: Inertial Response (IR), Primary Frequency Control (PFC), and Secondary Frequency Control (SFC). Depending on the power system or transmission system operator (TSO) involved, other names can be found for the primary and secondary response. Figure 1 shows the relevant time frames involved in each phase of the system frequency response in the case of a generation outage.

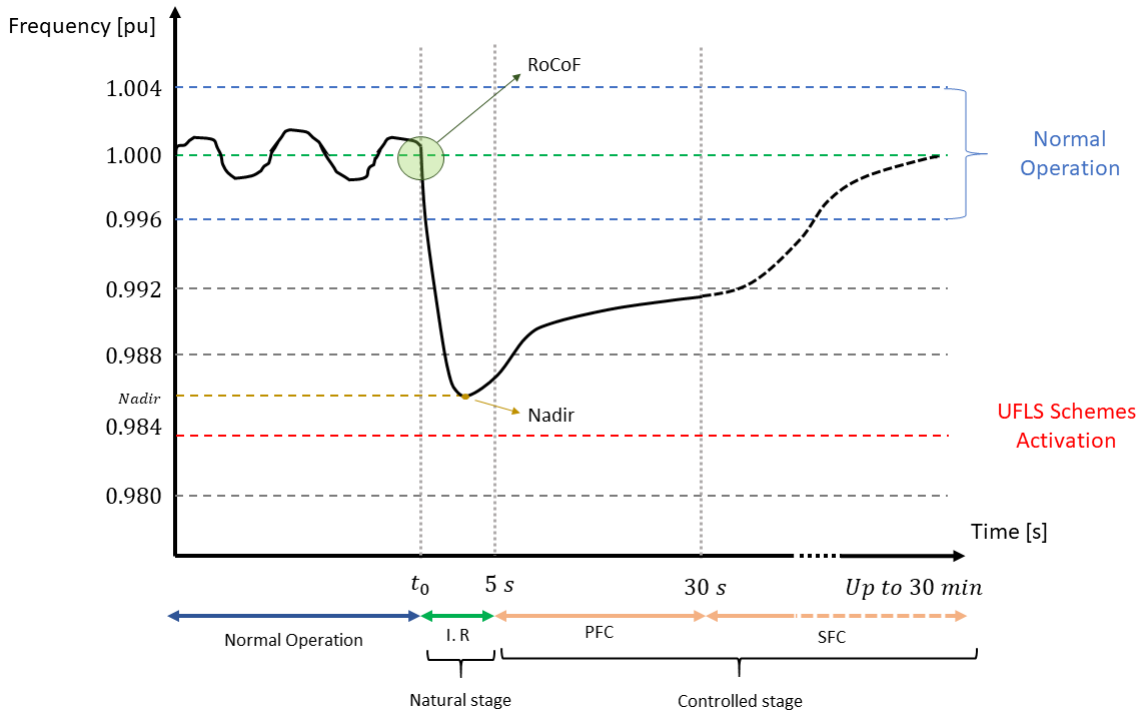

Figure 1: Typical time evolution of the frequency of a traditional large power system under a negative power unbalance.

According to (9), in this case, the system's frequency will start to decrease at a rate mainly determined by the total inertia of the system: the lower the system inertia, the faster the system frequency will decrease. Due to their electromechanical coupling, the rotating masses will inject kinetic energy into the grid for several seconds to counteract the frequency deviation according to their inertia. This natural counter-response from SGs is provided whenever the mismatch between generation and consumption remains. This action renders the system frequency dynamic slower and thus easier to regulate. Thus, the imbalance is initially compensated by extracting kinetic energy from the remaining rotating machines. This natural action is essential to arrest the decline in frequency to prevent the activation of automatic UFLSS. It plays a crucial role in frequency

stability since it determines how fast the frequency will drop after a fault and how easy it will be for the controlled stage to restore normal operation.

Two indexes commonly characterize the system's performance after a negative power imbalance event. First, the "Rate of Change of Frequency" (RoCoF), defined as the rate of variation of the frequency at the beginning of the fault t_0. As seen in (11), the RoCoF depends directly on the system inertia and the magnitude of the power imbalance. The second index is the "frequency nadir," defined as the minimum value of the frequency reached by the system after the fault. It depends on how fast the frequency dropped initially in the inertial response and how effective is the Primary Frequency Control (PFC) action.

$$RoCoF = \frac{d\bar{f}}{dt}(t = t_0) = \frac{\overline{P_g} - \overline{P_l}}{2 \cdot H_{sys}} \quad (11)$$

$$Nadir = min\{\bar{f}(t)\} \quad (12)$$

From (11), it is clear the role of the total system inertia H_{sys} to sustain frequency stability after power imbalances. A low-inertia system is poorly prepared to face a major power imbalance as its frequency will drop very quickly. Moreover, it will reach low frequency nadir values. For that reason, the total system inertia is an indicator widely used for quantifying power system robustness in terms of frequency stability.

Beyond this natural (first) inertial response, primary frequency controls of SGs react by changing the generated power to recover the power balance. After some seconds, the governors of SGs begin to act upon its valves or gates, leading to an increase in the output power of the turbines. SGs will increase their generation until the balance between generation and consumption is restored and the system frequency stabilizes. This second phase is called Primary Frequency Control (PFC), as shown in Figure 1. This response occurs in a time frame from 5 to 30 s, depending on the characteristics of the generation units.

Secondary frequency control is required to restore the frequency back to its nominal value and release the used primary power reserves. As shown in Figure 1, SFC adjusts the power set-point of the generation units, usually controlled through an automatic generation control (AGC). Secondary power reserves are engaged in approximately 30 s after a contingency, and they must be fully operational within 15 min. Once both control actions occur, the system frequency is restored to its nominal value.

2.2 Effects of a high share of CIGTs on frequency of power systems

Due to the physical characteristics of CIGTs and the fact that they are connected through power converters to the system, from a frequency perspective, these power plants behave differently than conventional generation facilities. The main differences are that most CIGTs do not (yet) contribute either to the system frequency regulation or system inertial response. On the one hand, power converters of CIGTs are usually controlled to inject their maximum available active power into the grid, meaning that these power plants do not keep power reserves for helping to sustain the balance between the generated power and demand. On the other hand, CIGTs do not usually provide inertial response to the system as conventional SGs do. In the following subsections, an overview of the main effects of CIGTs in system frequency is presented.

2.2.1 Decreasing system inertia levels

As described in Section 2.1.3, the kinetic energy stored in the rotating masses of SGs is the main contribution to the inertial response in power systems. Since most CIGTs do not naturally contribute to system inertial response, as CIGTs replace SGs, less inertia is available in power systems.

In the case of photovoltaic power plants, they do not have any rotational masses, and there is no stored kinetic energy to be delivered to support the system during a power imbalance. Even though there is some energy stored in the capacitors of the converters, its amount is negligible. In the case of wind power plants, the power converter fully or partly electrically decouples the generator from the grid, which implies that the kinetic energy stored in their moving parts is not used for supporting the frequency unless a specific control is designed for this purpose [4].

Several studies have demonstrated that replacing conventional SGs with inertia-less CIGTs can lead to degradation in both primary frequency response and system inertial response. This can be especially critical in the case of islanded systems and small isolated systems, where the inertia (without CIGTs) is already low.

To illustrate the effects of low inertia levels, Figure 2 shows the frequency behavior of the Continental Europe Power System after a power imbalance of 3 GW for different inertia levels [14]. The figure clearly shows that lower inertia levels (this time described by the acceleration time constant T_N) lead to a worst dynamic performance of the system frequency.

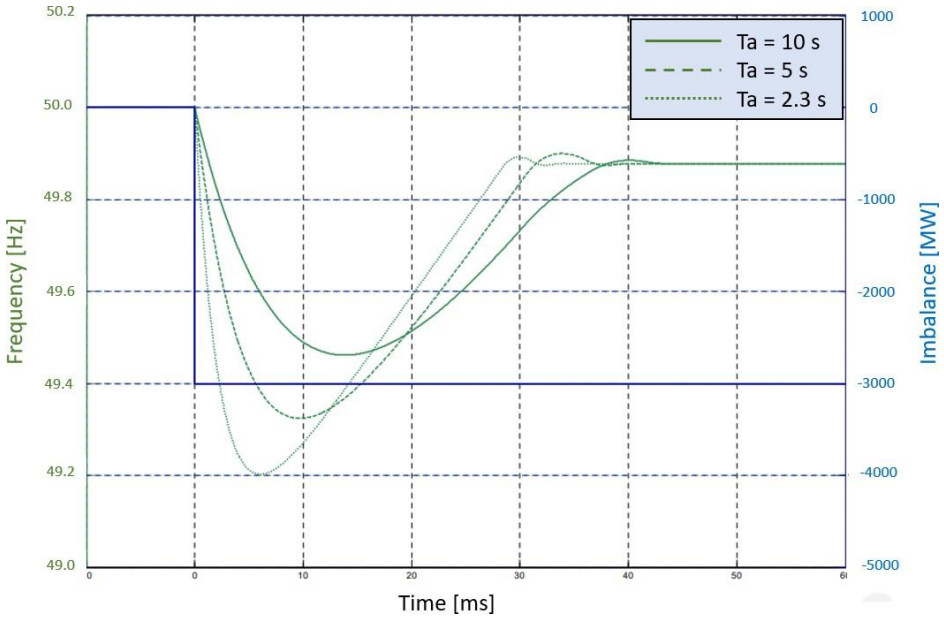

Figure 2: Frequency response for a 3 GW reference incident in the Continental Europe Power System for different inertia levels [14].

2.2.2 Faster frequency dynamics

As previously mentioned, the total system inertia decreases as the use of CIGTs increases. Accordingly, the system frequency response will present steeper RoCoF slopes and lower frequency nadirs. Moreover, as CIGTs increase, frequency behavior will become more dependent on power converters' complex fast electromagnetic phenomena. Consequently, fast interactions between CIGTs and the grid may arise and provoke unstable behaviors [3]. On the one hand, many more but likely smaller contingencies of loss of generation are expected to occur [15]. On the other hand, future power systems are potentially susceptible to even larger faults caused by HVDC lines [16].

As the system frequency response becomes faster, it should not be expected that in CIGTs-dominated power systems, the frequency behavior will still be similar to that shown in Figure 1. On the contrary, it will be characterized by faster and more complex dynamics dominated by different control mechanisms implemented in the power converters of CIGTs [4]. This change can lead to situations where traditional control approaches (PFC) may be too slow to prevent large frequency deviations [6]. Moreover, in the extreme case of a zero-inertia system, the frequency may no longer have a relevant meaning, at least not as an indicator of power balance [3]. In addition, traditional performance indicators such as the RoCoF, frequency nadir, or the total system inertia may not faithfully represent the system frequency dynamics in such scenarios, as shown in [7]. In conclusion, even though for understanding frequency stability in low-inertia systems it may be a good starting point to use (9), a direct extrapolation from the behavior in Figure 1 to low-inertia systems could lead to incorrect conclusions [3].

2.2.3 Increasing temporal variability of inertia levels

The total system inertia of a system, previously defined in (10), strongly depends on the generation mix dispatched for some operating point. In traditional power systems, since the inertia constants of different SGs are pretty similar, the total system inertia does not vary much with the generation dispatch [2]. However, the total system inertia becomes highly time-variant with the

increasing penetration of CIGTs since the variability of these resources provokes large fluctuations of SGs dispatch. Thus, the total inertia becomes a function of the expected wind and solar power output. For instance, in [6], the authors studied data from Germany's power system for 2012 and showed significant variations of total system inertia. Figure 3 shows the total inertia fluctuations for a month and the histogram of total inertia for the entire year. It varies from 6 s for an operating point with large amounts of SGs to 3 s for another operating point with high participation of CIGTs. This is a variation of 50 %, whose relevance should not be neglected.

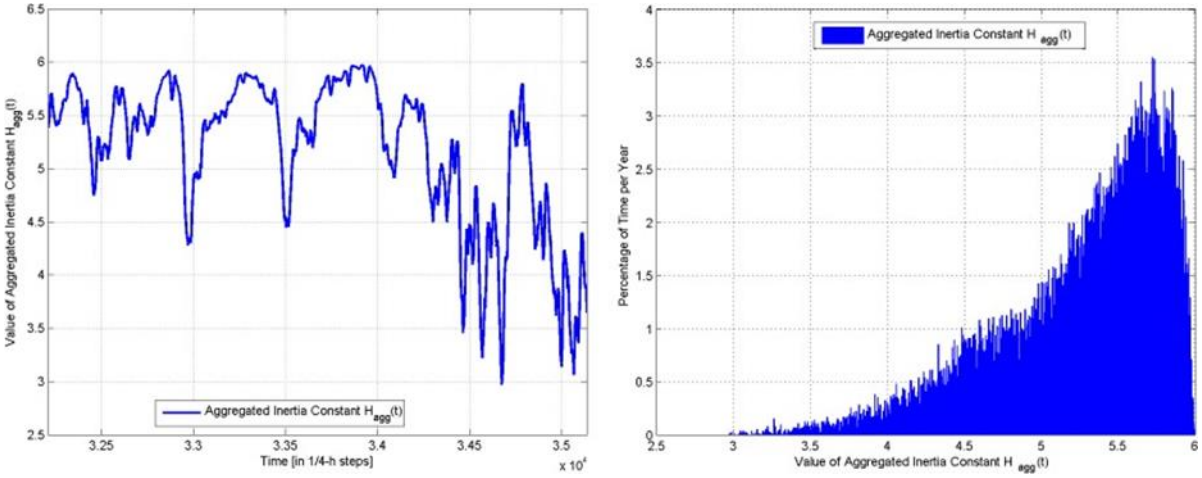

Figure 3: Time-Variant total system inertia in German Power System (December 2012), and Histogram of total system inertia in German Power System (full-year 2012) [6].

Another relevant study was presented in [14]. Authors have emphasized the increase of inertia's time variations with the increasing penetration of CIGTs in the Nordic Power System. Figure 4 shows an estimation of the inertia fluctuations for a two-month time frame in 2025. In this case, the inertia is expressed as the kinetic energy stored in the rotating machines present in the system in GWs. It can be noted that high variations arise from one day to another consecutive.

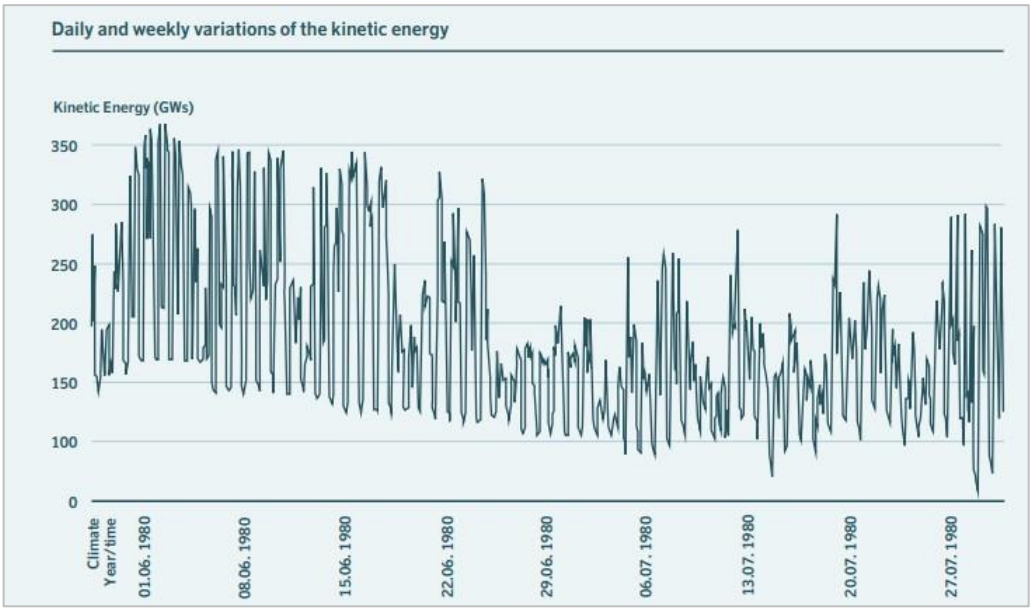

Figure 4: Estimated kinetic energy as a function of time in 2025 with a daily resolution for the Nordic Power System [14].

The time-variability of the total inertia constant is a relevant aspect that must be considered when planning future power systems. This should be done to ensure a sufficient amount of inertia at any operating point [3]. If CIGTs contribute to the inertial and primary frequency regulation, they can also affect the amount of total system inertia on a smaller time window. Since their reserves depend on their power output[1], CIGTs intra-hourly variability leads to a variable amount of total system inertia inside an hour. This poses a new challenge to ensure a certain level of inertia at some particular operating point.

2.2.4 Spatial distribution of inertia

Some researchers have shown that the spatial distribution of inertia strongly influences the frequency dynamics after a fault and not only the total system inertia [6] [18] [19]. For instance, in [18], the authors showed that local low-inertia areas present a higher RoCoF index than the rest of the system, suffer larger inter-area oscillations, and have shorter critical clearing times. Figure 5 shows the Great Britain reduced model with zonal inertia distribution used by authors in [18].

Two main zones identified as R1 and R2 concentrate 89.59 % and 10.41 % of the total system inertia, respectively. The RoCoF in the weakest zone (R2) is monitored for the same contingency (400 MW generation loss) at four different locations within R2; zones 24, 27E, 28, and 32, which concentrates 9 %, 3.49 %, 1.96 %, and 0.75 % of the total system inertia, respectively. The obtained RoCoF is tested under different operating points before the fault, and the results are organized in a box and whisker plot for each fault location. In addition, this is done in two cases: 1) base case of inertia distribution, according to Figure 5, and 2) case with R1 and R2 concentrating 94.8 % and 5.2 % of the total system inertia, respectively (more uneven inertia distribution). On the one hand, Figure 6 clearly shows a higher RoCoF in R2 when the contingency is located at zones with lower inertia concentrations. On the other hand, the figure also shows that no matter the location of the fault (x-axis of the plot), larger local RoCoF's are obtained in case 2, i.e., with more uneven distribution.

[1] Mechanisms to provide FFR from RESs are described in more detail in section 2.2.5

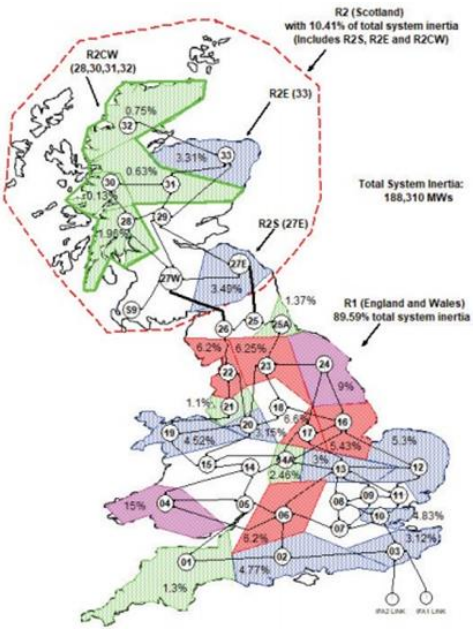

Figure 5: GB reduced model with zonal inertia distribution [18].

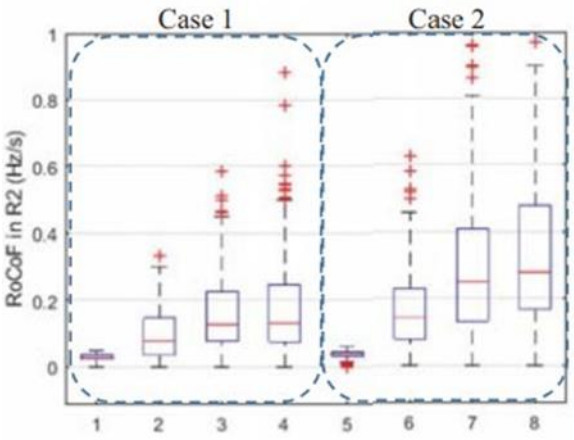

Figure 6: Effect of inertia distribution on local RoCoF [18] 1-4: Generation trip at 24, 27E, 28 and 32, respectively (case 1). 5-8: Generation trip at 24, 27E, 28 and 32, respectively (case 2).

When CIGTs replace the conventional power plants, it is expected to have a more uneven inertia distribution throughout the network [3]. Since large hydro power plants will likely always be based on synchronous machines, inertia will be distributed according to the locations of the hydro resources. In fact, this is the expected scenario for 2050 in the Chilean National Electrical Power System, a concentration of SGs based on hydro power plants in the South of the country and CIGTs distributed throughout the rest of the system. Although substituting all existing conventional power plants with CIGTs will undoubtedly require a few decades, it is possible that, for short periods, the percentage of synchronous generation can be very small or, even, null, especially when parts of the grid are islanded.

To accurately assess the robustness of future power systems, it will be necessary to consider the inertia as a heterogeneous variable instead of a global parameter [19]. Then, the inertia must be conceived as a spatial and temporal variant feature of a power system. In this regard, the traditional assessment of power system robustness through total system inertia is insufficient [4]. Then, a key challenge of TSOs is to propose novel indexes that quantify power system robustness in terms of

inertia distribution in future power systems. Up to date, only a few studies have progressed in this direction (an overview of state of the art about this topic is presented in Section 2.3).

2.2.5 Techniques to deliver FFR from CIGTs

Previous subsections described the main challenges which arise in power systems as CIGTs penetration increases due to their lack of inertial response. In order to minimize the possible negative impacts, different control techniques have been recently developed for enabling the capability to provide FFR from CIGTs. These solutions can be roughly classified into two main groups depending on an energy storage system's (ESS) presence (or not).

The first way to provide FFR to counteract the lack of inertial response of CIGTs power plants is through fast-acting ESS such as batteries, flywheels, or super-capacitors. Researchers have proposed several control strategies for allowing WTs and solar PVs to support system frequency during contingencies, including ESSs [8] [3] [9]. Depending on each solution, the power reserves delivered to provide FFR can come from the ESS or a combination between the ESS and some storage-less technique described below [21].

FFR can also be provided by implementing additional control loops specially designed for responding to frequency variations. Although power converters of CIGTs usually are not operated for doing that, incorporating these loops allows CIGTs to provide FFR to support the system during major power imbalances [10]. Indeed, some investigations have shown that the fast response times of power converters can provide essential benefits to system frequency compared to the frequency support provided by SGs [3].

Several control techniques have also been presented to allow CIGTs to provide FFR without ESS. No matter the alternative, this may require operating CIGTs in the so-called de-load mode [4] [8]. That is, instead of injecting all the available power, the CIGTs supply only a percentage of it, meaning that they operate at a sub-optimal point. In this way, there is some energy buffer available to contribute with inertial response and thus counteracting the effects of a power imbalance [4] [10]. The de-load margin is usually restricted to less than 20 % of the maximum nominal capacity of the CIGTs power plant [10]. For wind power plants, it is also possible to provide FFR without operating in de-load mode. This can be achieved using the kinetic energy stored in the blades to compensate power imbalances. However, special attention must be paid to the post-fault frequency recovery [4].

A classification of the techniques currently developed to deliver FFR from CIGTs is shown in Figure 7.

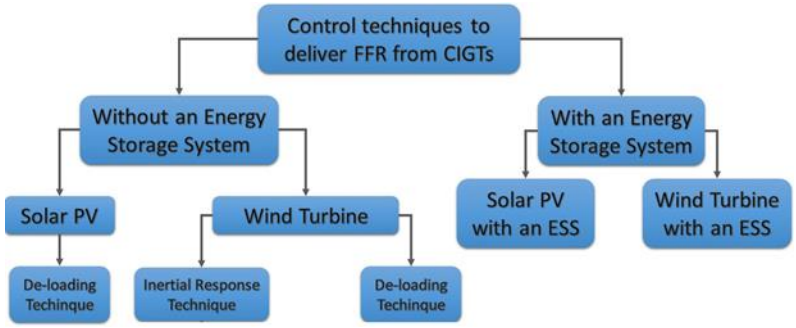

Figure 7: The techniques used to keep reserves in CIGTs to provide FFR.

2.2.6 New definition of total inertia including FFR from CIGTs

As described in the previous section, all the alternatives to provide FFR from CIGTs have in common: they need to store energy and deliver it fast, emulating SG's inertial response. This is often referred to as virtual (or synthetic) inertial response because of its controlled nature instead of the natural inertial response of SGs [4].

Virtual inertia is characterized by the virtual moment of inertia, following the same logic that the moment of inertia of SGs (see equation (1)). Then, similarly to the relationship between kinetic energy stored in the rotating masses of SGs and synchronous speed, an analogy between energy stored (in any form) ready to be delivered by CIGTs and the synchronous speed can be established by the following equation [4]:

$$E_v = \frac{1}{2} \cdot J_v \cdot \omega_e^2 \qquad (13)$$

where

- E_v = energy stored in a CIGT to provide FFR in J.
- J_v = virtual moment of inertia of a CIGT in $kg \cdot m^2$.
- ω_e = angular synchronous speed of the grid in rad/s.

If CIGTs can support the system frequency during contingencies, the FFR contribution of CIGTs should be considered and not only the contribution of SGs as in (10) [24]. Thus, a new definition of the total system inertia can be established as follows [4]:

$$H_{sys} = \frac{\sum_i^N E_i + \sum_j^M E_{vj}}{S_{sys}} \qquad (14)$$

where

- H_{sys} = total system inertia including SGs and CIGTs contribution to FFR, in s.
- E_i = kinetic energy stored in the rotating masses of generator i, in J.
- E_{vj} = energy stored in CIGT j to provide FFR, in J.
- S_{sys} = total generation capacity of the system, including SGs and CIGTs, in VA.

Finally, the total inertia in future power systems can be interpreted as the opposition to changes in frequency in the form of any stored energy from SGs and CIGTs, delivered immediately after power imbalances between generation and load [4].

2.3 Assessment of robustness in CIGTs-dominated power systems

The facts described in the previous sections show that the traditional approach to evaluatingpower system robustness by only considering the total inertia constant as defined

in (10) is not enough. Several investigations have shown that the total inertia constant would be insufficient in future low-inertia power systems [3] [4] as an indicator of how well the system can ride through major power imbalances. As already mentioned, even if FFR contribution from CIGTs is considered (as defined in (14)), the total system inertia may present significant time-space variations, meaning that just considering a single indicator for the whole system is not enough to quantify power system robustness. In fact, there can be significant differences in the frequency dynamic behavior between two or more areas of the system. Therefore, a novelapproach is needed to capture these differences and give indicators to quantify power system robustness faithfully.

Up to date, only a few research efforts have been made to define novel quantification approaches and indexes to accurately evaluate power system robustness in terms of frequency in case of high levels of CIGTs. In the following, a review of these research efforts is presented.

2.3.1 Assessment of temporal variability of inertia

2.3.1.1 Rate of Change of Inertia

In order to measure the temporal characteristics of the inertia, the authors in [25] proposed a novel index called Rate of Change of Inertia (RoCoI), which is defined as the derivative of the total inertia including CIGTs contribution (equation (14)) with respect to the current penetration of the CIGTs.

$$\mathrm{RoCoI} = \frac{\mathrm{dH_{sys}}}{\mathrm{dR_{pen}}} \qquad (15)$$

where

- H_{sys} = total system inertia including SGs and CIGTs contribution to FFR, in s.
- R_{pen} = penetration rate of CIGTs in pu, defined in (16).

$$\mathrm{R_{pen}} = \frac{S_{res}}{S_{sys}} \qquad (16)$$

where

- S_{res} = total generation capacity of the CIGTs connected to the system in VA.
- S_{sys} = total generation capacity of the system, including SGs and CIGTs, in VA.

As the authors suggested, the RoCoI index could be a quick indicator of inertial response shortage. Hence TSOs can prepare the unit schedule properly. For instance, if this index is below some limit, more SGs or other units capable of providing FFR can be scheduledto prevent a potential frequency instability [24].

An assessment procedure to evaluate the temporal distribution of the total system inertia through the RoCoI has been proposed in [24]. It is composed of two main steps: first, based on the predicted demand and CIGTs, the committed SGs are obtained and the value of the total system inertia for each hour is determined using (10). Then, the penetration rate

of CIGTs is obtained using (16). Consequently, the total system inertia variation trend is obtained by (15). The authors tested this procedure on the IEEE RTS-96 system to verify the effectiveness of their proposal for assessing the temporal variability of inertia. The load demand and available wind power profiles for 24 hours are shown in Figure 8:

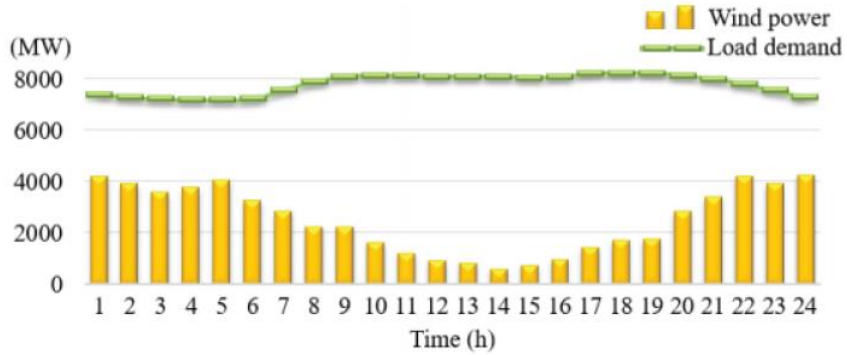

Figure 8: Load demand and wind power profile [25].

In that study, two cases have been considered; the "original case" where only SGs satisfy the load, and the "modified case" where wind power plants are also used to inject power into the load[2]. The total system inertia (expressed in MW *s*) time characteristicis shown in Figure 9:

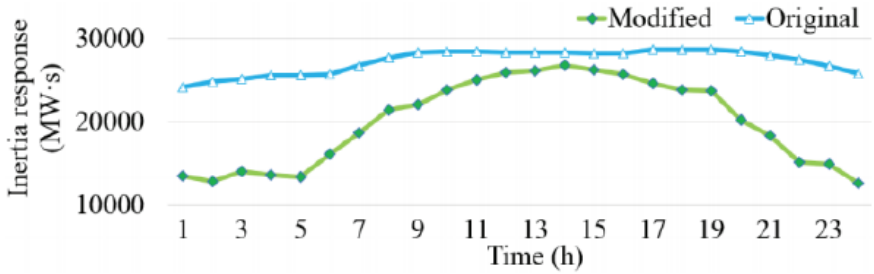

Figure 9: The temporal distribution of the total system inertia.

From Figure 9, it can be observed that the total system inertia is considerably less in the modified case compared with the original case. In fact, at hours with high wind power penetration, the inertia level even drops below 50% of the original level. For instance, in the 24-hour, its value descends to 12,654 MW *s* from 25,802 MW *s* in the original system. In addition, the temporal variability in the original case is quite limited, while the case with high wind shares shows huge variations for one day.

[2] It is assumed that wind power plants do not provide FFR, and then, they do not contribute to the total system inertia.

2.3.2 Assessment of the spatial distribution of inertia

In general, there are two types of approaches to analyze the spatial distribution of inertia: online and offline methods. The next sections present a review of the most relevant proposals of each type presented to date.

2.3.2.1 Online methods

Online methods are used to assess the spatial distribution of inertia in real-time through a constant feed of data from the WAMS network of the system. These methods aim to be a helpful tool to support the short-term security of the power system.

Up to date, there is only one proposal in this direction [25], where the authors derive a novel inertia distribution model and propose an online identification method based on active power and frequency measurements from the PMU's network of the power system. The derivation of the model is based on the psychical principle that there is an inverse relationship between the rate of change of the frequency in a node of the system and the inertia on that node, immediately after a sudden power imbalance occurs:

$$\dot{f}_j\big|_{t=0^+} = \frac{\alpha}{2h_j} \tag{17}$$

where

- $\dot{f}_j$ = time derivative of the frequency of the bus j.
- h_j = defined as the effect of the inertia on bus j.
- α = scaling factor that depends on the magnitude of the power imbalance.

The idea is to get first the frequency at each node f_j from the frequency divider proposed on [27] (described in section 2.4.1). Then, an expression for $\dot{f}_j\big|_{t=0^+}$ is derived analytically. Thus, given a certain α, h_j can be obtained through (17). Assuming small perturbations around nominal values (normal operation of the system), it can be obtained:

$$\frac{1}{h_j} = \sum_{i=1}^{n} \frac{m_{ij}}{H_i \cdot \alpha} \cdot (\Delta P_i | t = 0) \tag{18}$$

where

- H_i = Inertia constant of the generator i in pu.
- ΔP_i = Active power imbalance at generator i in pu.

Since ΔP_i is proportional to α, h_j is mainly determined by m_{ij} and H_i. From this model,an identification method composed of two stages is proposed:

- **Stage 1:** MISO (multiple input single output) dynamic model derivation between the changes in active power injected at all the generation busbars and the frequency

deviation of bus j under normal operating conditions. The model has different parameters for each operating point, for example, the value of m_{ij}. In this stage, measurements from the WAMS network are used.

- **Stage 2:** Apply a unit step in the identified model and estimate h_j according to (18).

The authors compared the performance of their WAMS -based estimation method with a pure theoretical derivation,which led to that the effect of the inertia over each node h_j satisfies the following equation:

$$\frac{1}{2h_j} = \sum_{i=1}^{n} \frac{m_{ij}}{2H_i} \quad (19)$$

Through this method, the authors can perform an online estimation of the spatial distribution of inertia in just a few seconds. As a reference, they tested their methodology on the IEEE-39 bus system, where it works satisfactorily with a computation time of less than 1 second.

2.3.2.2 Offline methods

Offline methods are used to assess the spatial distribution of inertia through simulations based on dynamic models that approximately represent the real power system behavior. They are focused on being a helpful support tool for planning problems in the mid or long term. For instance, in the mid-term, weak low inertia areas of the system can be identified, and constraints to the unit commitment (UC) of the CIGT can be established accordingly. In the long term, it is possible to define centers of CIGT development in robust areas or encourage the ancillary services in weak areas, among other applications.

Inertia Distribution Index

To quantify the spatial distribution of the inertia, an Inertia Distribution Index (IDI), which allows estimating the distance from any bus to the Center of Inertia (COI) location, is proposed in [28]. COI is a concept used in power systems to reduce a set of signals into a single variable that approximately represents their dynamic behavior. In the case of the frequency, although it is practically the same for the whole system during normal operation, it could significantly differ between two busbars during the transient period after a contingency. A COI-referred signal could be used to reflect the whole system behavior through a single variable, the center of the frequency f_{COI}, which is defined as follows:

$$f_{COI}(t) = \frac{\sum_i^N H_i \cdot f_i(t)}{\sum_i^N H_i} \quad (20)$$

where

- N = number of generators connected to the system
- H_i = per unit inertia constant of the generator i in s.
- $f_i(t)$ = frequency measured at the terminals of the generator i at time t in Hz.

Note that calculating the f_{COI} in a real power system through the definition in (20) could be difficult. In fact, measuring the frequency of all the generators connected to the grid and collecting that information to a centralized control center cannot be done easily in practice. For this reason, the definition in (20) needs some flexibility in order to be able to obtain the f_{COI} with the TSO's available measurements. Although authors in [28] did not propose a solution for this, a possible approach to estimate the f_{COI} could be to use the frequency measurements obtained from Phasor Measurement Units (PMUs). This would need a definition of limited zones of the system according to the PMUs locations, and then group the inertia constants Hi of the generators of each area into one equivalent inertia constant of the zone. However, authors in [28] assumed that frequency measurements at all system generators are available.

Before defining the IDI proposed in [28], it is necessary to define a way to quantify the distance between any busbar of the system to the COI location over a period T:

$$d_k = \int_{t_0}^{T+t_0} [f_k(\tau) - f_{COI}(\tau)]^2 d\tau \qquad (21)$$

where

- d_k = distance between the bus k and the COI location in Hz.
- $f_k(\tau)$ = frequency measured at the bus k at time τ in Hz.
- $f_{COI}(\tau)$ = frequency of the COI at time τ in Hz.

The distance d_k defined in (21) depends on the measurements taken over a period T. Thus, a busbar k could be close (low value of d_k) or far away (high value of d_k) from the COI location depending on the period T considered, which is chosen according to some contingency. The authors mention that a set of contingencies with their corresponding measurements must be evaluated to properly assess how far each busbar is from the COI [25].

Finally, by normalizing d_k with respect to the highest distance, the IDI is defined using (22):

$$\mathrm{IDI}_k = \frac{\mathrm{d_k}}{\max\limits_{k \in M} d_k} \qquad (22)$$

where

- IDI_k = Inertia Distribution Index of bus k in pu.
- M = set of the buses of the system.
- $\mathrm{d_k}$ = distance between the bus k and the COI location in Hz.

High values of IDI for a bus k indicates that:

1. The electrical distance from bus k to the COI is relatively large. Notice that the COI is not exactly located on a particular bus. An approximation of its physical location can be the bus with the closest (lower) value of IDI_k.

2. The bus k is located in an area with a low concentration of inertia.

Note that obtaining $\mathrm{d_k}$ from (21) needs continuous frequency sampling to compute the integral involved. In [25], the authors suggested that this may be impossible in practice due to the data's digital nature. Consequently, they proposed an improved $\mathrm{d_k}$ as follows:

$$d_k = \sum_{i}^{m} T_{sam} \cdot [f_k(i) - f_{COI}(i)]^2 \qquad (23)$$

where

- T_{sam} = sampling period in s.
- $f_k(i)$ = frequency measured at the bus k at time i in Hz.
- $f_{COI}(i)$ = frequency of the COI at time i in Hz.

By normalizing d_k by the range of the electrical distance, the IDI can be redefined as:

$$\mathrm{IDI}_k = \frac{d_k - d_{k\,max}}{d_{k\,max} - d_{k\,min}} \qquad (24)$$

where

- d_k = distance between bus k and the COI location in Hz.
- $d_{k\,max}$ = distance between the COI location and the farthest bus in Hz.
- $d_{k\,min}$ = distance between the COI location and the closest bus in Hz.

Although this index seems to be a simple way to characterize the spatial distribution of inertia, its calculation needs to pre-define a set of contingencies, which selection is a complex task that must be done carefully. Accordingly, authors in [25] proposed a framework to assess the inertia distribution through IDI that includes selecting a contingency set. However, it is unclear how to choose that set and how dependent the results are on the events chosen.

The performance of IDI_k was tested in the modified IEEE RTS-96 system, including wind power plants at different locations in the grid. This power system is divided into three main areas, as shown in Figure 10.

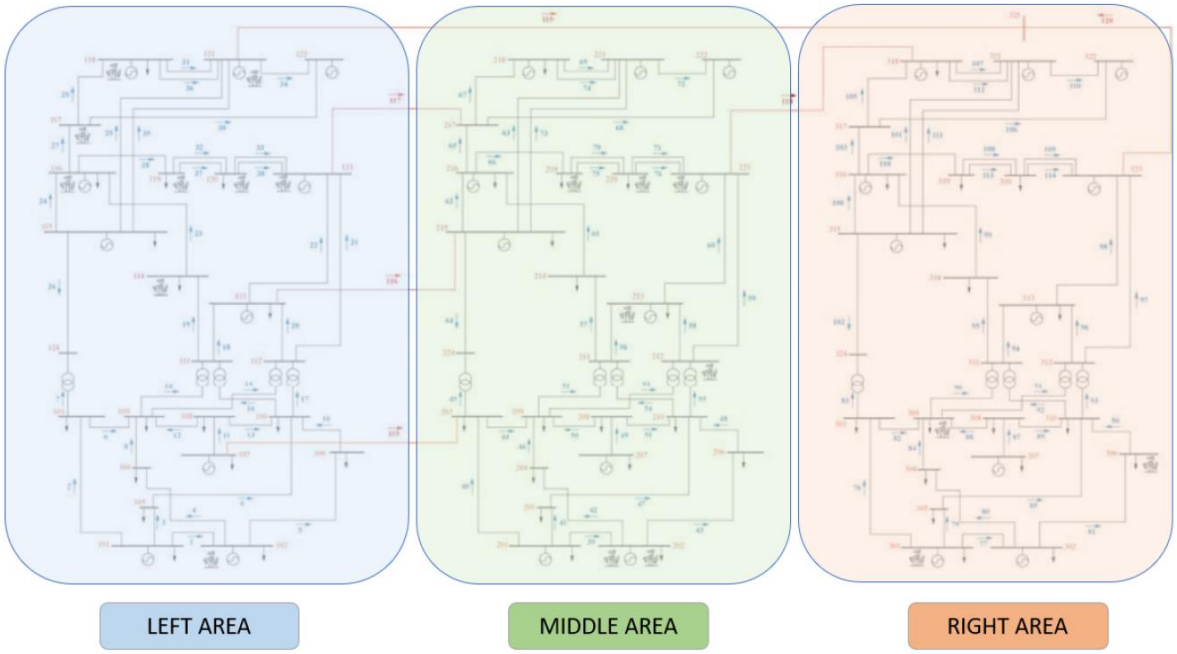

Figure 10: IEEE RTS-96 system areas division [25].

Different wind power penetration levels per area were considered in three cases, as shown in Table 2.2. The highest penetration on each case is 3,900 MW (56.5 %), and it is located at the LEFT, MIDDLE, and RIGHT areas, respectively.

Wind Power (MW)	Case 1	Case 2	Case 3
LEFT Area	3,900	600	600
MIDDLE Area	1,500	3,900	1,500
RIGHT Area	600	1,500	3,900

Table 2: Wind power in the modified RST-96 system with different cases [25].

A set of contingencies were executed, and the f_{COI} is calculated for each area using (20). Then, based on dynamic simulations, frequency data of all system busbars are obtained, and hence d_k is calculated using (23). Finally, IDI_k is obtained for each busbar k using (24). The results are plotted into a heat map, as shown in Figure 11. The authors found that the areas with low inertia match those with high integration of wind power. Thus, the system inertia is mainly concentrated in the regions dominated by synchronous units, which verifies the proposed IDI's effectiveness for revealing the inertia's spatial distribution [25].

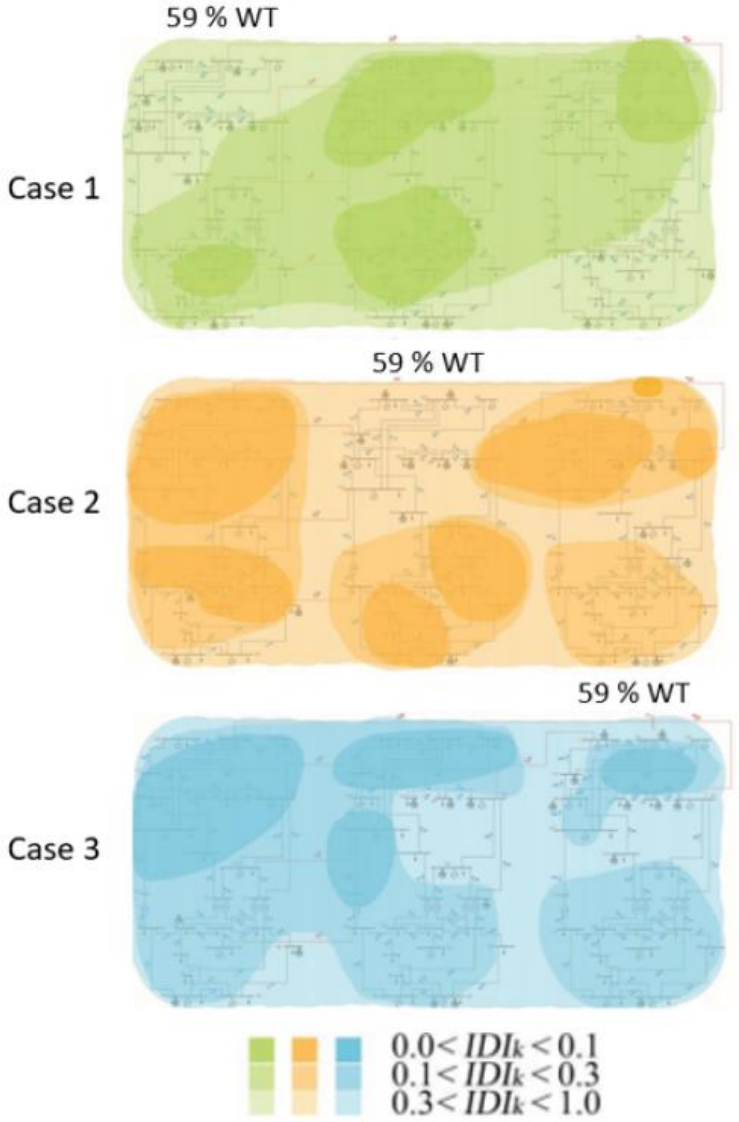

Figure 11: Inertia distribution in the three cases [25].

Center of Oscillation Index

In [29], the Center of Oscillation Index (S1) is proposed. Before defining this index, the following equation must be introduced:

$$SD_1(k) = \sum_{i}^{N} \sum_{j}^{N} \int_{t_0}^{t_0+T} \left[\omega_i(t) - \omega_j(t)\right] dt,\ i \neq j \qquad (25)$$

where

- N = number of generators connected to the system.
- $\omega_i(t)$ = rotor speed of the generator i at time t in rad/s.
- $\omega_j(t)$ = rotor speed of the generator j at time t in rad/s.

- t_0 = initial time when the contingency occurs in s.

By normalizing $SD_1(k)$ by the maximum value of $SD_1(k)$, the center of oscillation index is defined as:

$$S_1(k) = \frac{SD_1(k)}{\max\limits_{k \in M} SD_1(k)} \quad (26)$$

To calculate SD_1 for a particular busbar k, a contingency located at the same location k needs to be simulated, and then, the differences between the frequency measurements (or rotor speeds) of all the generators are integrated over a period T as given in (25). The main difference of SD_1 with respect to the IDI is that its calculation needs to simulate a contingency for each busbar k. On the contrary, IDI only needs a user-defined set, which could be only one contingency, and then it evaluates "how far" is a particular busbar k from the COI.

Since this index compares the results when the perturbation is performed at all potential locations, the authors suggested that it is more accurate than the IDI_k. Although, it is more time-consuming since it needs further calculations. Hence, authors in [29] suggested that $S_1(k)$ can be used in applications when accuracy is more critical than the computation time. Otherwise, IDI_k can be used.

The performance of $S_1(k)$ was tested in a meshed system composed of four SGs (400 MW of total generation) and four loads, as shown in Figure 12. Three cases were considered with different inertia constants for each generator, according to Table 3. $S_1(k)$ is calculated by executing a 50 MW load step at each bus k for the three cases. The results are shown in Figure 13, Figure 14, and Figure 15 for cases 1, 2, and 3, respectively.

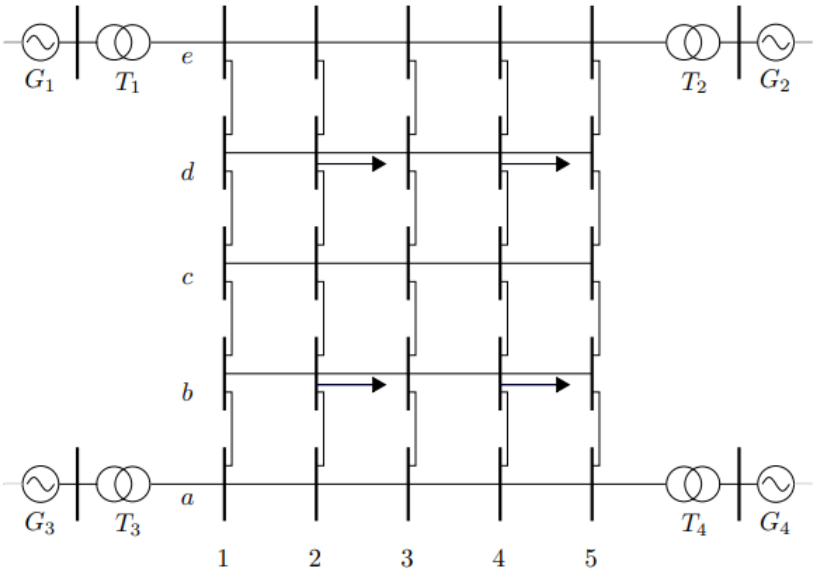

Figure 12: Meshed system topology [29].

Inertia constant (s)	Case 1	Case 2	Case 3
H_1	4.25	4.25	6.00
H_2	4.25	4.25	4.25
H_3	4.25	8.50	6.00
H_4	4.25	4.25	4.25

Table 3: Inertia constants of each generator for the three cases [29].

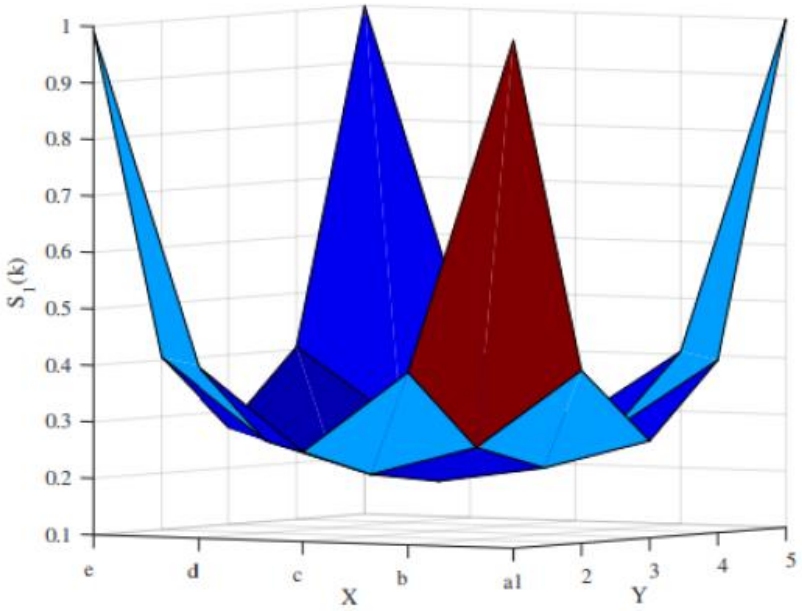

Figure 13: S_1 in meshed system, case 1 [29].

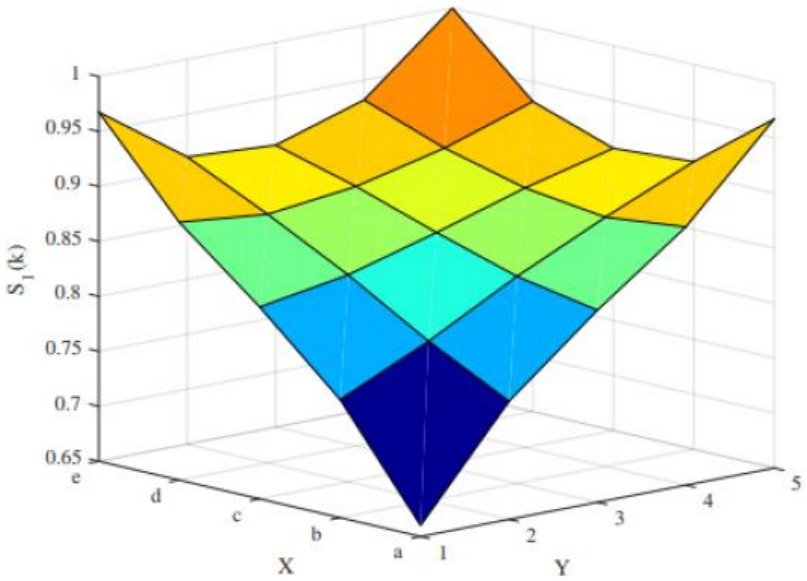

Figure 14: S_1 in meshed system, case 2 [29].

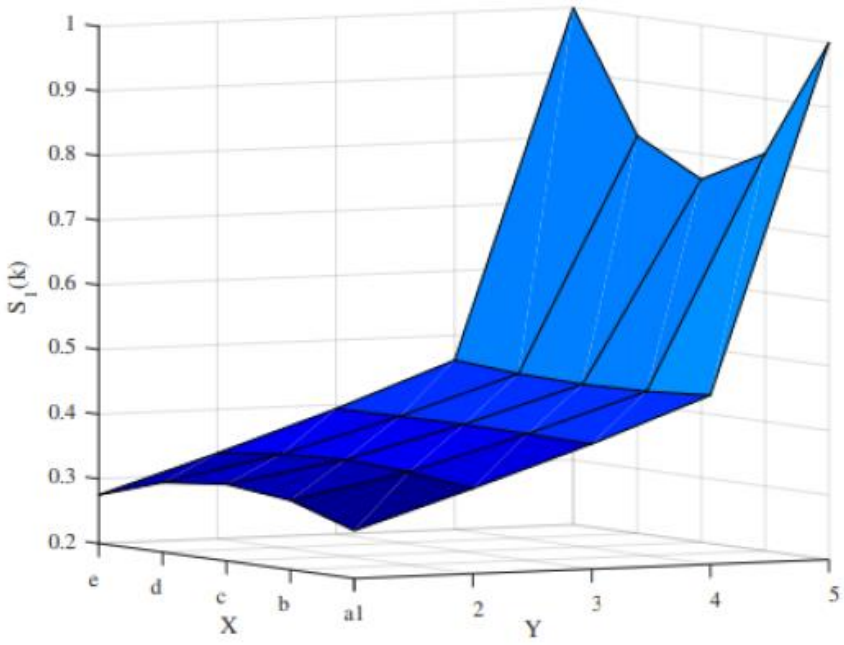

Figure 15: S_1 in meshed system, case 3 [29].

Figure 13 shows the result in the base case where all SGs have the same inertia constant. The lower value of $S_1(k)$ (strongest busbar) is located at the geometric center of the grid. Figure 14 shows the result where H_3 is twice the inertia constant of the other generators. In this case, the lower $S_1(k)$ is located at the G3 busbar, where most inertia is concentrated. Finally, Figure 15 shows the result in case 3, where the lower values of $S_1(k)$ are obtained close to the generators with larger inertia constants.

Authors in [29] concluded that the Center of Oscillation Index successfully reflects the system characteristics like the machine's inertia. However, this index was only validated using a small test power system. Therefore, further research is needed to validate the effectiveness of $S_1(k)$ to quantify the spatial distribution of inertia on a real power system. In addition, it is not clear how to define the contingencies required for its calculation and if the time cost involved in its calculation is suitable for real applications.

Dissimilarity coefficient

Another approach to assess the spatial distribution of the inertia is to group a subset of generators into clusters to define system areas. Then, an assessment of the equivalent inertia of each group can be done to identify the potential weak zones. For this purpose, Dissimilarity Coefficient has been proposed in [30]. This coefficient reflects the Euclidean distance between a pair of generators according to the following equation:

$$dist(i,j) = \sqrt{\sum_{t}^{T} \left[\omega_i(t) - \omega_j(t)\right]^2} \quad (27)$$

where

- $\omega_i(t)$ = speed deviation of the generator i at time t in rad/s.
- $\omega_j(t)$ = speed deviation of the generator j at time t in rad/s.

This coefficient represents a way to quantify "how far" is a generator from another one, and it depends on the period T considered for its computation (similar to the calculation of IDI and S_1). The period T has to be taken after some disturbance to observe differences between two arbitrary generators. To characterize the distance between two generators, a contingency set must be considered and simulated.

Based on $dist(i,j)$, the authors in [30] proposed to group generators into clusters using some technique to delimit the system's areas. They mentioned that one of the best algorithms used is the average linkage method due to its excellent performance. This is done according to the following equation:

$$d_{rs} = \frac{1}{N_r \cdot N_s} \sum_{i=1}^{N_r} \sum_{j=1}^{N_s} dist(x_{ri}, x_{sj}) \qquad (28)$$

where

- N_r and N_s = number of generators in the cluster (r) and (s), respectively.
- $dist(x_{ri}, x_{sj})$ = distance between the generator x_i in the cluster (r) to the generator x_j in the cluster (s).

This index was tested on a 16-generator test system shown in Figure 16. Then, the authors considered a set of contingencies of all possible line outages, which are cleared after 90 ms. The methodology follows computing $dist(i,j)$ using (27) and then merging the pair of generators with the smallest coefficients into one cluster. $dist(i,j)$ is then updated using (28) and the process is repeated until the final cluster is obtained. The results are shown through the cluster tree in Figure 17 a) and the dissimilarity coefficient of the merged units at each clustering step in Figure 17 b).

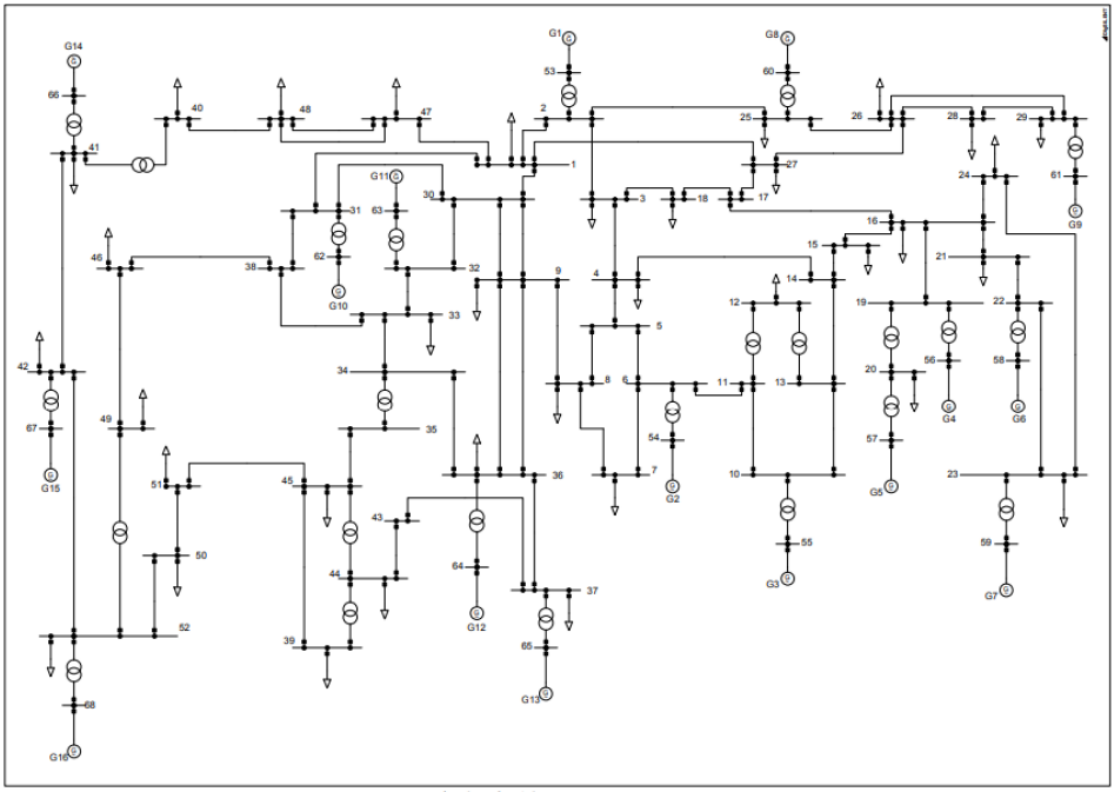

Figure 16: The 16-generator test system [30].

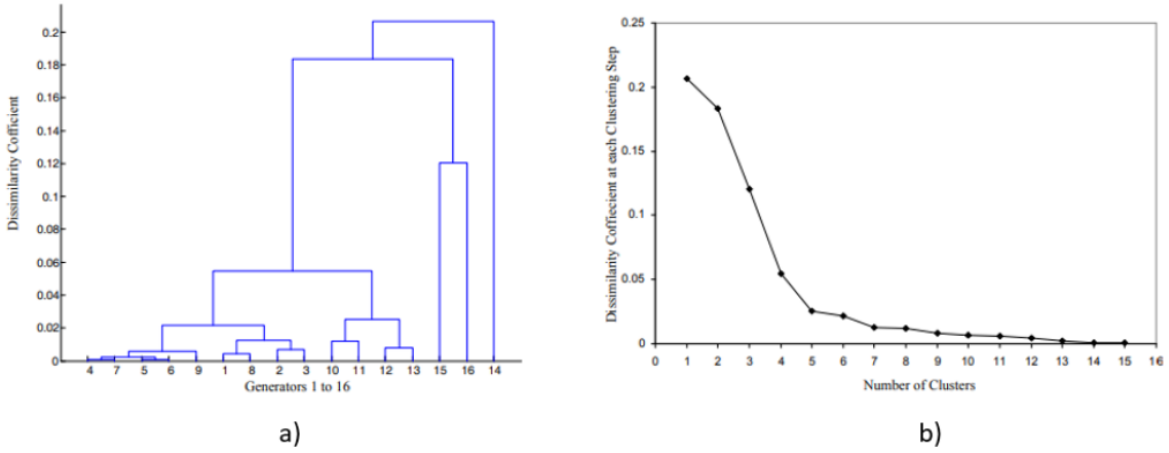

Figure 17: a) The cluster tree. b) The dissimilarity coefficient at each clustering step [30].

2.4 Mathematical background

This section presents a brief description of some analysis tools used in Chapter 3 Methodology. It is divided into two categories: power system analysis tools, where specific procedures and novel formulas presented by leading researchers in power systems are described, and data analysis tools, where general scientific methods regarding data analysis are presented.

2.4.1 Frequency divider

Traditionally, frequency stability has been evaluated, assuming that frequency is a global variable for the entire system. However, as described in section 2.2.4, in future weak power systems, this approach may not be sufficient to properly assess the differences of the frequency dynamic response throughout the grid and thus prevent instabilities that could arise. In order to take care of this matter, some efforts have been made in recent years, where one of the tools investigated that has had the greatest impact is the **frequency divider** [27]. In [27], the authors presented a simple and reliable formula to estimate the frequency at every busbar of the system based on the frequency of the SGs. While the frequency of the COI has been very useful on transient and frequency stability analysis, it cannot capture local oscillations, which is the main contribution of the equation proposed, thus improving the accuracy of the dynamic models used in such analysis. Authors have demonstrated that the frequency divider performs better than other solutions like washout filters.

The starting point of the analytical derivation of the frequency divider is the augmented admittance matrix of the system, which includes the internal impedance of the SGs. The system currents and voltages are related according to the following expression:

$$\begin{bmatrix} \widehat{\imath_G} \\ \widehat{\imath_B} \end{bmatrix} = \begin{bmatrix} \widehat{Y_{GG}} & \widehat{Y_{GB}} \\ \widehat{Y_{BG}} & \widehat{Y_{BB}} + \widehat{Y_{B0}} \end{bmatrix} \cdot \begin{bmatrix} \widehat{e_G} \\ \widehat{v_B} \end{bmatrix} \quad (29)$$

where considering a n-busbar and n_g-generators system:

- $\widehat{v_B}$ and $\widehat{\imath_B}$ = voltages and current injections on each busbar of the grid, respectively $(n \times 1)$.
- $\widehat{v_G}$ and $\widehat{\imath_G}$ = e.m.f behind the internal impedance and current injections of each SG, respectively $(n_g \times 1)$.
- $\widehat{Y_{BB}}$ = standard admittance matrix of the system $(n \times n)$.
- $\widehat{Y_{GG}}$, $\widehat{Y_{GB}}$ and $\widehat{Y_{BG}}$ = admittance matrices obtained using the internal impedances of the SGs.
- $\widehat{Y_{B0}}$ = diagonal matrix that contains the internal impedances of the SGs in the generation busbars.

Analytical derivation follows from (29) and considers the following assumptions:

1. Admittance matrix dependence on the frequency is neglected. This assumption has minimal impact on the estimation accuracy, allows for a compact expression, and is easy to calculate.

2. Current injections from loads $\widehat{\imath_B}$ are neglected. This assumption is justified by the fact that the equivalent admittance of loads is usually a magnitude order inferior to thediagonal elements of $\widehat{Y_{BB}} + \widehat{Y_{B0}}$.

3. Quasi-steady phasor during the electromechanical transient is approximated to the magnitude of the *dq* reference axis: $\widehat{v_h} \approx \widehat{v_{dq,h}}$.

4. The parameters of the transmission lines, transformers, loads, and generators are assumed constant.

5. All the busbar voltages and e.m.f of SGs are assumed equal to 1 pu.

6. Conductance of diagonal elements of the admittance matrix is neglected $\widehat{Y_{BB}} \approx jB_{BB}$.

7. It is assumed that $\omega_0 = 1$.

All the assumptions mentioned above are based and motivated on common simplificationsin the context of electromechanical phenomena and typical parameters of a high voltage transmission system. Finally, the frequency divider formula is presented in the following:

$$\omega_B = 1 + D(\omega_G - 1) \tag{30}$$

where

$$\mathrm{D} = -(B_{BB} + B_{B0})^{-1} \cdot B_{BG} \tag{31}$$

The equation (30) allows **estimating the frequency at every busbar ω_B from the rotor speed of SGs ω_G**, which act as boundary conditions of the steady-state problem.

2.4.2 Agglomerative hierarchical methods of cluster analysis

The objective of hierarchical methods is to merge clusters into a new one or split one cluster into two others, and then, by repeating one of these processes successively, minimize the difference or maximize the similarity between the objects. Hierarchical methods are classifiedinto agglomerative or dissociative techniques [31].

- Agglomerative hierarchical methods begin by considering as many groups as objects to be analyzed. On one step of the algorithm, the closer groups, i.e., have the minimum distance or the maximum similarity, are merged to form a new group. This process is repeated until some stopping criteria are met.

- Dissociative hierarchical methods realize the opposite process to agglomerative methods. They begin by considering only one group that contains all the objects to be analyzed. On each step of the algorithm, the groups that are further away, i.e., have the maximum distance or the minimum similarity, are divided to form a new group. This process is repeated until some stopping criteria are met.

Several techniques differ on the criterion to calculate the distance metric between two clusters during the process. The most common and basic used methods arelisted below [31]:

- Single linkage method
- Complete linkage method
- Non-weighted average linkage method
- Weighted average linkage method
- Centroid-based methods.

This work uses an agglomerative technique based on the weighted average linkage method, which is briefly described in the following.

The Weighted average linkage method considers that the distance (or similarity) between two clusters is defined as the weighted average of the distances (or similarities) between the components of one cluster to the other.

Thus, after completing the k-th iteration, there are $n - k$ clusters and the distance between the clusters C_i (with n_i elements) and C_j (with n_j elements) is:

$$d(C_i, C_j) = \frac{1}{n_i \cdot n_j} \sum_{x_i \in C_i} \sum_{x_j \in C_j} d(x_i, x_j) \qquad (32)$$

Then, in the k+1-th iteration, the clusters to be merged are those that $d(C_i, C_j)$ is the minimum.

3 Methodology

In this chapter, a detailed description of the methodology implemented to achieve the goals of the research is presented. The main result is an offline tool capable of automatically identifying weak frequency areas for each system operating condition. Figure 18 shows how it works at the macro-level:

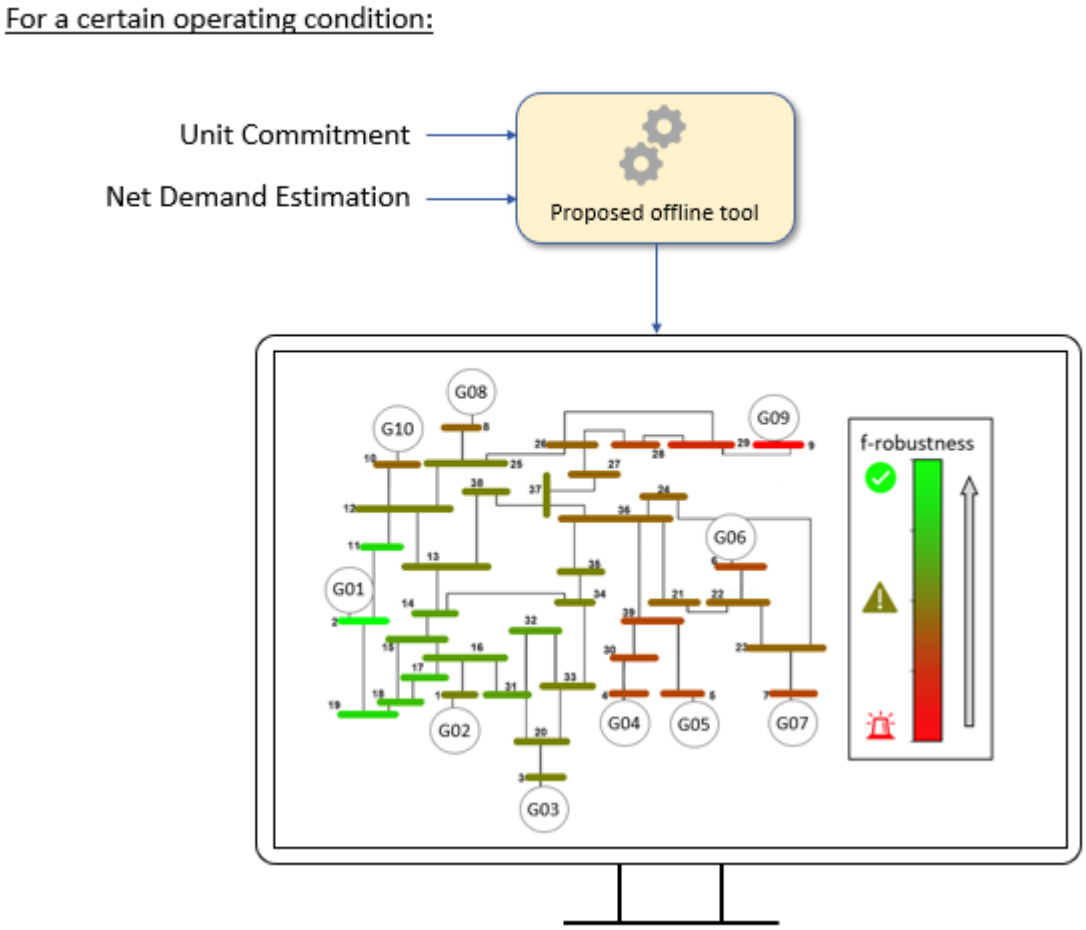

Figure 18: Macro-level diagram of the proposed solution.

For ensuring the practical use of the proposed tool, the following requirements must be fulfilled:

1. To be computationally inexpensive to be run in a reasonable time for the expected applications.

2. To present the results in a user-friendly display system, quickly identifying weak areas and thereby making it easier for the TSO to take actions over several resources distributed throughout the grid.

3. To quantify the level of robustness in terms of frequency through comprehensive indexes.

A six-stage methodology is proposed to develop the solution: In the first stage, a market simulation for a complete year is done using classical economic dispatch analysis tools. In the

second stage, an identification of a subset of representative operating conditions that represent worst-case scenarios from a frequency stability perspective is made. In the third stage, a set of time-domain dynamic simulations (ΔP contingencies) are performed for all the representative operating conditions. In the fourth stage, the results of the third stage are used to identify coherent groups of SGs. In the fifth stage, the results of the previous stage are extended to derive coherent frequency areas. Finally, in the last stage, the system robustness in terms of frequency (f-robustness) is determined through novel comprehensive indexes that consider the spatial distribution of inertia. This procedure is summarized in Figure 19, where main inputs and outputs are highlighted for each stage.

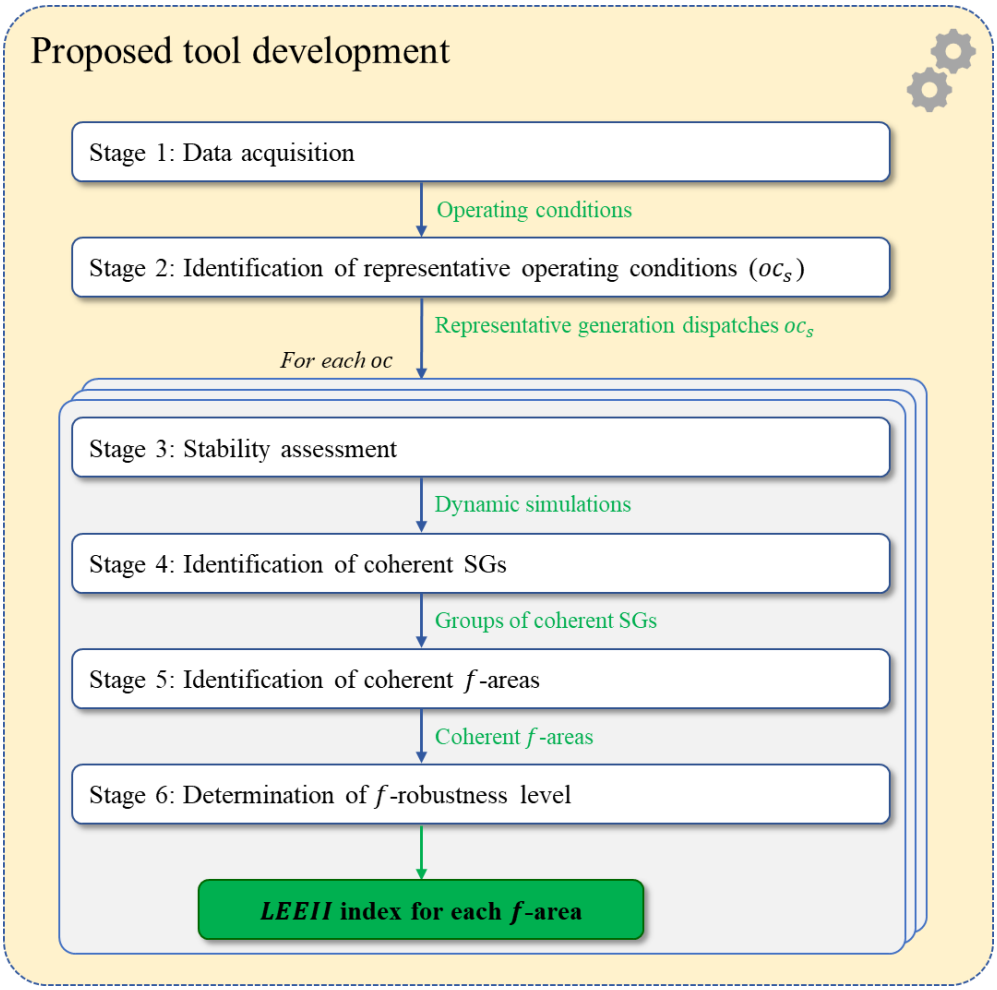

Figure 19: Methodological framework.

In the following, general guidelines to implement stages 1 and 2 are provided since their results can be obtained in several ways using well-known traditional economic tools. Then, a detailed description of stages 3 to 6 is presented since they are the main contribution of this thesis.

By following the stages mentioned above, the proposed offline tool is developed. Then, its performance to identify weak conditions that may threaten the frequency stability of the system is validated in section 5.2.

3.1 Stage 1: Data acquisition

The goal of this stage is to define the initial set of operating conditions that represent all the possible states that the system may experience for a year of operation. For instance, a set of 8760 operating conditions for a 1-hour dispatch resolution period system. This initial set can be obtained from traditional market simulation tools such as a Unit Commitment (UC) [33] or an Optimal Power Flow (OPF) [34].

3.2 Stage 2: Identification of representative operating conditions (oc_s)

Weak areas of a power system strongly depend on the system operating state. In principle, this would render weak system areas to change according to generators dispatch, which in the best case would imply that they change every hour. Although the generators dispatch between two hours of a year can differ significantly, it can also be very similar for many others. In addition, considering that the proposed tool aims to support the operator in planning tasks, to have a set of representative generation "dispatches modes" would be much more adequate than a set of 8760 specific system states. Accordingly, the second stage of the methodology aims to define a set of representative generation dispatches that the system can experience over a year. The set selected must be small enough to guarantee the applicability of the proposed tool, but it should also cover all possible critical system conditions.

Recent research has proposed detailed methodologies to define the required subset of critical generation dispatches for frequency stability studies [35][36]. For instance, authors in [36] proposed to face this task by first implementing a filter specially designed to preselect a subset of worst-case scenarios. The filter selection is based on the computation of key features from a frequency stability perspective: the inertial response and primary frequency control. Then, a classical clustering technique to group similar filtered critical operating conditions is done. Finally, they obtain the set of representative operating conditions by getting the centroids of each cluster [36].

The following stages, Stages 3 to 6, are done for each representative operating condition. In the following, the process for a single generic oc_i in these stages is described in detail.

3.3 Stage 3: Stability assessment

The goal of this stage is to execute a set of dynamic positive sequence simulations allowing to characterize the system's dynamic behavior following sudden power imbalances from a frequency stability perspective. For this purpose, the set of N representative operating conditions selected from the previous stage is considered $\mathrm{o}c_i \in \{\mathrm{o}c_1, \mathrm{o}c_2, \dots, \mathrm{o}c_N\}$.

For each operating condition $\mathrm{o}c_i \in \{\mathrm{o}c_1, \mathrm{o}c_2, \dots, \mathrm{o}c_N\}$, a set of M_i critical contingencies (power imbalance ΔP) $c_j \in \{c_1, c_2, \dots, c_{M_i}\}^{oc_i}$ is defined. Accordingly, a set of $N \cdot M_i$ time-domain simulations are executed considering a detailed dynamic model of the BPS. For each dynamic simulation, the frequency $\Delta f_{k\,c_j^{oc_i}}$ (or speed) deviation from its nominal value of each online SG k is recorded.

The results obtained in this stage are the input of the next stage, where coherent synchronous generators are identified.

Figure 20 shows a detailed flowchart of this stage.

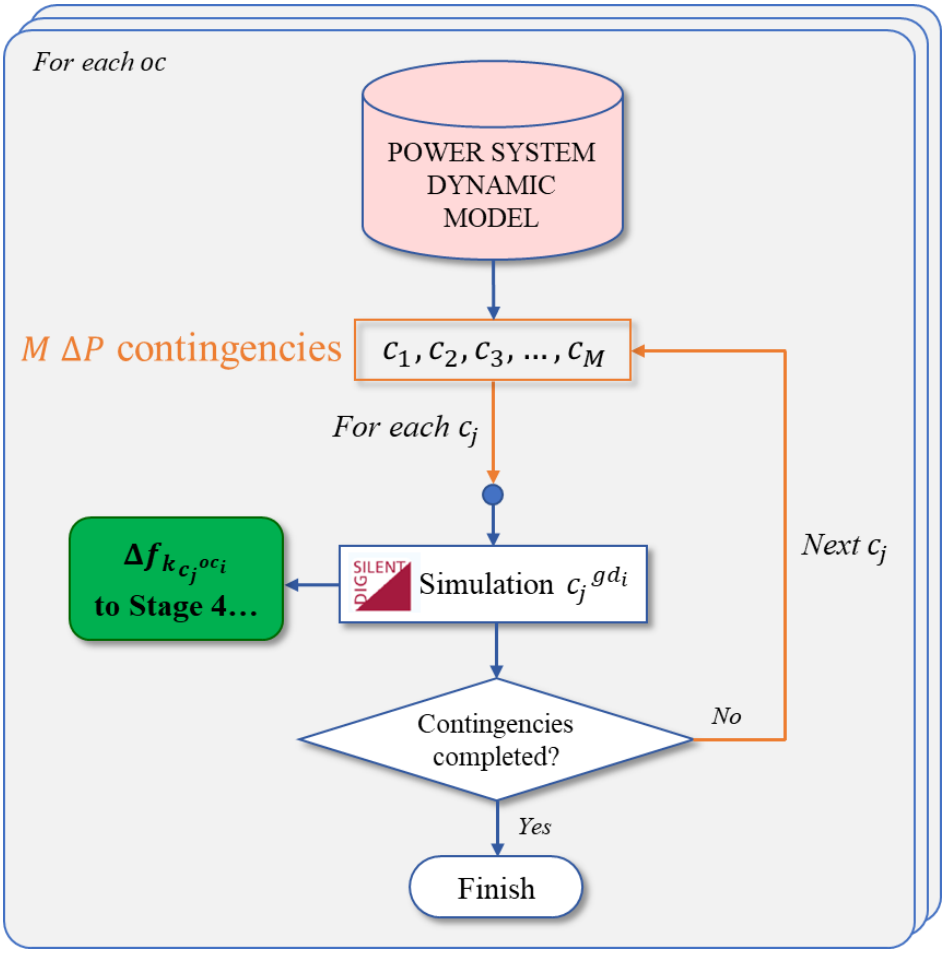

Figure 20: Methodological flowchart | Stage 3.

3.4 Stage 4: Identification of coherent SGs

The goal of this stage is to identify coherent groups of synchronous generators considering all operating conditions and critical contingencies under study. In general, the concept of coherency indicates a close relationship between the dynamic response of two objects. In this case, coherent generators are those that show a very similar dynamic response of their frequency (or speed) after a set of contingencies for a specified period T.

Figure 21 shows an example of the result from applying this stage to the well-known IEEE 39-bus test system for a single operating point, where coherent generators are colored together. Note that the results are consistent with the electrical distance between the generators.

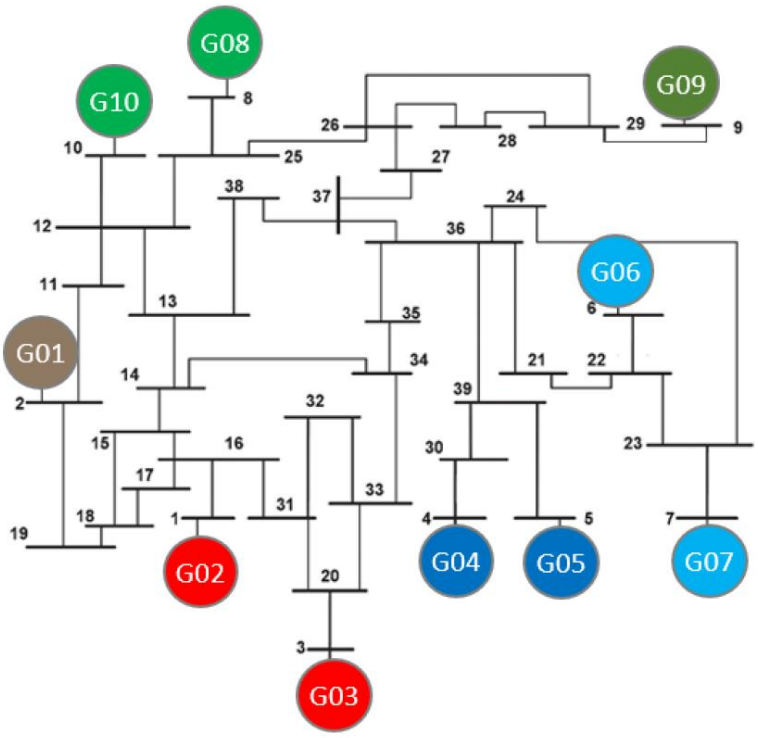

Figure 21: Example of the result of Stage 4 | Resultant layout in the IEEE 39-bus system.

To identify coherent SGs after contingency oc_i, the dissimilarity coefficient between two generators k_1 and k_2, is used as shown in equation (33) [30]:

$$dist(k_1, k_2)|c_j^{oc_i} = \sqrt{\sum_{t}^{T} [\omega_{k_1}(t) - \omega_{k_2}(t)]^2} \quad (33)$$

where

- $\omega_{k_1}(t)$ = speed deviation of the generator k_1 at time t in rad/s.
- $\omega_{k_2}(t)$ = speed deviation of the generator k_2 at time t in rad/s.
- T = period after the contingency c_j occurs on the representative operating condition oc_i. In this case, a period of 30 seconds after the event is considered.
- $c_j^{oc_i}$ = contingency c_j in the representative operating condition oc_i.

The formula defined above is valid for a single simulation (considering contingency c_j in the operating condition oc_i). To quantify the distance between two SGs considering all contingencies $c_j \in \{c_1, c_2, \dots, c_{M_i}\}^{oc_i}$ for the operating condition oc_i, the sum of the distances of each event is considered as shown in equation (34):

$$d(k_1, k_2)|\mathrm{o}c_i. = \sum_{j=1}^{M} dist(k_1, k_2)|c_j^{oc_i} \quad (34)$$

Then, with $d(k_1, k_2)|\mathrm{o}c_i$ as the metric of the distance between individual generators, an agglomerative clustering technique, the average linkage method, is implemented. This method defines how to calculate the distance between two clusters (q) and (r) composed by individual generators during the clustering process, and it is shown in equation (35):

$$dc(q, r)|\mathrm{o}c_i = \frac{1}{N_q N_r} \sum_{i_1}^{N_q} \sum_{j=1}^{N_r} d(k_q, k_r)|\mathrm{o}c_i \quad (35)$$

where

- $dc(q, r)|\mathrm{o}c_i$ = distance between cluster (q) and (r) for the representative operating condition $\mathrm{o}c_i$.
- N_q and N_r = number of generators in the cluster (q) and (r), respectively.
- $d(k_q, k_r)|\mathrm{o}c_i$ = distance between generator k_q in the cluster (q) and generator k_r in the cluster (r) for the representative operating condition $\mathrm{o}c_i$, as defined in (34).

Considering the definitions presented above, a clustering process to achieve the identification of coherent generators is proposed. The detailed flowchart of this stage is shown in Figure 22.

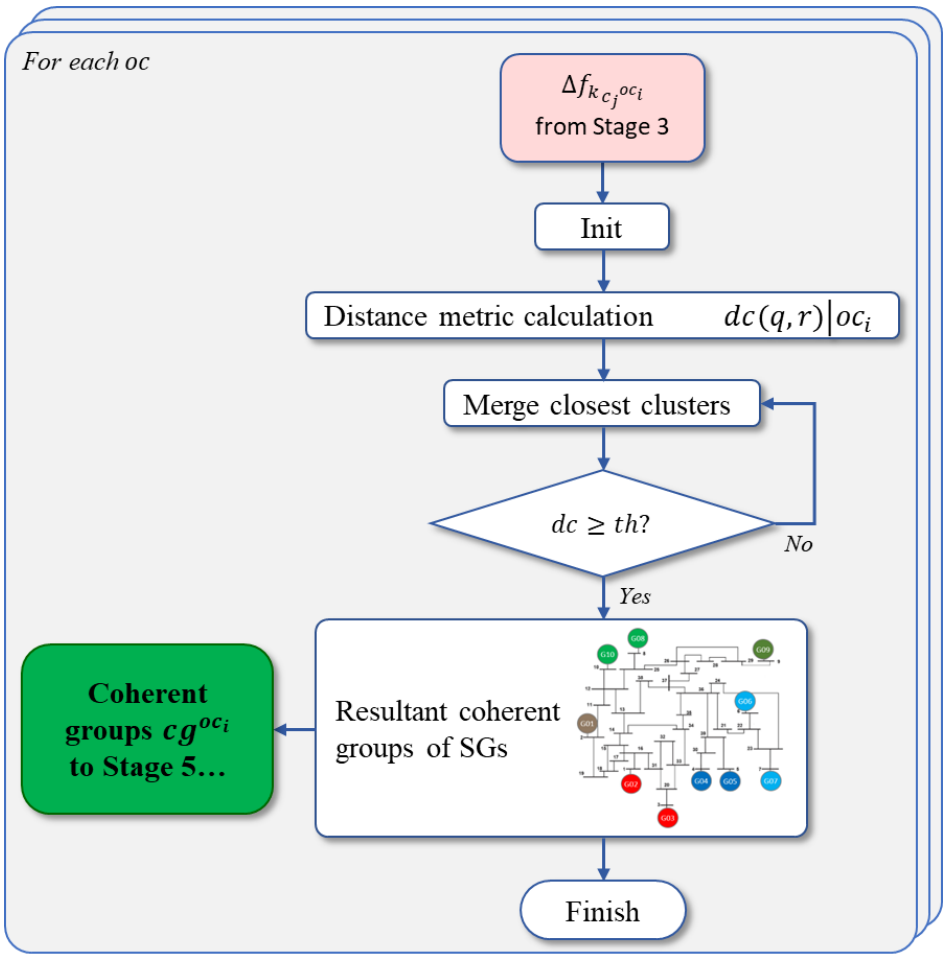

Figure 22: Methodological flowchart | Stage 4.

For a K-generators system and each representative operating condition oc_i, the process begins having K clusters, each with one SG. On each iteration, $dc(q,r)|oc_i$ is calculated for all distinct pairs of clusters. Then, those with smaller values of dc, i.e., the closer clusters, are merged into a single cluster. This process is repeated until a stopping criterion is met. In this case, the algorithm stops when the distance metric dc reaches a global threshold th. This criterion ensures that the minimum coherency required to consider a set of generators into the same group is the same for all the analyzed operating points.

The magnitude of the threshold th is a hyper-parameter, and it is system dependent. There is a lack of reference values in the literature about this specific parameter. Consequently, an empiric value is considered that leads to reasonable results in terms of the number of clusters identified for all the operating conditions oc_i.

Finally, for each operating condition oc_i, G groups of coherent SGs are obtained. Formalizing, a single resulting coherent group x is defined as a set that contains at least one SG (in the case that a SG was not merged with any other machine) and at most K SG (in the case that all the SGs were merged into a single cluster) and is denoted as ${cg_x}^{oc_i} \in \{cg_1^{oc_i}, {cg_2}^{oc_i}, \dots, {cg_G}^{oc_i}\}$. For the sake of simplicity, the set $\{cg_1^{oc_i}, {cg_2}^{oc_i}, \dots, {cg_G}^{oc_i}\}$, i.e., the set that contains all the resulting coherent groups for operating condition oc_i is henceforth called a **layout** and denoted by $l^{oc_i} \Leftrightarrow \{cg_1^{oc_i}, {cg_2}^{oc_i}, \dots, {cg_G}^{oc_i}\}$.

3.5 Stage 5: Identification of coherent f-areas

This stage aims to extend the result of Stage 4, i.e., the coherent groups of SGs, to coherent frequency areas. In practice, this means associating each network busbar into one coherent group. Since real BPSs can have several thousands of busbars, a subset of the most representative busbars can be selected if necessary to keep the problem computationally inexpensive. For instance, classify every busbar that belongs to the highest voltage levels or the main transmission links.

Figure 23 shows the resultant coherent areas after applying the Stage 3 to the same example shown in Figure 21. Note that each busbar is colored following the coherent group of SGs with the strongest influence on its frequency dynamic.

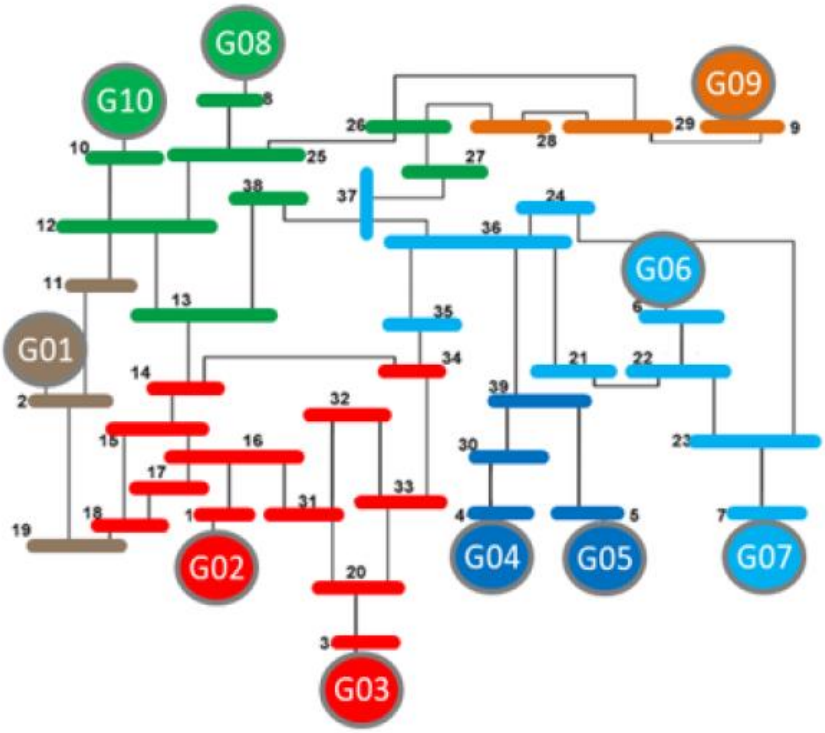

Figure 23: Example of the result of Stage 5 | Resultant coherent areas in the IEEE 39-bus system.

The idea is to include every busbar b on one of the coherent group of generators previously identified on Stage 2 according to the dynamic response of the busbar frequency. For this purpose, a relationship between each busbar's frequency and the frequency of each group of coherent SGs ${cg_x}^{oc_i}$ is needed. As described in section 2.4.1, theFrequency Divider formula proposed by authors on [27] can be used for this purpose. It provides an expression to estimate the frequency of a particular busbar *b* as a linear combination of the frequencies of all the SGs (which act as boundary conditions), where the linear coefficients c_k depends on the augmented admittance matrix of the system [27][3]:

[3] Augmented admittance matrix of the system is calculated as described in section 2.4.1 according to [27].

$$\omega_b(t) = {c_1}^b \cdot \omega_1(t) + {c_2}^b \cdot \omega_2(t) + \cdots + {c_k}^b \cdot \omega_k(t) + \cdots + {c_K}^b \cdot \omega_K(t) \quad (36)$$

where

- $\omega_b(t)$ = estimated frequency of the busbar b in rad/s.
- $\omega_k(t)$ = frequency (or speed) of SG k in rad/s.
- ${c_k}^b$ = coefficient that represents the influence of generator k on the frequency of busbar b. This coefficient depends on the augmented admittance matrix of the system.

An algorithm to identify coherent frequency areas is proposed based on the definitions presented above. The detailed flowchart of this stage is shown in Figure 24.

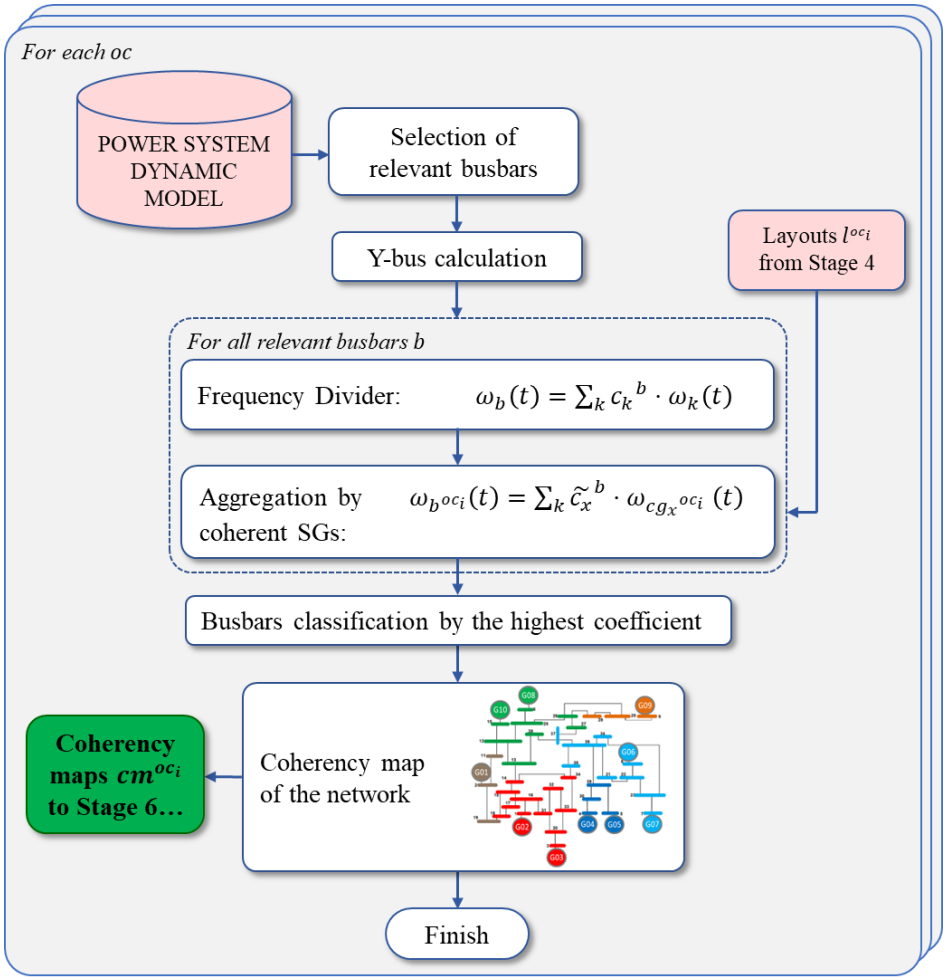

Figure 24: Methodological flowchart | Stage 5.

From (36), it is assumed that the frequency of the SGs that belongs to the same coherent group ${cg_x}^{oc_i}$ is approximately the same, and it is equal to the COI-based frequency for them $\omega_{cg_x{}^{oc_i}}$:

$$\forall k_1, k_2 \in \{1 \dots K\}\, \omega_{k_1} \approx \omega_{k_2} = \omega_{cg_x{}^{oc_i}}, \;\; if \;\; \exists cg_x{}^{oc_i} \in l^{oc_i}: k_1, k_2 \in cg_x{}^{oc_i} \quad (37)$$

where

- $\omega_{cg_x{}^{oc_i}}$ = COI-based frequency of the coherent group $cg_x{}^{oc_i}$, which is defined as in equation (38):

$$\omega_{cg_x^{oc_i}} = \frac{\sum_{\forall k \in cg_x^{oc_i}} (H_k \cdot \omega_k)}{\sum_{\forall k \in cg_x^{oc_i}} (H_k)} \quad (38)$$

By applying the assumption defined through equation (37) to the Frequency Divider formula (36), the coefficients of generators that belong to the same group can be aggregated as follows:

$$\widetilde{c_x}{}^b = \sum_{\forall k \in cg_x^{oc_i}} c_k{}^b \quad (39)$$

Thus, the formula becomes an estimation of the frequency of a particular busbar b as a linear combination of the frequencies of all the coherent groups of SGs:

$$\omega_{b}{}^{oc_i}(t) = \widetilde{c_1}{}^b \cdot \omega_{cg_1{}^{oc_i}}(t) + \cdots + \widetilde{c_x}{}^b \cdot \omega_{cg_x{}^{oc_i}}(t) + \cdots + \widetilde{c_G}{}^b \cdot \omega_{cg_G{}^{oc_i}}(t) \quad (40)$$

Thus, the new coefficients $\widetilde{c_x}{}^b$ represent a measure of the proximity of the frequency of a particular busbar *b* to the COI-based frequency of each coherent group of SGs. Finally, each busbar is classified within the group that obtains the highest coefficient, i.e., the group that most influences its frequency dynamic. Thus, the result of coherent f-areas as in Figure 23 is obtained.

Formalizing, a single group of coherent busbars (coherent f-area) x is defined as a set that contains at least one busbar and at most B (in the case of a B-busbars system) and is denoted as $ca_x^{oc_i} \in \{ca_1^{oc_i}, ca_2{}^{oc_i}, \dots, ca_G{}^{oc_i}\}$. Finally, the set $\{ca_1^{oc_i}, ca_2{}^{oc_i}, \dots, ca_G{}^{oc_i}\}$, i.e., the set that contains all the resulting coherent f-areas for operating condition oc_i is henceforth called the **coherency map** of the network and denoted by $cm^{oc_i} \Leftrightarrow \{ca_1^{oc_i}, ca_2{}^{oc_i}, \dots, ca_G{}^{oc_i}\}$.

3.6 Stage 6: Determination of f-robustness level

The objective of this stage is to quantify the level of f-robustness of each coherent f-area obtained in the previous stage for all operating conditions oc_i. For this purpose, particular effects that threaten the dynamic response of local frequency are specified in the following. As introduced in Chapter 1, future BPSs with an uneven spatial distribution of inertia are more prone to deteriorate the local behavior of the frequency at weaker areas, leading to the following consequences:

After a sudden ΔP contingency on a weak area:

1. Its local frequency presents a higher RoCoF than other regions that concentrate more inertia.

2. The amplitude of its local frequency oscillations around the global COI-based frequency is more prominent than in other regions that concentrate more inertia.

Both consequences are highly influenced by two key factors: **inertia** and its **spatial distribution.** In the following, comprehensive indexes to characterize the f-robustness in terms of these factors are derived through an analytical approach.

The analytical derivation is first focused on finding an index to represent the effect of inertia on the dynamic behavior of the frequency of **a particular busbar**. Then, the f-robustness index for each area is simply obtained by calculating an average over all the busbars that belong to that area.

As presented by the authors on [26] at the beginning of their inertia distribution model, analytical derivation begins assuming a swing-like equation for the frequency of each busbar. This equation postulates a fundamental psychical law that indicates that there is an inverse relationship between the rate of change of the frequency and the effect of the inertia at a particular busbar *b*:

$$\frac{d\Delta\omega^b(t)}{dt} = \frac{1}{2H_{eq}^b} \cdot \left(\Delta P_g^b(t) - \Delta P_l^b(t)\right) \quad (41)$$

where

- $\omega^b(t)$ = frequency of busbar b in pu.
- $P_g^b(t)$ and $P_l^b(t)$ = generated and consumed power at busbar b in pu.
- H_{eq}^b = equivalent effect of the inertia at busbar b in s.

As described in previous section 3.5, the frequency of a particular busbar b can be estimated as a linear combination of the COI-based frequency of all the coherent groups of SGs:

$$\omega_{b^{oc_i}}(t) = \sum_{x\in\{1\dots G\}} \widetilde{c_x}^b \cdot \omega_{cg_x{}^{oc_i}}(t) \quad (42)$$

Equation (42) also holds for the deviation of the frequency from its nominal value:

$$\Delta\omega_{b^{oc_i}}(t) = \sum_{x\in\{1\dots G\}} \widetilde{c_x}^{\,b} \cdot \Delta\omega_{cg_x{}^{oc_i}}(t) \quad (43)$$

Applying the time derivative on both sides of (43):

$$\frac{d\Delta\omega_{b^{oc_i}}(t)}{dt} = \sum_{x\in\{1\dots G\}} \widetilde{c_x}^{\,b} \cdot \frac{d\Delta\omega_{cg_x{}^{oc_i}}(t)}{dt} \quad (44)$$

By replacing equation (41) on the left side of (44):

$$\frac{1}{2H_{eq}^{b\ oc_i}} \cdot \left(\Delta P_g^b(t)^{oc_i} - \Delta P_l^b(t)^{oc_i}\right) = \sum_{x\in\{1\dots G\}} \widetilde{c_x}^{\,b} \cdot \frac{d\Delta\omega_{cg_x{}^{oc_i}}(t)}{dt} \quad (45)$$

$\Delta P_g^b(t)$ can be simplified by 0 during the inertial response:

$$\frac{-\Delta P_l^b(t)^{oc_i}}{2H_{eq}^{b\ oc_i}} = \sum_{x\in\{1\dots G\}} \widetilde{c_x}^{\,b} \cdot \frac{d\Delta\omega_{cg_x{}^{oc_i}}(t)}{dt} \quad (46)$$

Regarding the inner term of the summation, it is assumed that the COI-based frequency (or speed) dynamic of each coherent group $\Delta\omega_{cg_x{}^{oc_i}}(t)$ is governed by a local swing-like equation:

$$\widetilde{c_x}^{\,b} \cdot \frac{d\Delta\omega_{cg_x{}^{oc_i}}(t)}{dt} = \widetilde{c_x}^{\,b} \cdot \frac{(\Delta P_{gx} - \Delta P_{lx})}{2H_{cg_x{}^{oc_i}}} \quad (47)$$

where

- ΔP_{gx} = deviation of the mechanical power (input of synchronous machine) of SGs of group $cg_x{}^{oc_i}$ in pu.
- ΔP_{lx} = deviation of the electrical power (output of synchronous machine) of SGs of group $cg_x{}^{oc_i}$ in pu.
- $H_{cg_x{}^{oc_i}}$ = total inertia constant of SGs of coherent group $cg_x{}^{oc_i}$ in s, defined in equation (48):

$$H_{cg_x{}^{oc_i}} = \sum_{\forall k \in cg_x^{oc_i}} H_k \quad (48)$$

Again, the mechanical power can be assumed constant, therefore, ΔP_{gx} can be simplified by 0 during the inertial response:

$$\tilde{c_x}^b \cdot \frac{d\Delta\omega_{cg_x{}^{oc_i}}(t)}{dt} = \tilde{c_x}^b \cdot \frac{-\Delta P_{lx}}{2H_{cg_x{}^{oc_i}}} \quad (49)$$

By replacing equation (49) on (46):

$$\frac{-\Delta P_l^b(t)^{oc_i}}{2H_{eq}^{b\ oc_i}} = \sum_{x \in \{1 \dots G\}} \tilde{c_x}^b \cdot \frac{-\Delta P_{lx}}{2H_{cg_x{}^{oc_i}}} \quad (50)$$

Considering a sudden contingency, the term $-\Delta P_l$ instantaneously represent the magnitude of the active power imbalance. By neglecting the effect of the transmission losses, it is assumed that its effect is approximately the same no matter the system's location. In consequence, $\Delta P_{l1} \approx \Delta P_{l2} \approx \cdots \approx \Delta P_{lG} = \Delta P_l^b$. This simplification leads to:

$$\frac{-\Delta P_l^b(t)^{oc_i}}{2H_{eq}^{b\ oc_i}} = \frac{-\Delta P_l^b(t)^{oc_i}}{2} \sum_{x \in \{1 \dots G\}} \tilde{c_x}^b \cdot \frac{1}{H_{cg_x{}^{oc_i}}} \quad (51)$$

By simplifying some terms:

$$\frac{1}{H_{eq}^{b\ oc_i}} = \sum_{x \in \{1 \dots G\}} \tilde{c_x}^b \cdot \frac{1}{H_{cg_x{}^{oc_i}}} \quad (52)$$

Equation (52) defines the effect of the inertia at busbar b. It depends on two key factors:

- The inertia of each coherent group of SGs through the term $H_{cg_x{}^{oc_i}}$.
- The topology of the system through the coefficients $\tilde{c_x}^b$ that come from the augmented admittance matrix of the system.

Thus, **the equivalent effect of the inertia at busbar *b* is interpreted as a kind of a parallel of all the coherent group's total inertias present on the system $H_{cg_x{}^{oc_i}}$ but influenced by the topology through coefficients $\tilde{c_x}^b$.** The result is coherent with the expression (19) that authors

in [26] derived for their online method to assess the spatial distribution of the inertia, as described in section 2.3.2.

Based on the analytical derivation presented above, an algorithm to achieve the determination of the f-robustness level of each coherent f-areas for all operating conditions oc_i is proposed. The detailed flowchart of this stage is shown in Figure 25.

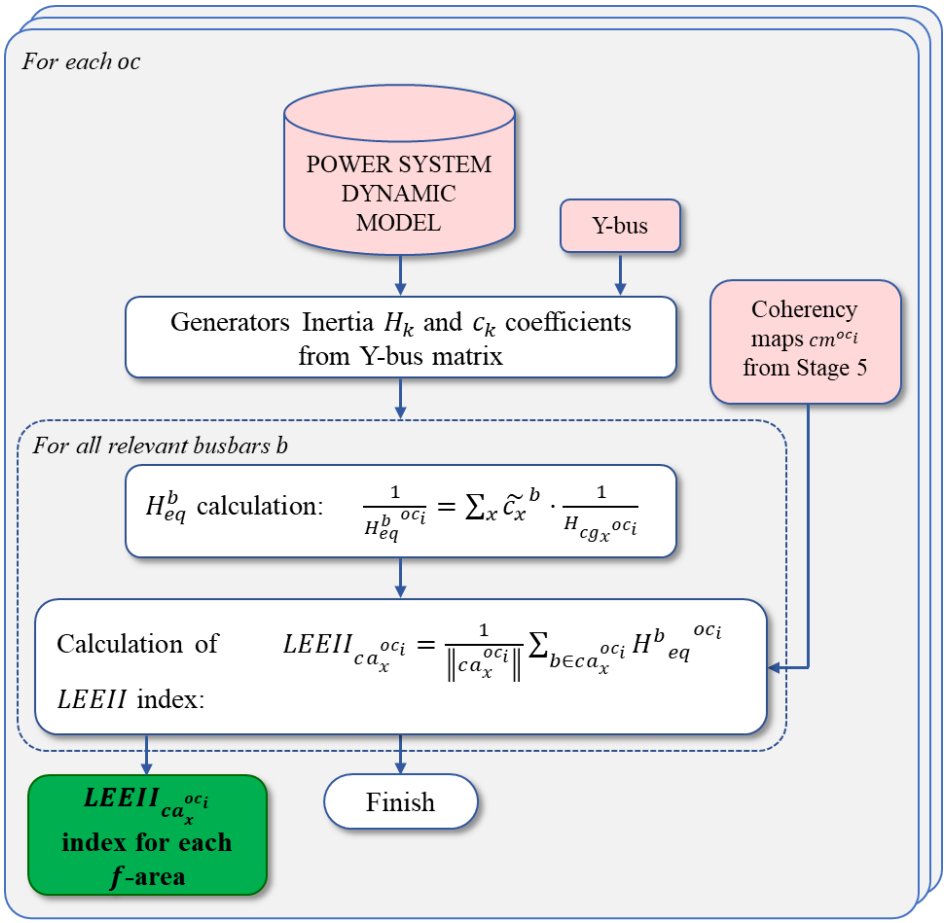

Figure 25: Methodological flowchart | Stage 6.

Finally, to get a metric to quantify the f-robustness index for each f-area, the **Local equivalent effect of inertia index** (LEEII) is defined by calculating the average of the result of equation (52) for each busbar that belongs to each area:

$$LEEII_{ca_x^{oc_i}} = \frac{1}{\|ca_x^{oc_i}\|} \sum_{b \in ca_x^{oc_i}} H^b_{\ eq}{}^{oc_i} \qquad (53)$$

where

- $LEEII_{ca_x^{oc_i}}$ = LEEII index for f-area $ca_x^{oc_i}$ for representative operating condition oc_i.
- $\|ca_x^{oc_i}\|$ = number of busbars that belong to f-area $ca_x^{oc_i}$ for representative

operating condition oc_i.

4 Study Case

This chapter presents a description of the study case used to test and validate the proposed index. The power system analyzed corresponds to the Chilean National Electric System (Chilean NES), considering the generation and transmission planning to the end of 2022. The system covers almost the entire national territory, feeding 98,5% of the population [38]. The total capacity is around 36,2 GW, composed of 73% synchronous generation and 27% CIGTs. Figure 26 shows the total installed capacity by technology [40]:

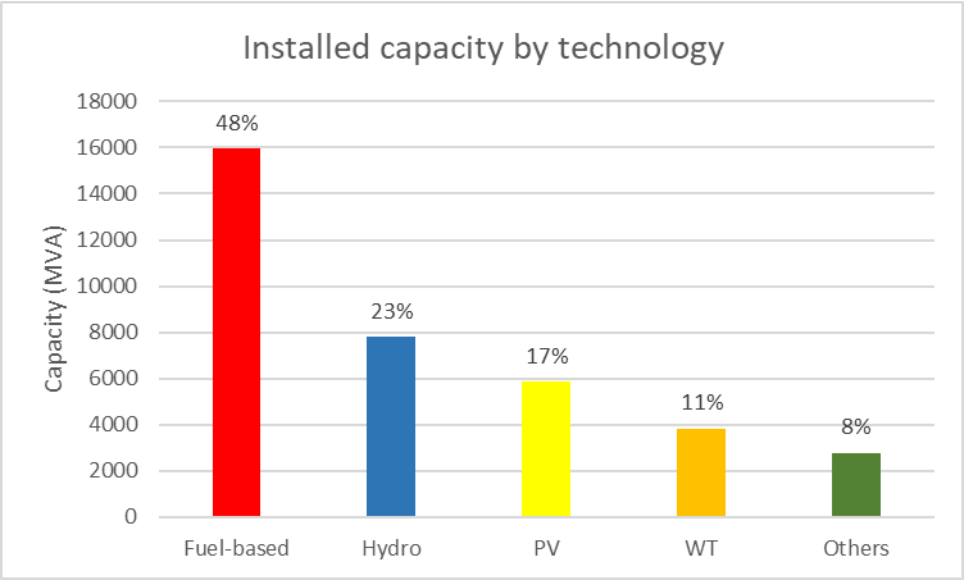

Figure 26: Installed capacity by technology in the Chilean National Electric System.

4.1 System characteristics

Due to the country's unique geography, it is a very long and low-meshed system that reaches 2700 km from North to South. Figure 27 shows a map of the transmission system of the Chilean NES, including the transmission lines above 66 kV. Figure 28 shows a map that includes the locations of the generation's facilities of the Chilean NES. Statistics of installed capacity of SGs and CIGTs for the country's North, Mid and South regions are also included.

Following global tendencies, the energy matrix of the Chilean NES is replacing its fuel-based generation with CIGTs at a rapid pace. Chilean environmental policy aims to eliminate coal-based generation by 2040 entirely. In addition, renewable energies goals are set to cover at least 60% of the installed capacity of CIGTs by 2035 and 70% by 2050 [39]. It is also expected that hydro power plants will remain in the future. Consequently, the future Chilean NES will have almost all its synchronous generation concentrated in the country's Mid and South regions, while CIGTs will dominate the North.

The aforementioned system's evolution is already occurring: the total inertia is getting lower as fuel-based generation is going out of service, and the remaining synchronous generation is getting concentrated in the Mid and South. Consequently, it is expected that stability concerns due to the low and uneven concentrated inertia will become more frequent and more threatening in the upcoming years.

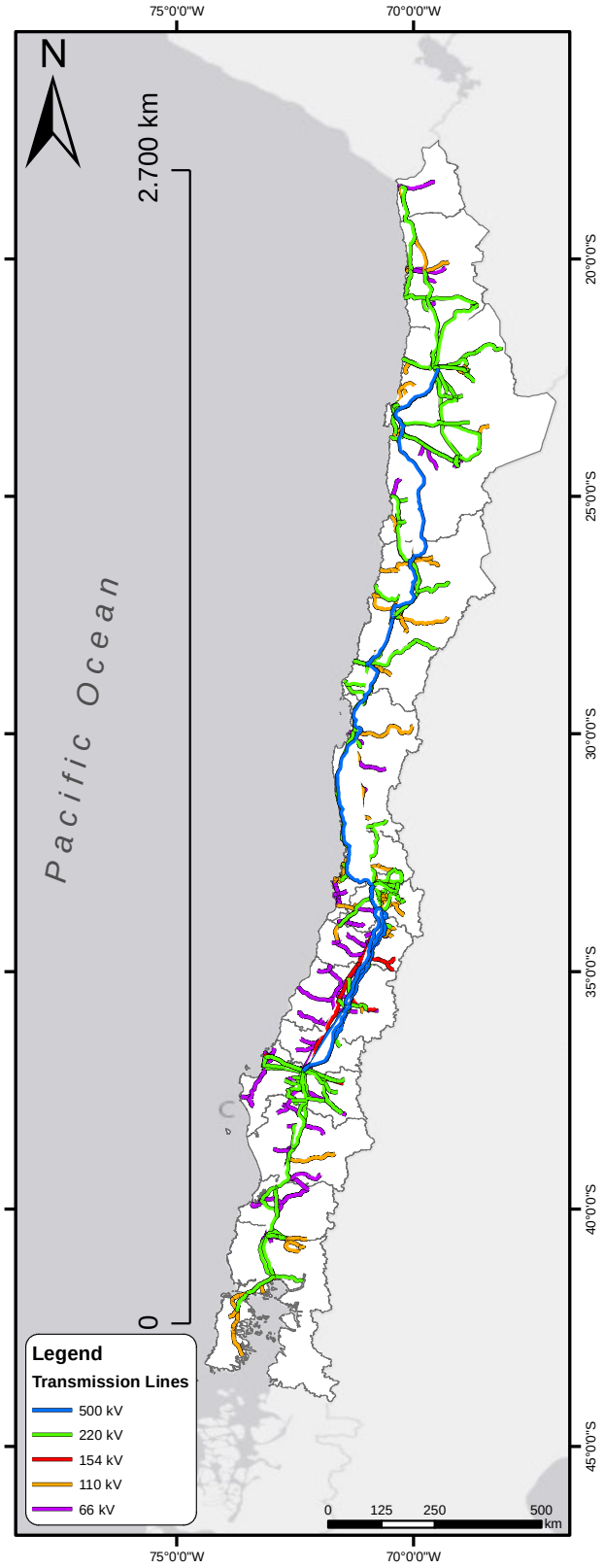

Figure 27: Transmission system of the Chilean NES.

Installed Capacity Distribution by Tech:

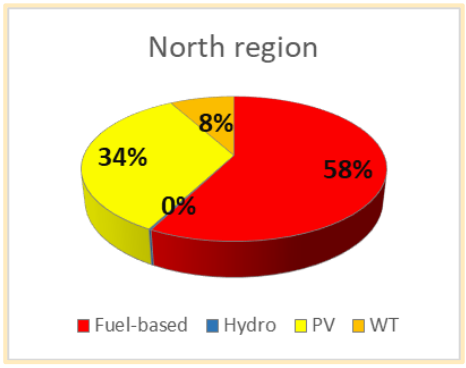

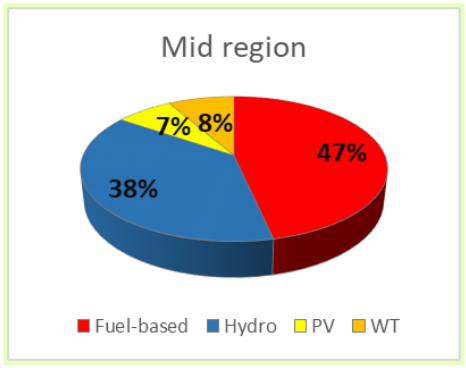

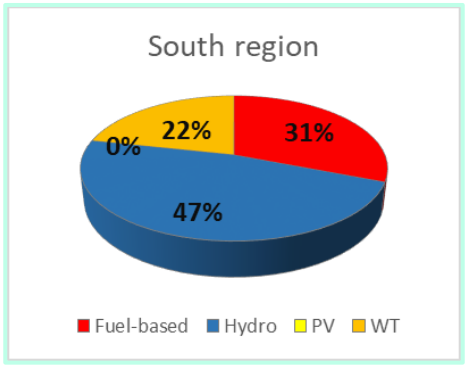

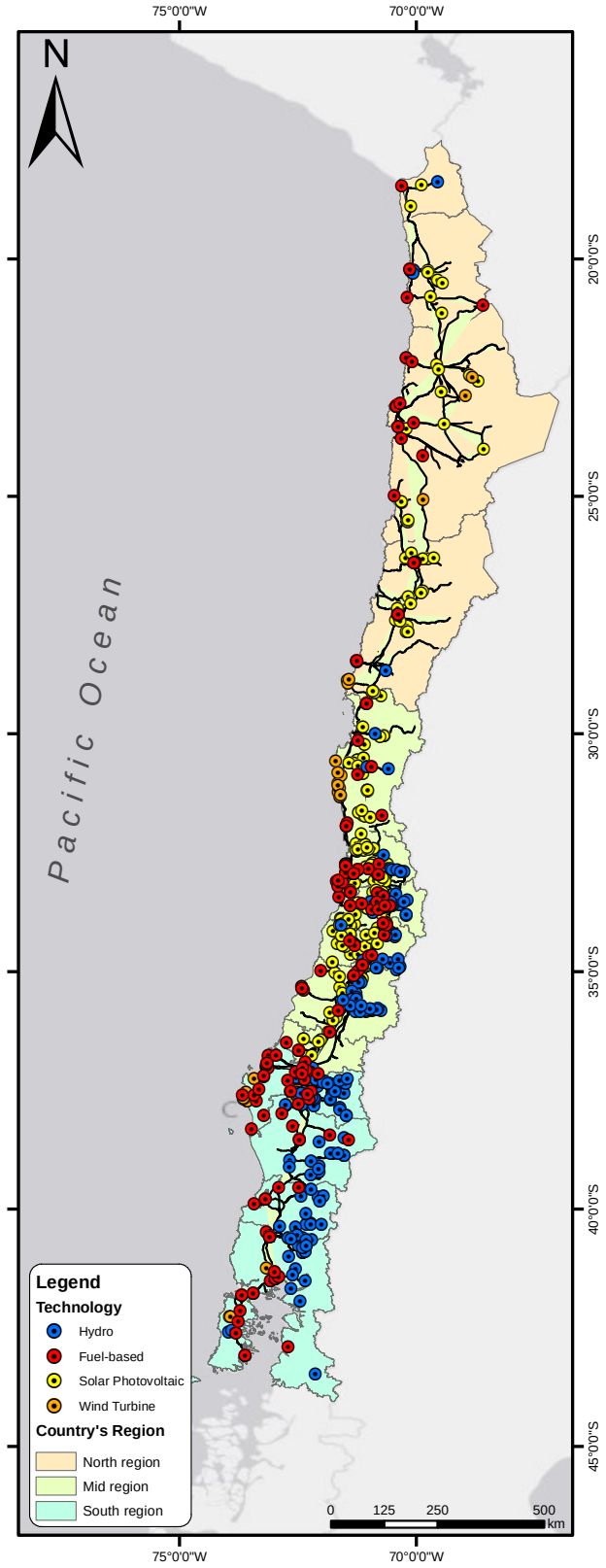

Figure 28: Generation system of the Chilean NES.

4.2 Power system's dynamic model

The Chilean TSO publishes a DIgSILENT Power Factory RMS model of the Chilean NES regularly [40]. In this project, the last available model was modified, including all the expected system changes up to December 2022, considering the generation and transmission planning. The resulting model is used to implement the methodology described in chapter 3, and it is composed by:

- 18102 busbars.
- 406 SGs.
    - 254 machines with a dynamic model.
    - 150 machines are usually dispatched.
- 116 CIGTs without contribution to frequency regulation.
- 32284 km of high voltage transmission lines (>110 kV).

4.3 Operating conditions

A set of operating conditions must be defined to implement the proposed methodology and assess the system's dynamic behavior. For this purpose, a market simulation of the 8760 hours for the operation of 2022 is done according to stage 1. Then, all the possible operating points are grouped in a few representative operating conditions from the clustering analysis described in section 3.2. In this case, six representative operating points are selected and divided into two sets:

- Training set: Five representative operating conditions used to **train (develop)** the proposed tool. They are used to run stages 1 to 6, leading to the calculation and storage of the proposed LEEII index of each f-area depending on the unit commitment.
- Validation set: A representative operating condition used to **validate** the proposed tool. It is used to evaluate the performance of the proposed LEEII index in terms of its accuracy in identifying local weakness of f-areas.

The main characteristics of the representative operating conditions are shown in Table 4:

Generation Dispatch	Total Demand (MW)	CIGTs Generation (MW)	Net Demand (MW)	Total Inertia (GVAs)	Inertia by region (GVAs)		
					North	Mid	South
gd_1 (T)	9254	5640	3614	33	12,1	12,5	8,8
gd_2 (T)	7464	1635	5830	41	16,0	14,4	10,0
gd_3 (T)	9720	4926	4794	32	11,2	11,9	8,9
gd_4 (T)	7995	956	7040	40	16,1	14,7	9,7
gd_5 (T)	9395	4637	4758	35	11,7	14,7	9,1
gd_6 (V)	8867	4905	3963	37	15,1	13,1	8,4
(T) Train set, (V) Validation set.							

Table 4: Representative operating conditions used.

5 Results and Discussion

This chapter presents the results of implementing the proposed methodology to the Chilean NES study case described in the previous chapter.

5.1 Tool development

In this section, the results of the training process (development) of the proposed tool are presented. Results of stages 1 and 2 are omitted since their results were already summarized in section 4.3.

5.1.1 Stage 3: Stability Assessment

A set of $N = 5$ operating conditions $\{oc_1, oc_2, oc_3, oc_4, oc_5\}$ corresponding to the Training set described in section 4.3 is considered to execute dynamic simulations using the power system's dynamic model presented in section 4.2. The definition of the set of contingencies is described in the following.

As the data acquired in this stage is used only for coherency identification purposes, a set of non-real sudden load increment events is used instead of simulating real (possible) generation outages. Consequently, additional loads that do not represent real facilities in the Chilean NES were included in the power system's dynamic model in this stage. It facilitates the execution of the same event in terms of the magnitude of the power imbalance and covering the grid homogenously. It is worth noting that real possible generation outages were simulated later in the stage of validation as described in section 5.2.

Thus, the set of contingencies defined is composed of $M = 40$ sudden load increments at different locations according to the map presented in Figure 29. The magnitude of the power imbalance is set to 300 MW, which is 77% of the bigger SG of the system.

Consequently, $N \cdot M = 5 \cdot 40 = 200$ RMS simulations are executed, and the electrical frequency deviation from the nominal value of each SG is recorded. Simulations details are listed below:

- Adapting size time step.
- Simulation time: 6 s.[4]
- Load increment event time: 0,1 s.

[4] Due to the characteristics of the Chilean NES, the frequency Nadir occurs around 5-6 seconds after a sudden power imbalance.

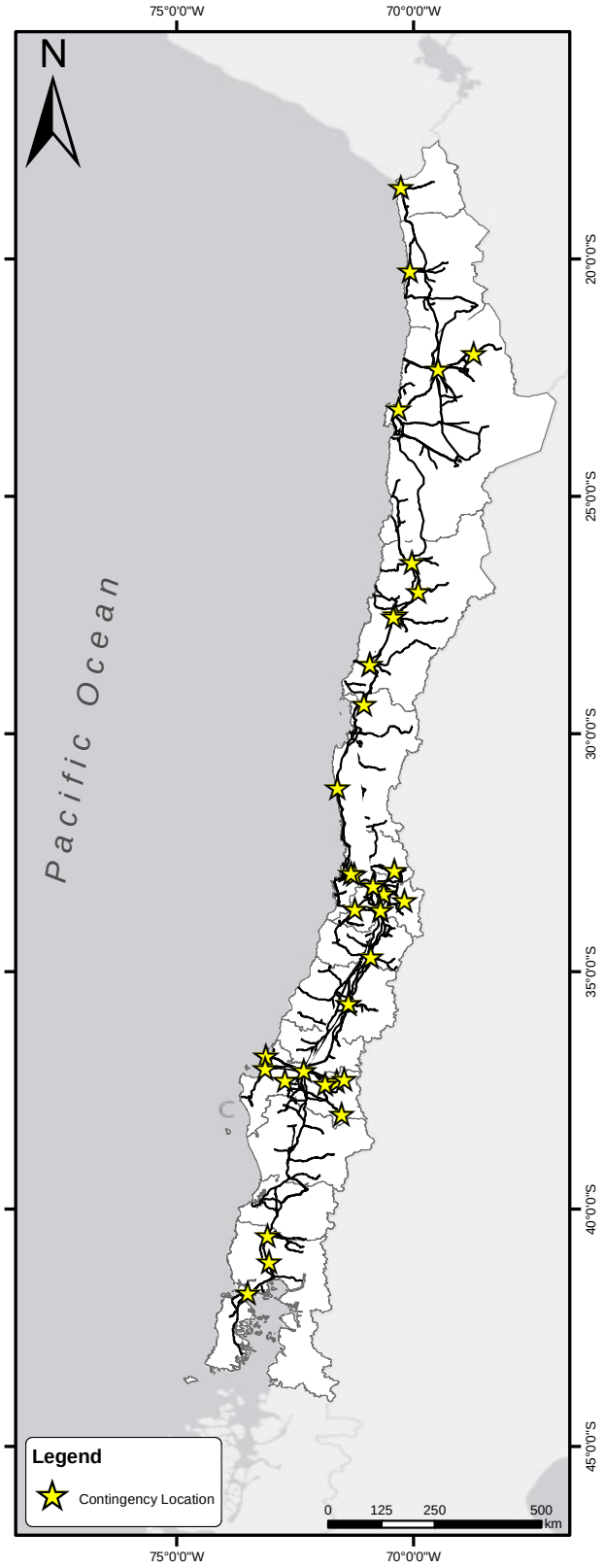

Figure 29: Locations of the 300 MW of load increment contingencies simulated.

5.1.2 Stage 4: Identification of coherent SGs

From the results of the RMS simulations executed in the previous stage, coherent generators are identified for each operating condition $\{oc_1, oc_2, oc_3, oc_4, oc_5\}$ following the methodology described in section 3.4. The threshold used as the criterion to determine the number of clusters is set to 40 mHz.

The resulting layouts on each operating condition are summarized in the following tables, where coherent groups are colored accordingly with figures presented in section 5.1.3.

Coherent Group[5]	Number of SGs	Total H (pu)[6]
cg_0	106	223,91
cg_{12}	3	51,79
cg_{13}	6	31,86
cg_7	9	10,03
cg_2	2	2,17
cg_{11}	3	1,13
cg_{15}	2	0,33
cg_3	3	0,16

Table 5: Resulting layout for oc_1.

Coherent Groups[5]	Number of SGs	Total H (pu)[6]
cg_1	99	225,64
cg_{11}	16	128,04
cg_0	6	32,43
cg_6	7	5,55
cg_4	2	4,48
cg_2	2	2,17
cg_3	3	0,16
cg_{10}	1	<0,01

Table 6: Resulting layout for oc_2.

Coherent Groups[5]	Number of SGs	Total H (pu)[6]
cg_0	104	217,58
cg_{10}	12	86,51
cg_6	8	6,04
cg_2	2	2,17
cg_3	3	0,16

Table 7: Resulting layout for oc_3.

Coherent Groups[5]	Number of SGs	Total H (pu)[6]
cg_0	109	222,23
cg_8	16	134,85
cg_1	16	26,26
cg_5	11	7,06
cg_3	2	4,48
cg_2	2	3,61

Table 8: Resulting layout for oc_4.

Coherent Groups[5]	Number of SGs	H_tot (pu)[6]
cg_0	94	204,87
cg_7	14	100,24
cg_1	21	33,32
cg_4	10	6,57
cg_2	2	4,48
cg_6	3	1,13

Table 9: Resulting layout for oc_5.

It is worth noting that the most significant two coherent groups of all resulting layouts are very similar. On the one hand, the green group concentrates more than 200 pu ($S_{base} = 100\ MVA$)

[5] As all cg_i correspond to the same operating condition oc_i for each table, superscript is omitted for simplicity.
[6] Note that Total H (pu) column is the sum of the inertia of each coherent group in pu $@S_{base} = 100\ MVA$.

of the total inertia and represent the Mid Region of the country almost entirely (see figures presented in section 5.1.3). On the other hand, the red group concentrates around 100 pu ($S_{base} = 100\ MVA$) of the total inertia and represent the North Region of the country entirely in all the cases, except in the operating condition oc_1, where the North is divided into three smaller f-areas (see figures presented in section 5.1.3).

5.1.3 Stage 5: Identification of coherent f-areas

Before identifying coherent f-areas, the augmented admittance matrix is calculated for each operating condition. The assumptions presented in section 2.4.1 are implemented to simplify the calculation. The size of the Y-bus matrix is 18102x18102. Note that it can slightly vary depending on the operating condition because some nodes are out of service in each scenario.

Once Y-bus is obtained for each operating condition oc_i, f-areas are identified by following the methodology described in section 3.5. The resulting coherency maps are presented with their corresponding layouts from Stage 1 in the following figures. Note that the busbars that belong to the same f-area are colored together in the maps and using the color of their corresponding coherent group of SGs accordingly with tables presented in 5.1.2.

The results presented from Figure 30 to Figure 39 show three main f-areas in the Chilean NES. First, the North region of the country (red group in the maps) is connected to the rest of the system radially through a 500 kV link (see Figure 27). This zone operated as a separate system before 2017, where the Chilean NES was unified [37]. Even though today this area concentrates a substantial amount of the system inertia, it comes exclusively from fuel-based generation. Consequently, it is expected that it will become weaker in the future. Second, a huge central f-area (green group in the maps) goes from the interconnection with the northern system to the southern endpoint of the 500 kV transmission system (see Figure 27). Unlike the North region, this area's inertia is composed of a mix of hydro and fuel-based generation. It concentrates around 70% of the system inertia, distributed well throughout the area. This zone is also characterized by a high-meshed topology for Chile's geography since it combines parallel systems of different voltage levels: 500 kV, 220 kV, and lower. It helps to improve the distribution of the inertia's benefits to frequency stability. Finally, the third area is the southern zone of the system, which is characterized by a low-meshed topology and lower voltage levels. It concentrates a relevant amount of inertia that comes mainly from hydro generation facilities.

The three main areas mentioned above are divided into two or more sub-areas depending on each operating condition. For instance, while the North region is divided into three smaller f-areas in the oc_1 (see Figure 2), the southern system is divided into smaller f-areas in the oc_1, oc_2 or oc_5. The Mid region is divided into sub-areas in some cases as well. The more remarkable subdivision arises in oc_2, where a huge part of the northern zone of the Mid region is separated following the influence of three generation plants that are pretty separated from the rest of the mid-located machines (light blue group in Figure 32). Other noticeable subdivisions frequently arise in the middle of the Mid region (pink, purple and yellow groups). It is because of the parallel different voltage systems that compose that part of the system. For instance, the pink area in the oc_5 arise in the 154 kV and 66 kV parallel systems to the main transmission links of the higher voltage levels: 500 kV and 220 kV.

5.1.3.1 Operating condition 1

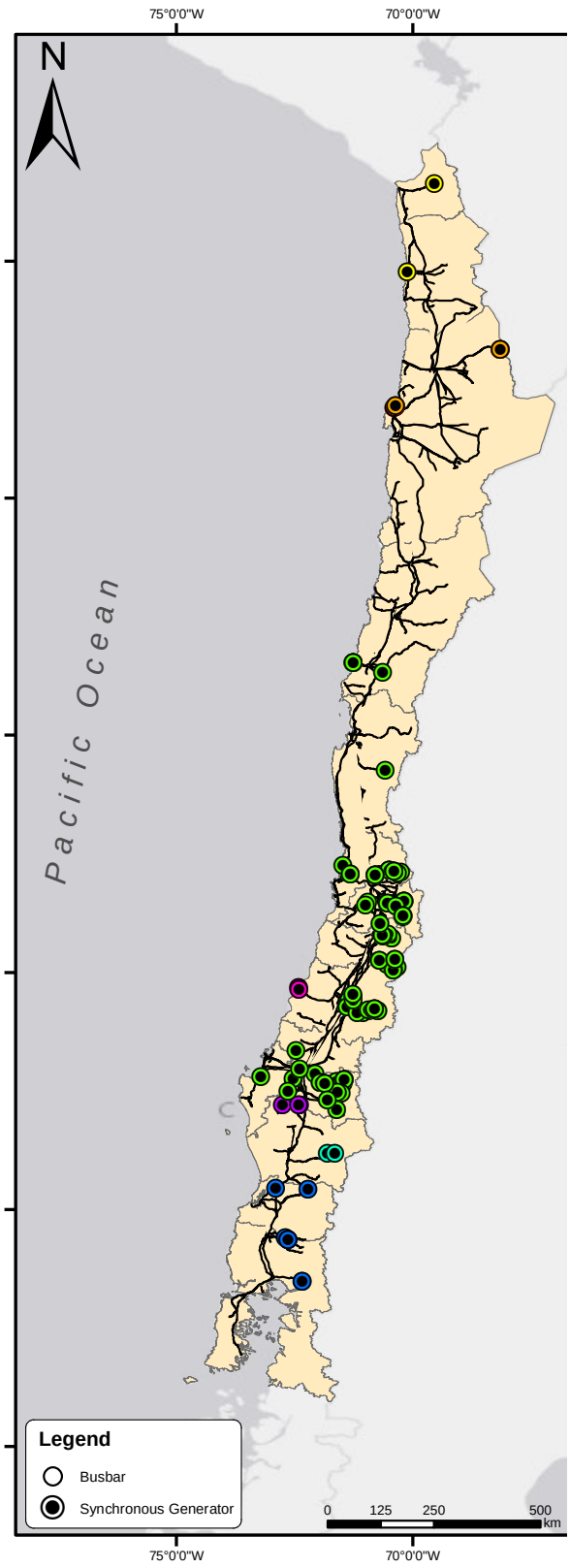

Figure 30: Stage 4 result: Layout for oc_1.

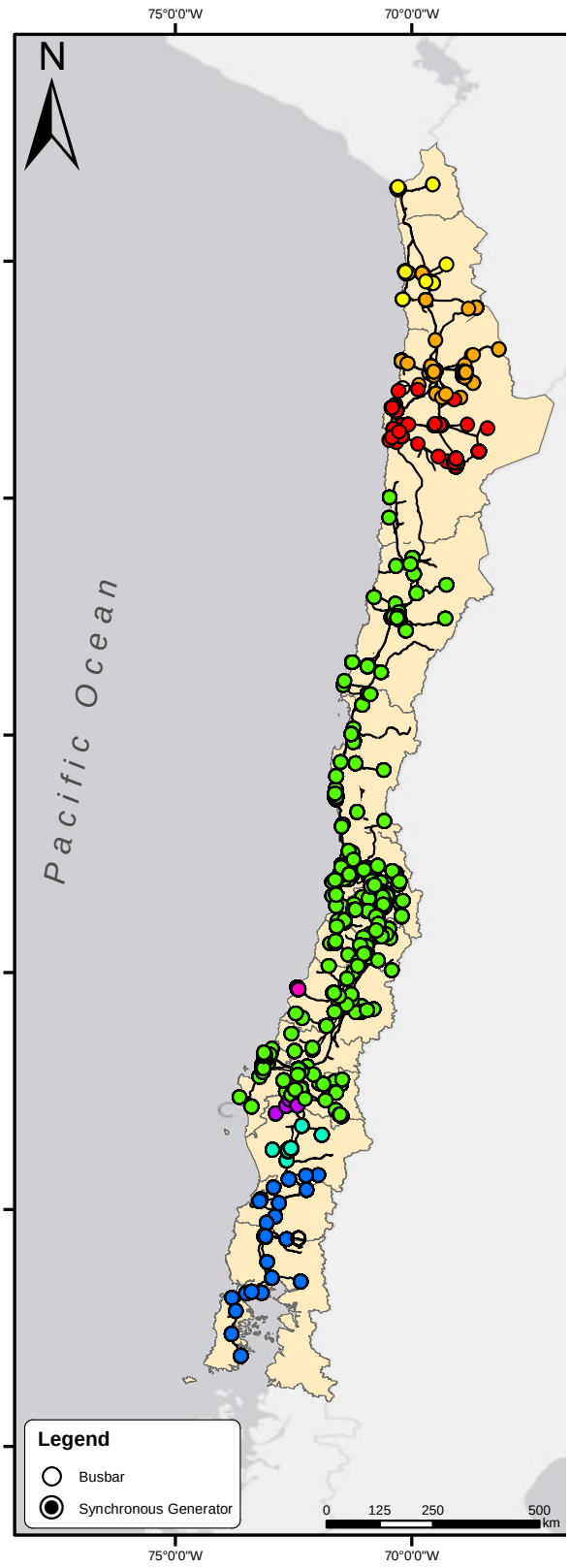

Figure 31: Stage 5 result: Coherency map for oc_1.

5.1.3.2 Operating condition 2

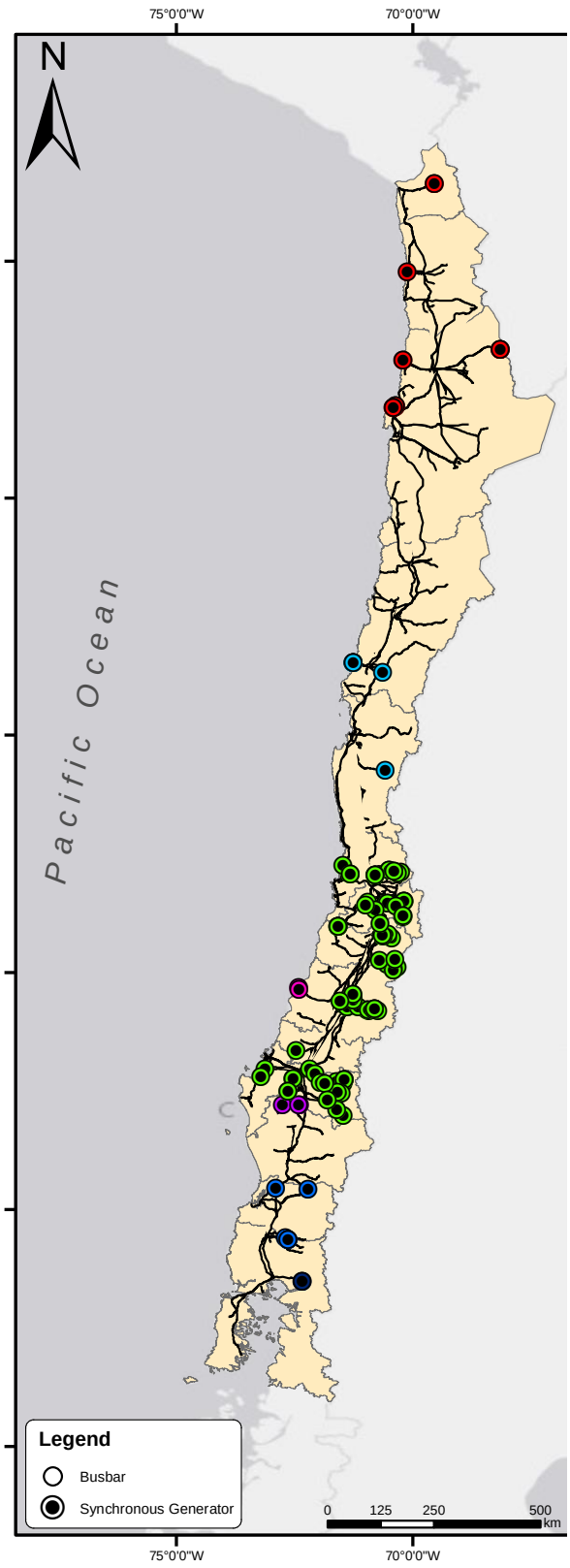

Figure 32: Stage 4 result: Layout for oc_2.

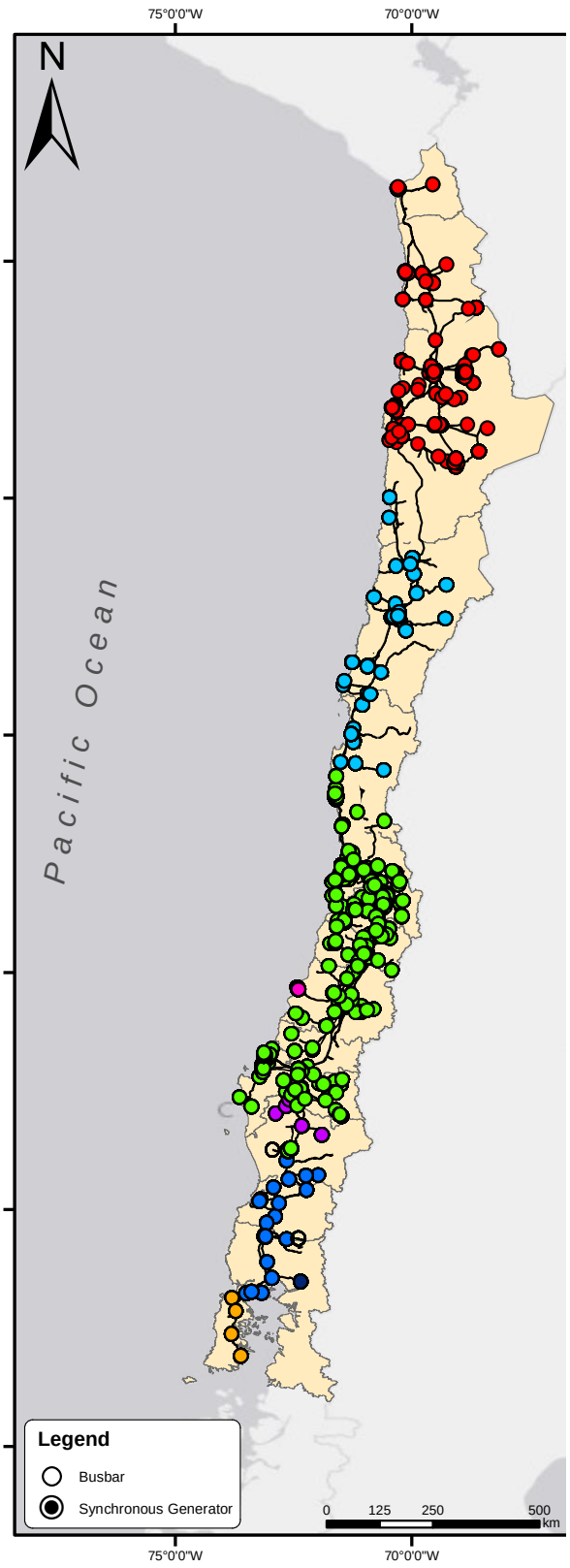

Figure 33: Stage 5 result: Coherency map for oc_2.

5.1.3.3 Operating condition 3

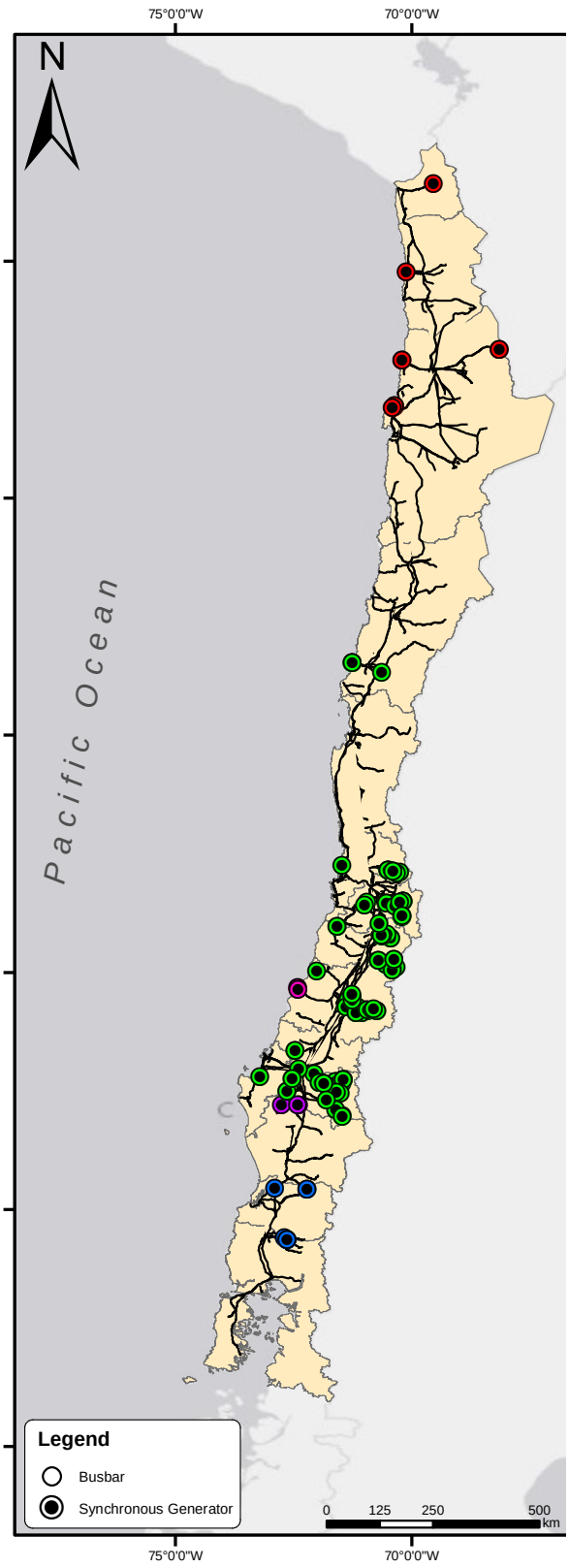

Figure 34: Stage 4 result: Layout for oc_3.

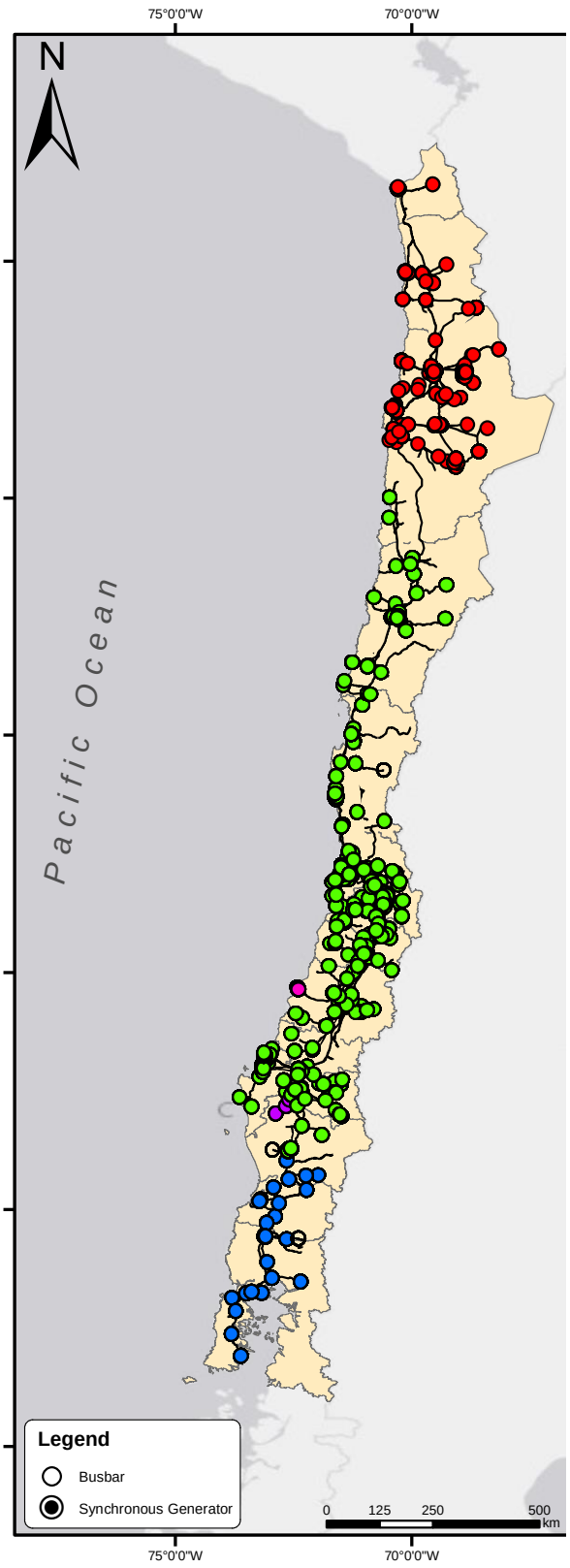

Figure 35: Stage 5 result: Coherency map for oc_3.

5.1.3.4 Operating condition 4

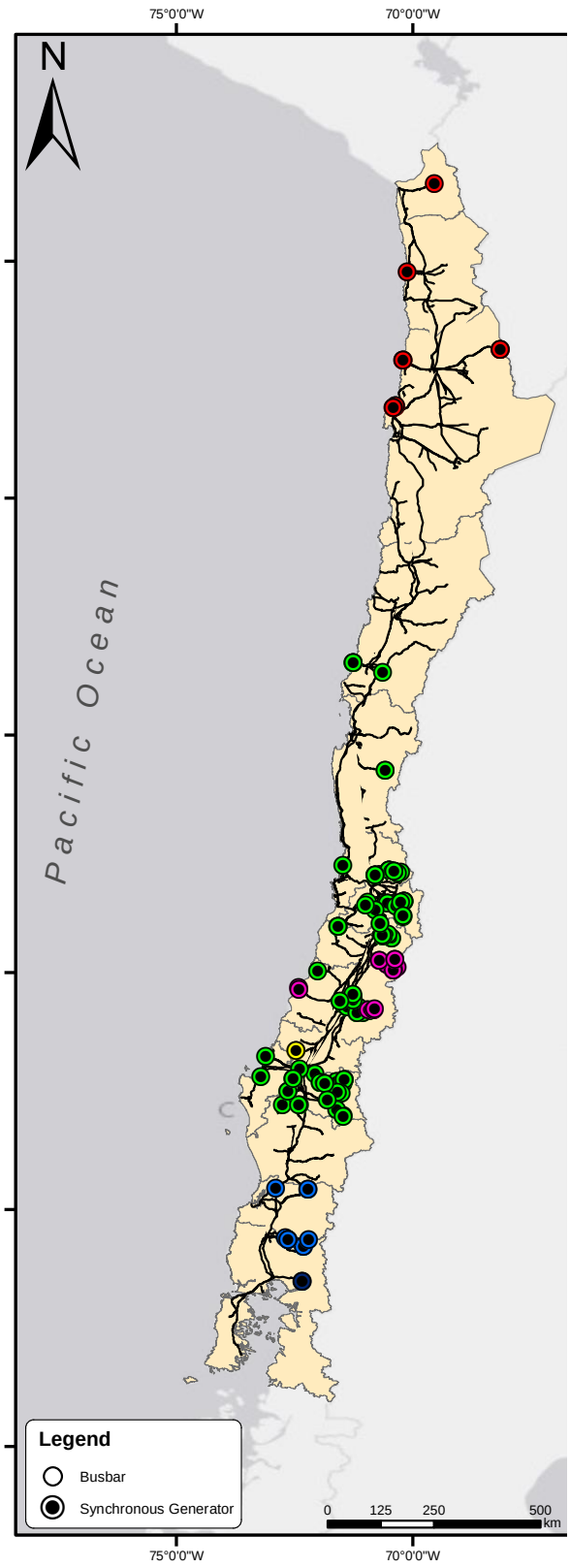

Figure 36: Stage 4 result: Layout for oc_4.

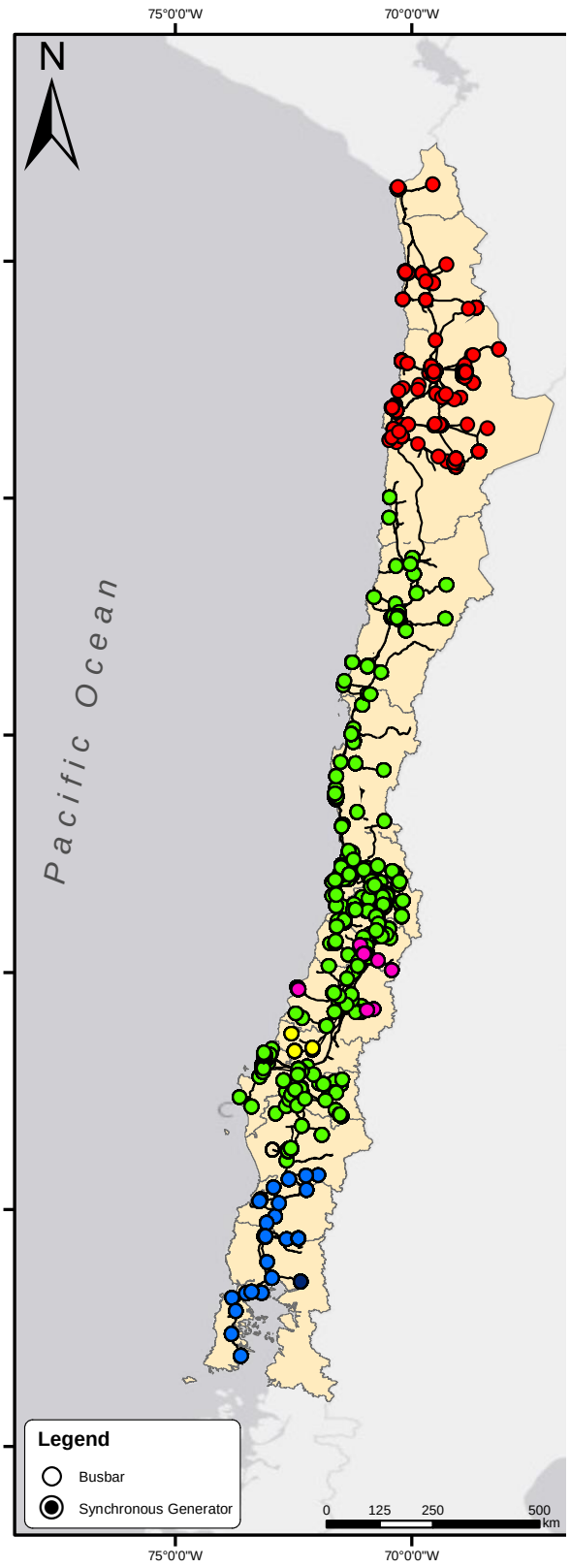

Figure 37: Stage 5 result: Coherency map for oc_4.

5.1.3.5 Operating condition 5

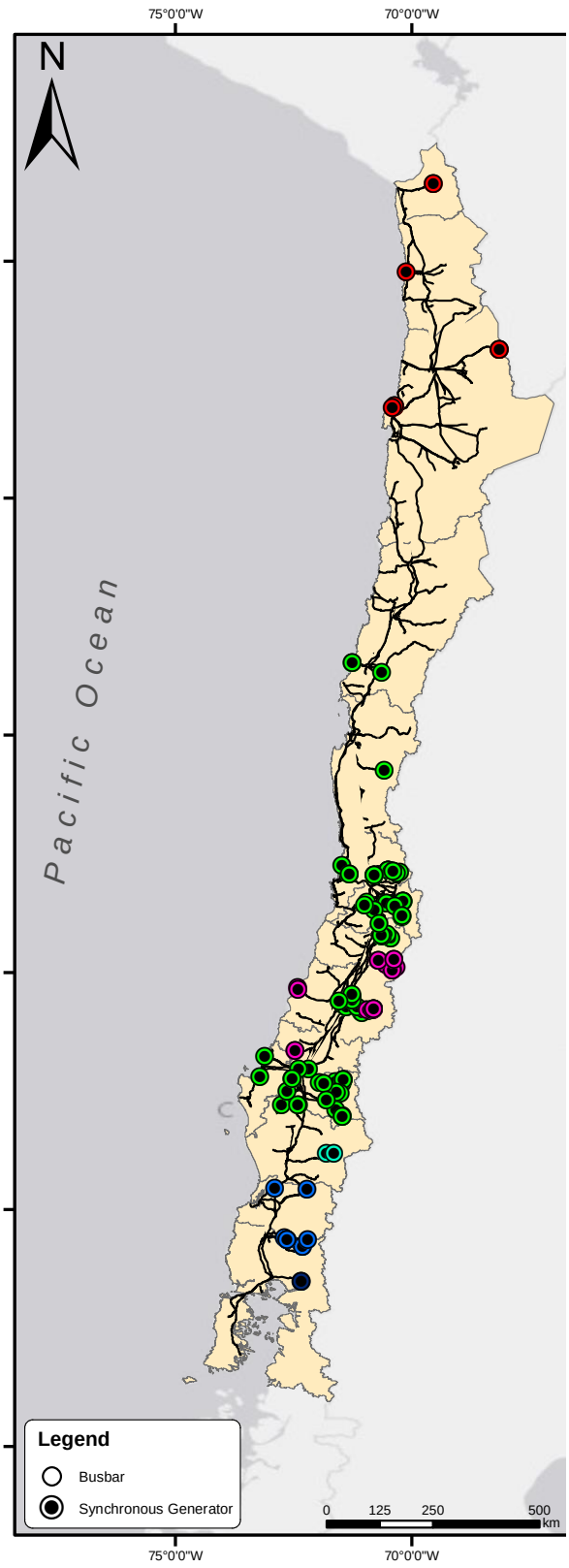

Figure 38: Stage 4 result: Layout for oc_5.

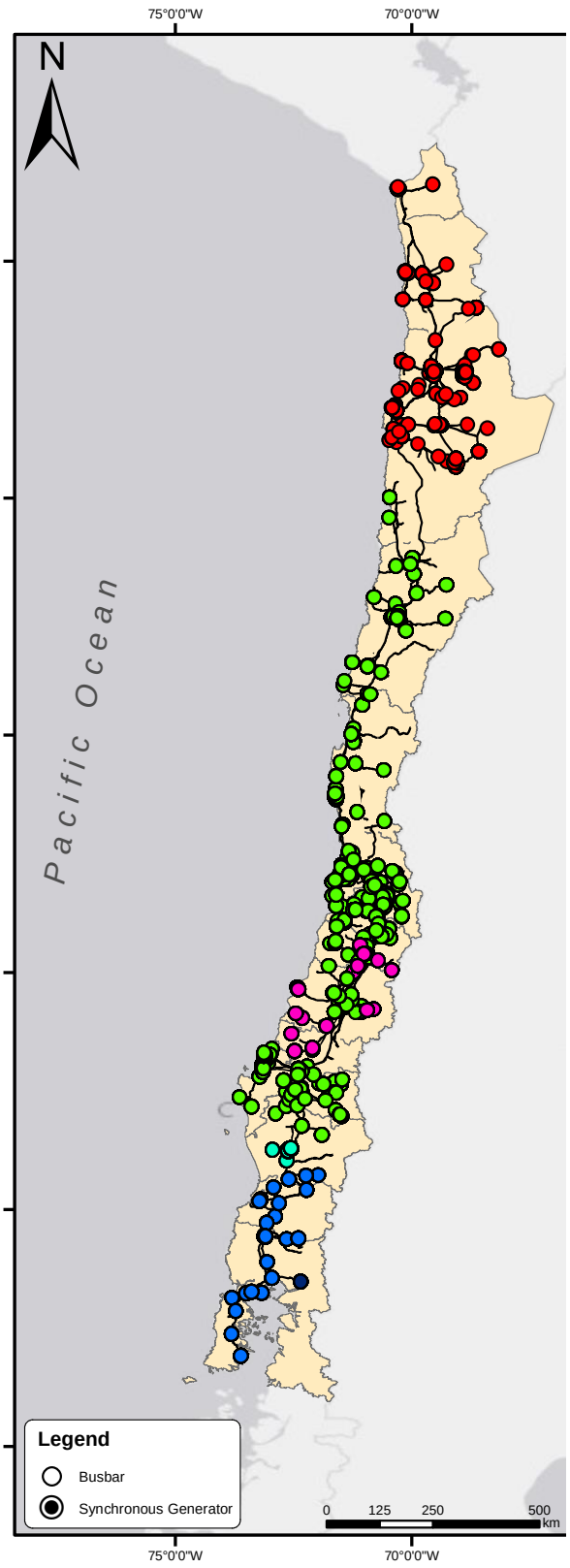

Figure 39: Stage 5 result: Coherency map for oc_5.

5.1.4 Stage 6: Determination of f-robustness level

Once coherent f-areas were obtained by analyzing the operating conditions of the training set, the proposed LEEII index was calculated for each f-area and operating condition implementing the methodology described in 3.6. The resulting LEEII index for each f-area is presented in the following. Since the Y-bus matrix dimension is 18102x18102, it is not practical to show the resulting coefficients $\tilde{c_x}^b$ for each busbar used to calculate the LEEII index according to equations (52) and (53). However, mean coefficients for all busbars of f-areas are included to provide information about the influence of the inertia contained in each area in the LEEII calculation. They are calculated according to equation (54):

$$\bar{c}_{ca_x^{oc_i}} = \frac{1}{\left\| ca_x^{oc_i} \right\|} \cdot \sum_{b \in ca_x^{oc_i}} \tilde{c_x}^b \qquad (54)$$

F-area[7]	Mean Coefficient[7]								LEEII (pu @100 MVA)
	$\bar{c}_{ca_0}$	$\bar{c}_{ca_{11}}$	$\bar{c}_{ca_{12}}$	$\bar{c}_{ca_{13}}$	$\bar{c}_{ca_{15}}$	$\bar{c}_{ca_2}$	$\bar{c}_{ca_3}$	$\bar{c}_{ca_7}$	
ca_0	**0,94**	0,01	0,03	0,00	0,00	0,00	0,01	0,00	18,28
ca_{11}	0,23	**0,53**	0,00	0,00	0,00	0,00	0,01	0,23	1,52
ca_{12}	0,06	0,00	**0,68**	0,20	0,06	0,00	0,00	0,00	6,25
ca_{13}	0,03	0,00	0,28	**0,52**	0,17	0,00	0,00	0,00	2,53
ca_{15}	0,01	0,00	0,14	0,24	**0,61**	0,00	0,00	0,00	0,57
ca_2	0,10	0,00	0,00	0,00	0,00	**0,90**	0,00	0,00	2,40
ca_3	0,24	0,01	0,00	0,00	0,00	0,00	**0,75**	0,00	0,22
ca_7	0,06	0,14	0,00	0,00	0,00	0,00	0,00	**0,80**	3,62

Table 10: Resulting LEEII index and mean coefficients for each area in oc_1.

F-area[7]	Mean Coefficient[7]								LEEII (pu @100 MVA)
	$\bar{c}_{ca_0}$	$\bar{c}_{ca_1}$	$\bar{c}_{ca_{10}}$	$\bar{c}_{ca_{11}}$	$\bar{c}_{ca_2}$	$\bar{c}_{ca_3}$	$\bar{c}_{ca_4}$	$\bar{c}_{ca_6}$	
ca_0	**0,66**	0,24	0,00	0,10	0,00	0,00	0,00	0,00	25,82
ca_1	0,03	**0,94**	0,00	0,00	0,00	0,01	0,00	0,01	30,31
ca_{10}	0,00	0,02	**0,69**	0,00	0,00	0,01	0,13	0,16	0,00
ca_{11}	0,01	0,00	0,00	**0,98**	0,00	0,00	0,00	0,00	119,41
ca_2	0,00	0,10	0,00	0,00	**0,90**	0,00	0,00	0,00	2,41
ca_3	0,00	0,16	0,00	0,00	0,00	**0,71**	0,01	0,11	0,12
ca_4	0,00	0,01	0,03	0,00	0,00	0,01	**0,82**	0,12	0,85
ca_6	0,00	0,09	0,06	0,00	0,00	0,03	0,15	**0,66**	0,09

[7] As all ca_x and $\bar{c}_{ca_x}$ correspond to the same operating condition oc_i for each table, superscript is omitted for simplicity.

Table 11: Resulting LEEII index and mean coefficients for each area in oc_2.

F-area[8]	Mean Coefficient[8]					LEEII (pu @100 MVA)
	$\bar{c}_{ca_0}$	$\bar{c}_{ca_{10}}$	$\bar{c}_{ca_2}$	$\bar{c}_{ca_3}$	$\bar{c}_{ca_6}$	
ca_0	**0,94**	0,02	0,00	0,02	0,01	30,94
ca_{10}	0,02	**0,98**	0,00	0,00	0,00	61,75
ca_2	0,10	0,00	**0,90**	0,00	0,00	2,41
ca_3	0,25	0,00	0,00	**0,70**	0,05	0,24
ca_6	0,11	0,00	0,00	0,03	**0,86**	1,62

Table 12: Resulting LEEII index and mean coefficients for each area in oc_3.

F-area[8]	Mean Coefficient[8]						LEEII (pu @100 MVA)
	$\bar{c}_{ca_0}$	$\bar{c}_{ca_1}$	$\bar{c}_{ca_2}$	$\bar{c}_{ca_3}$	$\bar{c}_{ca_5}$	$\bar{c}_{ca_8}$	
ca_0	**0,90**	0,04	0,01	0,00	0,01	0,04	91,89
ca_1	0,20	**0,80**	0,00	0,00	0,00	0,00	32,35
ca_2	0,16	0,00	**0,84**	0,00	0,00	0,00	4,17
ca_3	0,02	0,00	0,00	**0,81**	0,17	0,00	3,66
ca_5	0,11	0,00	0,00	0,16	**0,73**	0,00	2,30
ca_8	0,03	0,00	0,00	0,00	0,00	**0,97**	134,78

Table 13: Resulting LEEII index and mean coefficients for each area in oc_4.

F-area[8]	Mean Coefficient[8]						LEEII (pu @100 MVA)
	$\bar{c}_{ca_0}$	$\bar{c}_{ca_1}$	$\bar{c}_{ca_2}$	$\bar{c}_{ca_4}$	$\bar{c}_{ca_6}$	$\bar{c}_{ca_7}$	
ca_0	**0,89**	0,05	0,00	0,00	0,01	0,05	108,51
ca_1	0,26	**0,74**	0,00	0,00	0,00	0,00	40,88
ca_2	0,02	0,00	**0,79**	0,15	0,03	0,00	3,95
ca_4	0,09	0,00	0,15	**0,63**	0,13	0,00	3,07
ca_6	0,29	0,01	0,03	0,21	**0,46**	0,00	1,88
ca_7	0,04	0,00	0,00	0,00	0,00	**0,96**	101,53

Table 14: Resulting LEEII index and mean coefficients for each area in oc_5.

Note that in all cases, the highest mean coefficient for each f-area corresponds to the self-influence, i.e., the mean coefficient of the same area (diagonal elements highlighted in bold). It is also worth noting that the second higher mean coefficient for each f-area corresponds to neighboring zones. For instance, the results for the operating condition oc_1 show that the frequency of coherent areas ca_{12}, ca_{13} and ca_{15} is mainly influenced by a combination thereof since they are neighbor zones in the North region of the system (see Table 10 and Figure 40). Further, the vast central zone ca_0 presents a slight influence on the three mentioned f-areas and the farthest (southern) zones ca_2, ca_3, ca_7 and ca_{11} have a negligible coefficient, less than 0,01 (1%). Similar

[8] As all ca_x and $\bar{c}_{ca_x}$ correspond to the same operating condition oc_i for each table, superscript is omitted for simplicity.

mutual influence effects arise between the neighboring zones at the Mid and South regions of the system.

Regarding the LEEII index results, note that, in general, the two largest f-areas in terms of their geographic extension and the amount of inertia they contain are the red and green areas, which represent almost entirely the North and Mid regions of the system, respectively. Both areas show the highest LEEII indexes, and therefore, they are the strongest zones of the Chilean NES. In contrast, the weaker f-areas arise in the South, mainly around small and weekly connected groups of SGs.

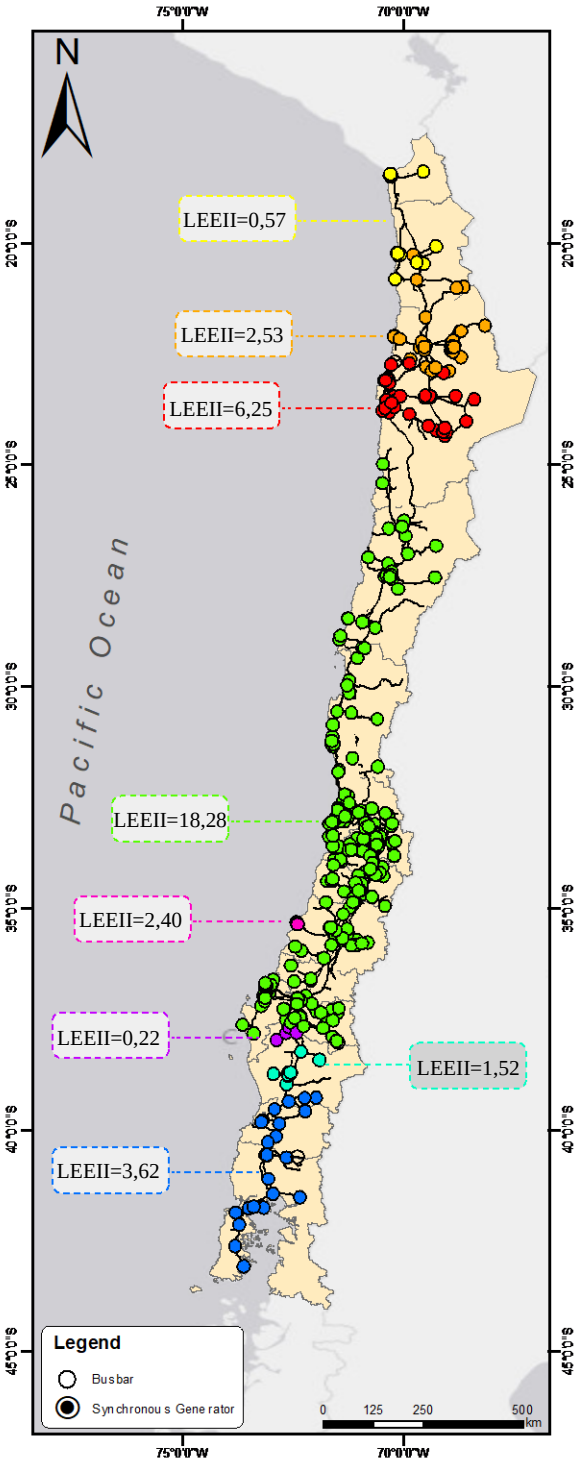

Figure 40: Stage 6 result: LEEII index for oc_1.

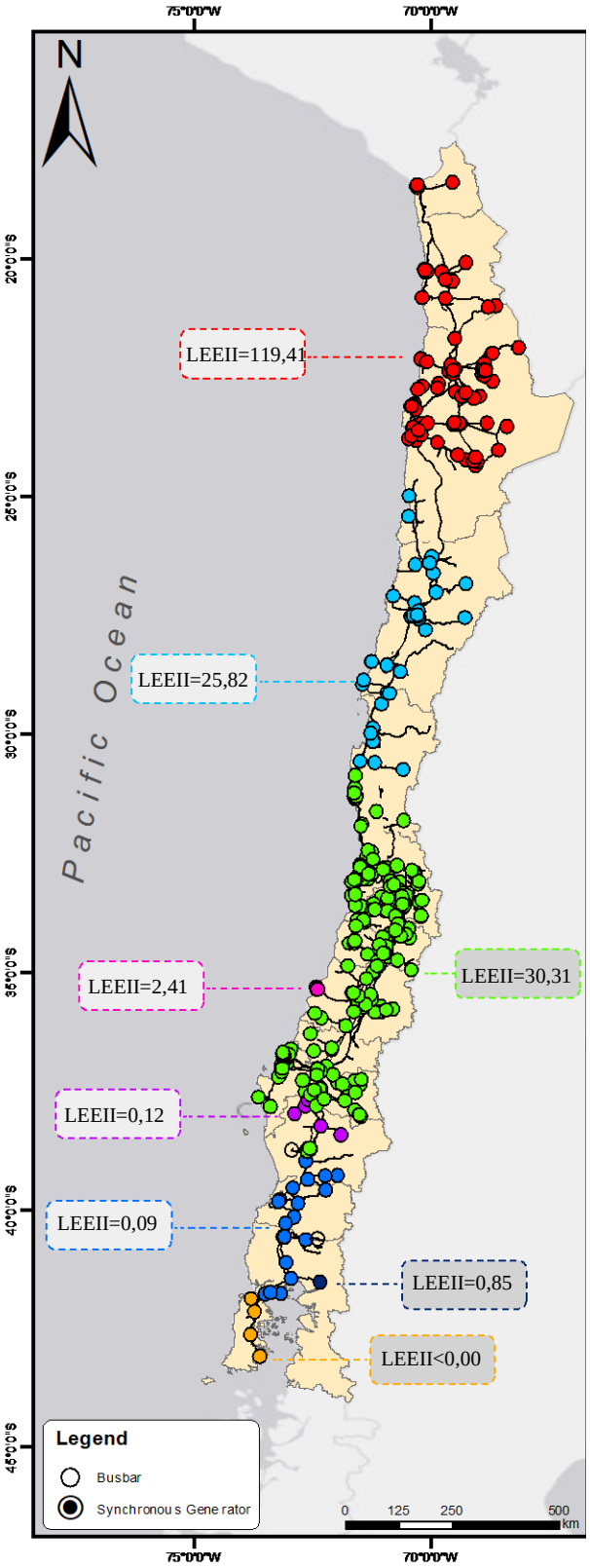

Figure 41: Stage 6 result: LEEII index for oc_2.

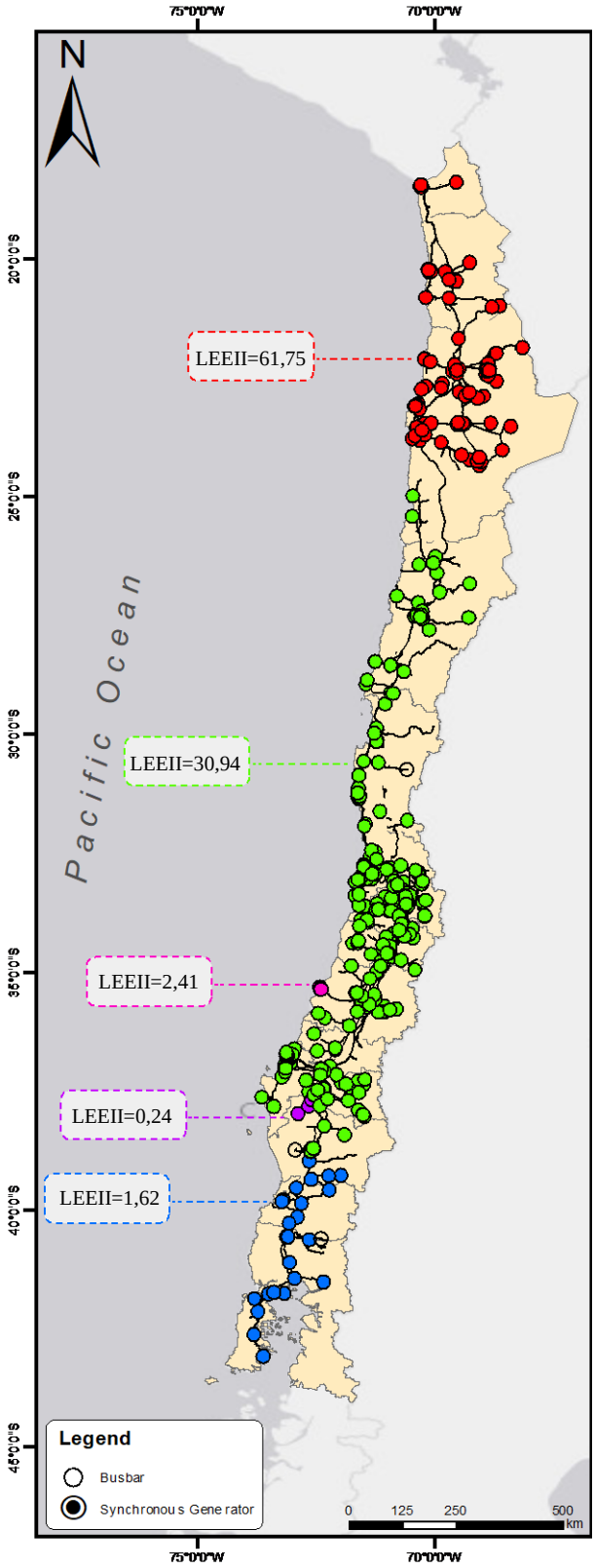

Figure 42: Stage 6 result: LEEII index for oc_3.

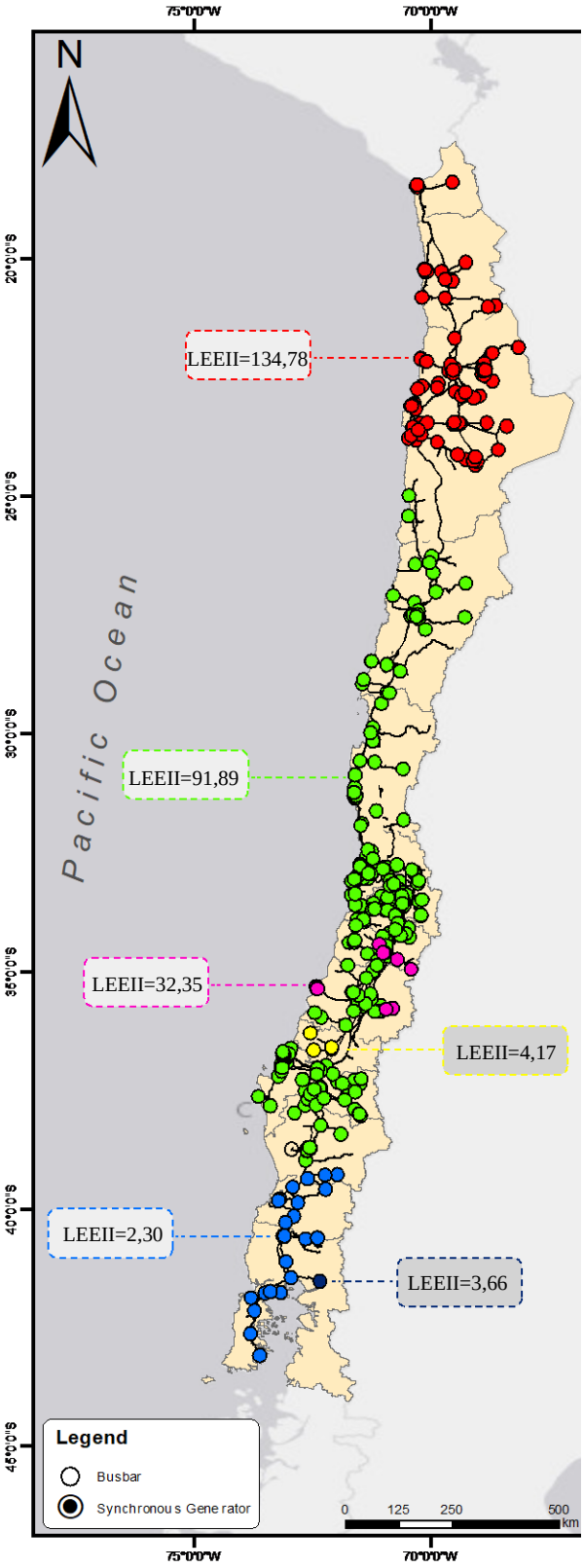

Figure 43: Stage 6 result: LEEII index for oc_4.

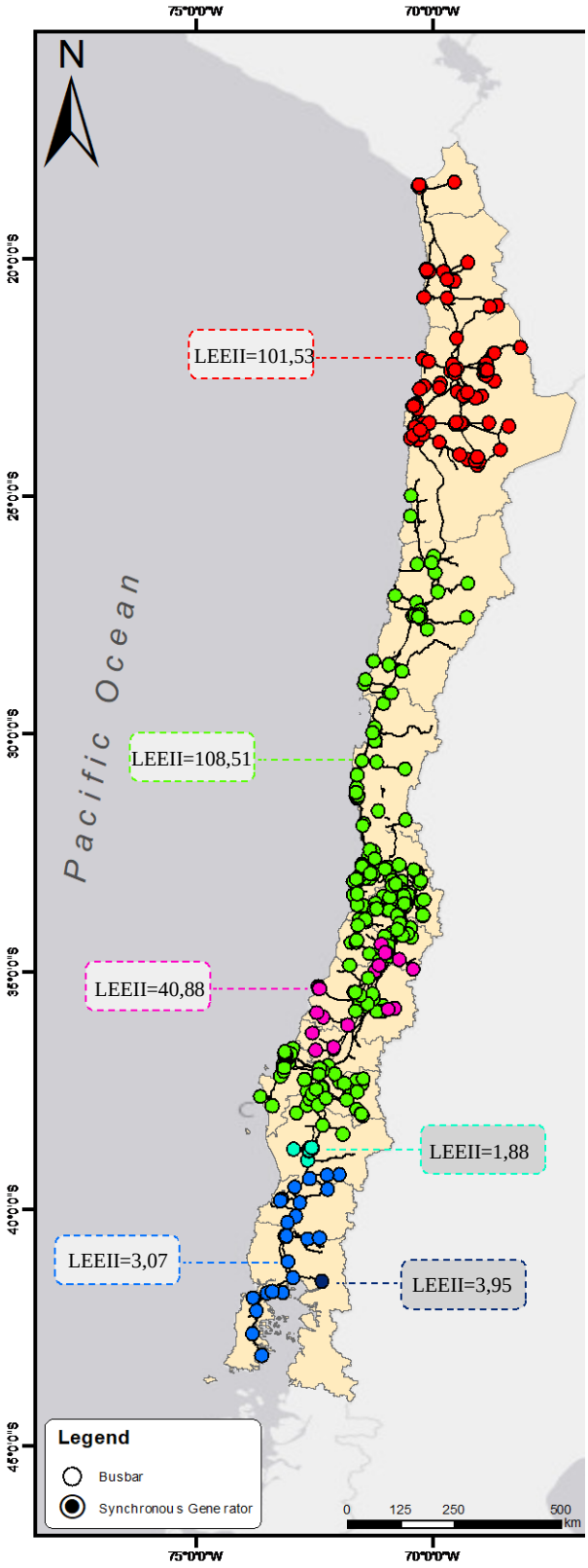

Figure 44: Stage 6 result: LEEII index for oc_5

5.2 Tool validation

This section is focused on validating the performance of the proposed offline tool. For this purpose, a dynamic study of the validating operating condition oc_6 is considered, consisting of a set of simulations of the worst possible generator outages events. For each dynamic simulation, the frequency deviation $\Delta f_{k_{cc_j}^{oc_i}}$ from the nominal value of each online SG k is recorded. While Figure 45 shows the geographic locations of the generation outages, Table 15 presents the dispatched active power of each suddenly disconnected SG.

SG outaged name	Active Power (MW)
01_Alfalfal 2 N°1	112,7
12_Las Lajas N°1	114,3
ANG1	104,7
Angostura U1	81,0
Antuco U2	72,7
CCH1	117,6
Canutillar U1	53,4
Guacolda U3	113,4
Guacolda U5	37,1
IEM	158,9
Pangue U1	109,6
Pehuenche U1	162,2
San Isidro U2 TG	220,1
Ventanas U2	87,9

Table 15: Power dispatched for each generation outage in MW.

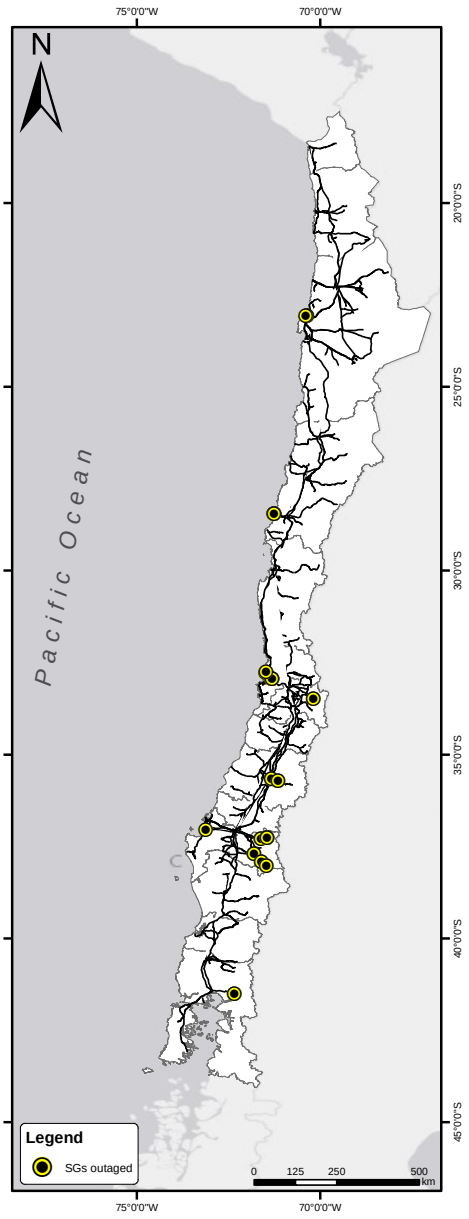

Figure 45: Locations of the generation outages simulated.

Then, it is required to fast-calculate the LEEII index for the validating operating condition oc_6, thus emulating the operation of the proposed tool, i.e., automatically assessing the f-robustness of the BPS (considering the spatial distribution of the inertia) from the unit commitment (see Figure

18). Then, the performance of the calculated LEEII index is evaluated, verifying that it accurately represents the spatial distribution of the inertia, and therefore, it explains the differences in local phenomena described in section 3.6: weaker areas exhibit worse frequency dynamics after a sudden ΔP contingency in terms of their local RoCoF and the amplitude of frequency oscillations:

- A high LEEII index leads to a low local RoCoF, i.e., close to zero.
- A high LEEII index leads to local frequency oscillations with low amplitude.

Automatically fast calculating the LEEII index from the unit commitment requires not executing stages 1 to 5. In other words, the process described for identifying coherent generators and coherent f-areas is not done. In this case, **the coherency map is taken directly from the most similar training operating condition**, whose results are previously stored in the tool. The criterion to determine which training operating condition is the most similar is **the one that has the closer net demand**.

Once the closest training operating condition has been selected, the LEEII is calculated for each f-area using equations (52) and (53), which require:

- Coefficients $\tilde{c}_x^{\,b}$, which are taken directly from stage 5.
- Mean inertias for each group of coherent generators $\bar{H}_{cg_x^{oc_i}}$, which are taken directly from stage 4. If there is not a SG present due to dispatch differences in the closest training operating condition, i.e., the coherent group of a SG is unknown, it is assigned to the group that its Point of Interconnection (POI) busbar belongs.

In the case of the oc_6, note that the closest training operating condition is the oc_1 according to the net demand (see Table 4), therefore, oc_6 inherits both the results of the layouts and coherency map from the oc_1. The results of the LEEII index and the mean coefficients of equation (52) are shown in Table 16:

	Mean Coefficient[9]								LEEII (pu @100 MVA)
F-area[9]	$\bar{c}_{ca_0}$	$\bar{c}_{ca_{11}}$	$\bar{c}_{ca_{12}}$	$\bar{c}_{ca_{13}}$	$\bar{c}_{ca_{15}}$	$\bar{c}_{ca_2}$	$\bar{c}_{ca_3}$	$\bar{c}_{ca_7}$	
ca_0	**0,94**	0,01	0,03	0,00	0,00	0,00	0,01	0,00	36,69
ca_{11}	0,23	**0,53**	0,00	0,00	0,00	0,00	0,01	0,23	0,36
ca_{12}	0,06	0,00	**0,68**	0,20	0,06	0,00	0,00	0,00	6,85
ca_{13}	0,03	0,00	0,28	**0,52**	0,17	0,00	0,00	0,00	2,75
ca_{15}	0,01	0,00	0,14	0,24	**0,61**	0,00	0,00	0,00	0,57
ca_2	0,10	0,00	0,00	0,00	0,00	**0,90**	0,00	0,00	2,41
ca_3	0,24	0,01	0,00	0,00	0,00	0,00	**0,75**	0,00	0,22
ca_7	0,06	0,14	0,00	0,00	0,00	0,00	0,00	**0,80**	1,93

Table 16: Resulting LEEII index and mean coefficients for each area in oc_6.

[9] As all ca_x and $\bar{c}_{ca_x}$ correspond to the same operating condition oc_6, superscript is omitted for simplicity.

As expected, the results are very similar to the oc_1. The mean coefficients are the same, and the LEEII index slightly vary, mainly in ca_0 and ca_7 due to some differences in the unit commitment. This result shows the effectiveness of the criterion selected to determine the most similar operating condition, the net demand, to fast-calculate the LEEII index and improve the practical feasibility of the offline tool proposed. The results are illustrated in Figure 46, where the total inertia of each f-area is also included:

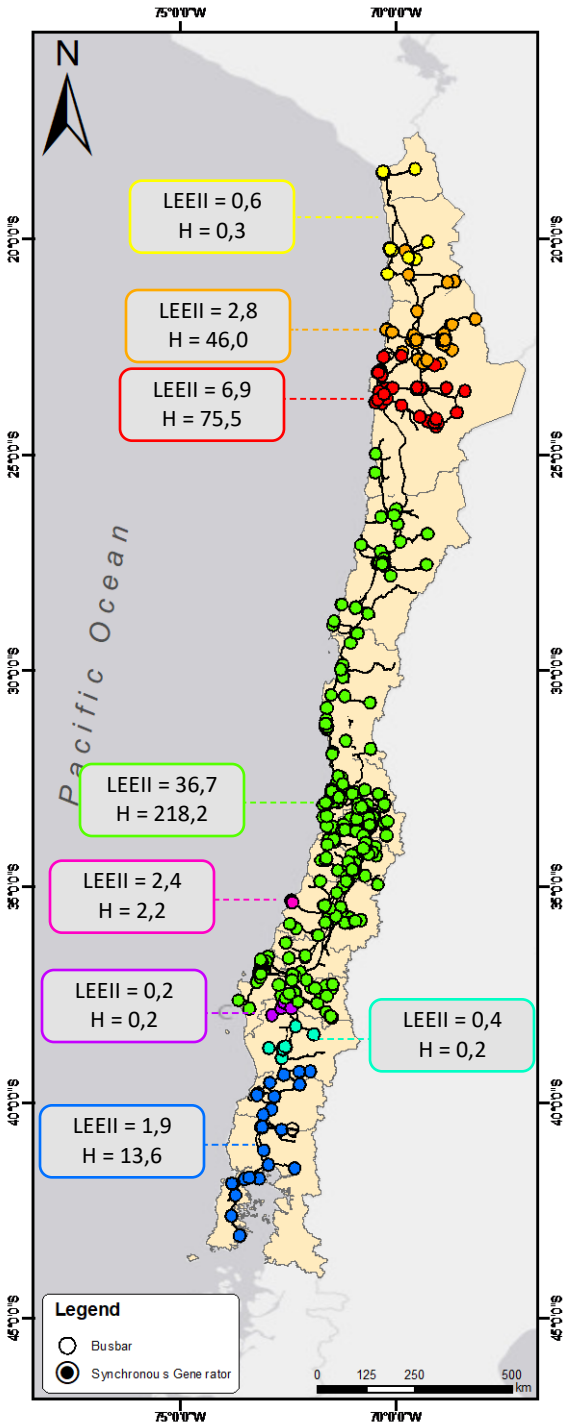

Figure 46: Stage 4 result: LEEII index for oc_6.

Once previous results are obtained, the local COI-based frequency of all the f-areas is recorded. Then, the worst results among the response of all the f-areas in terms of local RoCoF and the amplitude of local frequency oscillations are obtained and compared with its corresponding LEEII index for each dynamic simulation[10]. The results for all contingencies are plotted together and shown in Figure 47 and Figure 48 for the local RoCoF and local frequency oscillations, respectively. Each graph point represents a single dynamic simulation and is colored according to the f-area where the imbalance event occurs.

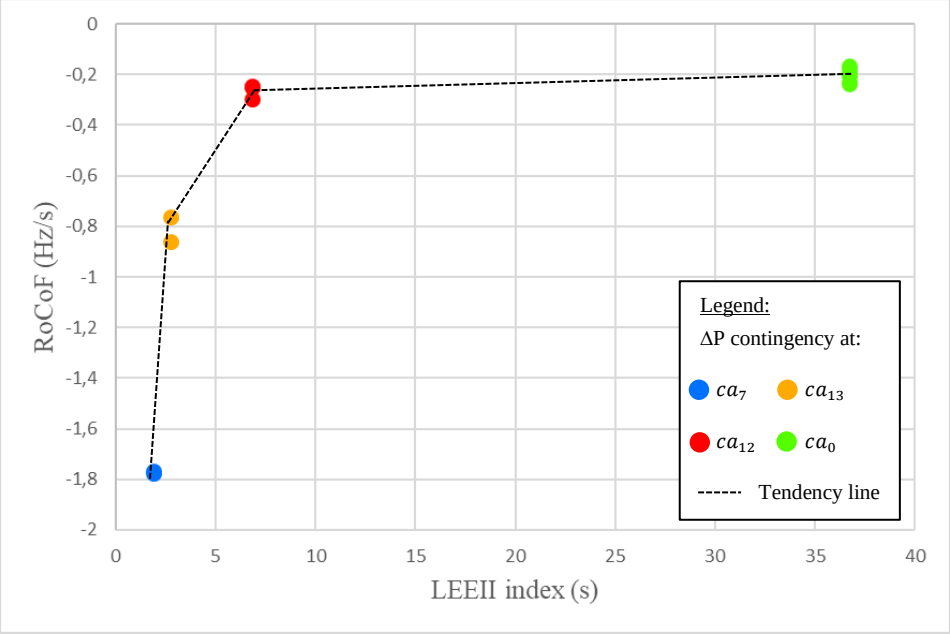

Figure 47: Validation results: LEEII index v/s Local RoCoF.

[10] Since simulated events involved different ΔP imbalance magnitudes (see Table 15), the results are normalized by a power base of 100 MW.

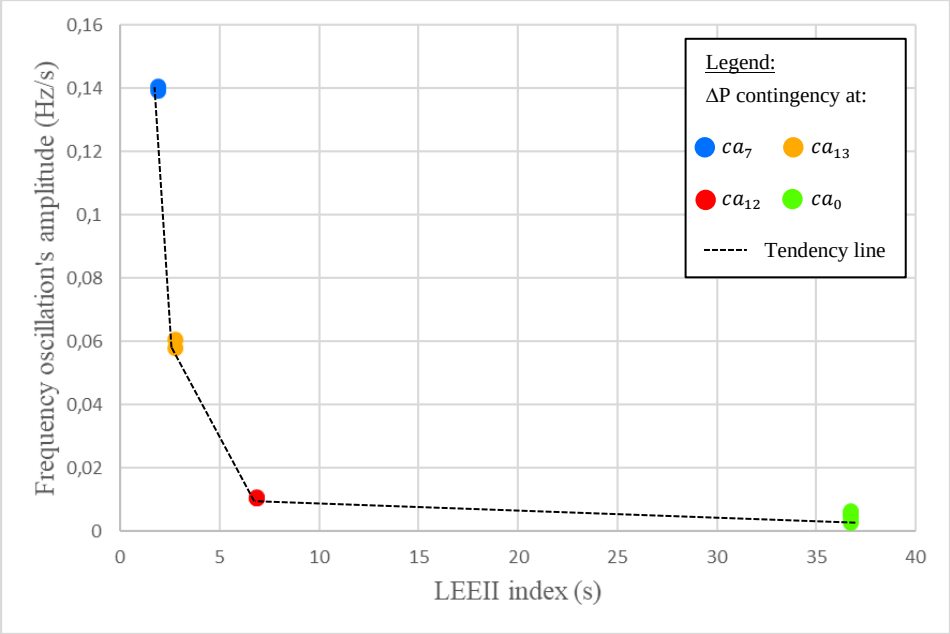

Figure 48: Validation results: LEEII index v/s Frequency oscillation's amplitude.

From Figure 47, it is clear to note a relationship between the LEEII index and the local RoCoF as expected: a weak f-area (low index) shows a more negative RoCoF than stronger f-areas (high index). It is worth noting that this relationship is not linear. In fact, beyond a specific value of the LEEII, a similar dynamic response is obtained despite a significant increment in the proposed index. This result suggests that a definition of a minimum threshold of LEEII index for f-areas could be a suitable solution to warn weak conditions. In contrast, interpolating a mathematical function that relates the LEEII index and the expected RoCoF is also possible but appears to be less appropriate than establishing a threshold due to the saturation of the relationship between both quantities.

Figure 48 also shows the proposed index's correct performance, where f-areas with a low LEEII index suffer higher local frequency oscillations than f-areas with a high LEEII index. The relationship shape is similar to the one obtained for local RoCoF, where the tendency saturates for a very high LEEII index.

Time-domain response of the COI-based frequency of the f-area where the ΔP continency is applied is shown in Figure 49 for 4 different ΔP contingencies, one for each f-area.

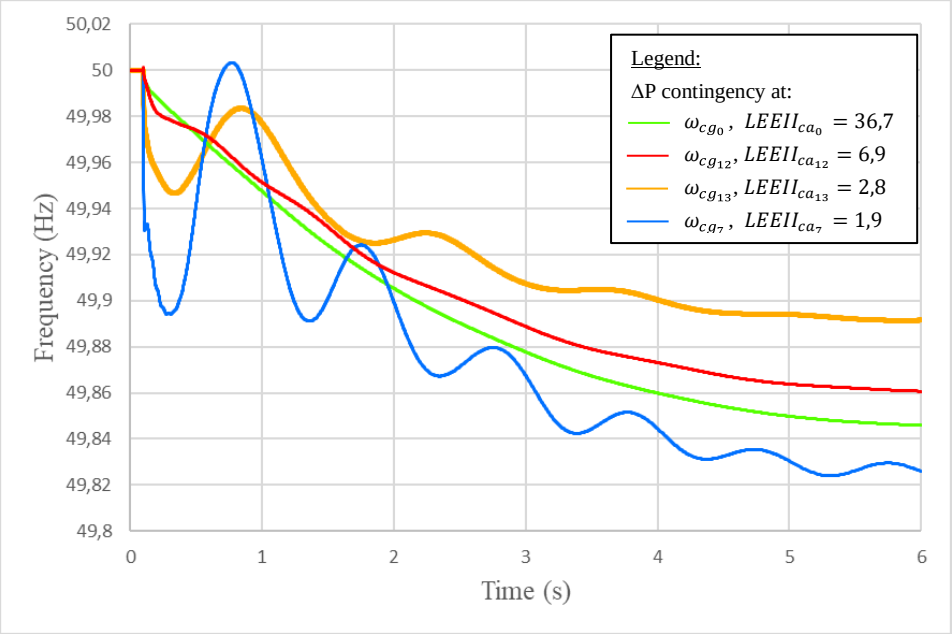

Figure 49: Validation results: Time response of the COI-based frequency for different ΔP contingencies at different f-areas.

The results shown in Figure 49 verify the correct performance of the LEEII index as an indicator of the dynamic frequency performance of f-areas during contingencies. Local frequency response is much worse in terms of RoCoF and the amplitude of oscillations in weak f-areas than in strong f-areas.

However, it is worth noting that the f-areas with a high LEEII index: ca_0 and ca_{12} with 36,7 s and 6,9 s, respectively, show a worse frequency Nadir than the weaker area ca_{13} with 2,8 s. This counterintuitive result arises because of that frequency Nadir depends not only on inertia and its spatial distribution (already represented through the proposed index) but also on primary frequency control. Therefore, to explain the frequency Nadir differences, further research is needed to define complementary novel indexes to represent how much, how fast, and from where the primary reserves are deployed.

Further details of the time domain response of the 4 different ΔP contingencies previously shown in Figure 49 are presented individually from Figure 50 to Figure 53. The COI-based frequency response of the 4 highlighted f-areas for each single simulation is included.

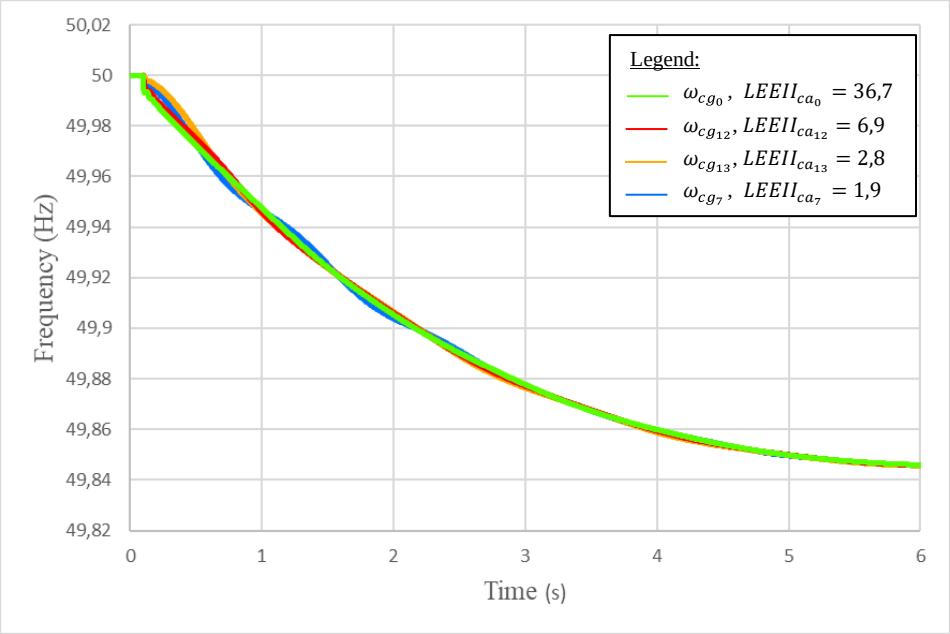

Figure 50: Validation results: Time-response of the COI-based frequency for 4 different f-areas | ΔP contingency at ca_0.

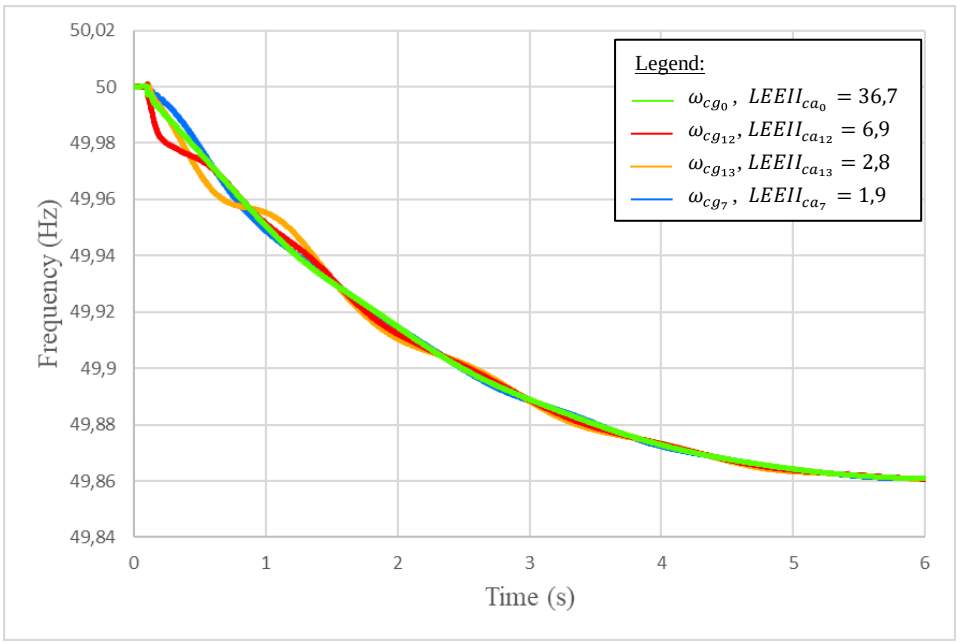

Figure 51: Validation results: Time-response of the COI-based frequency for 4 different f-areas | ΔP contingency at ca_{12}.

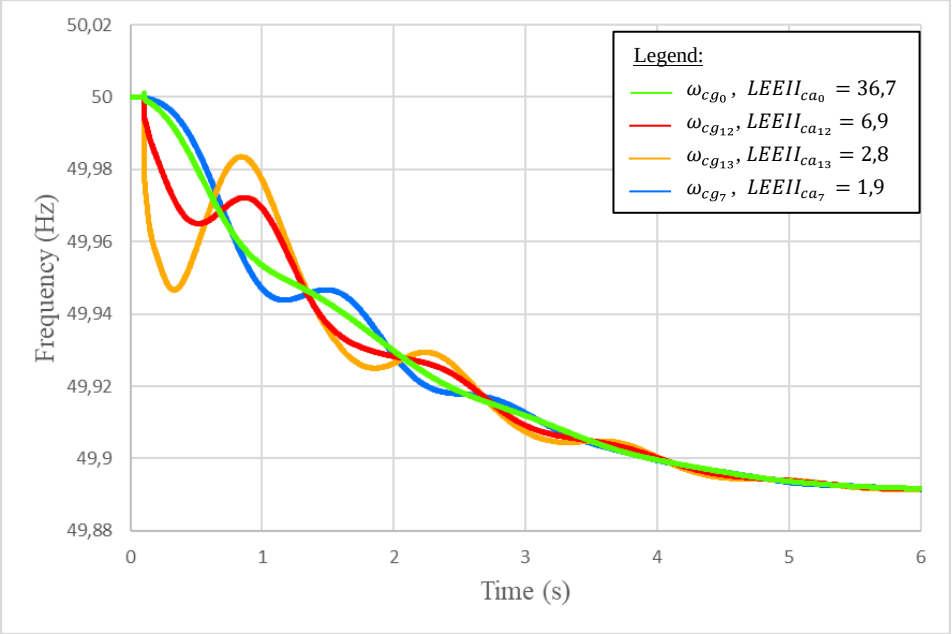

Figure 52: Validation results: Time-response of the COI-based frequency for 4 different f-areas | ΔP contingency at ca_{13}.

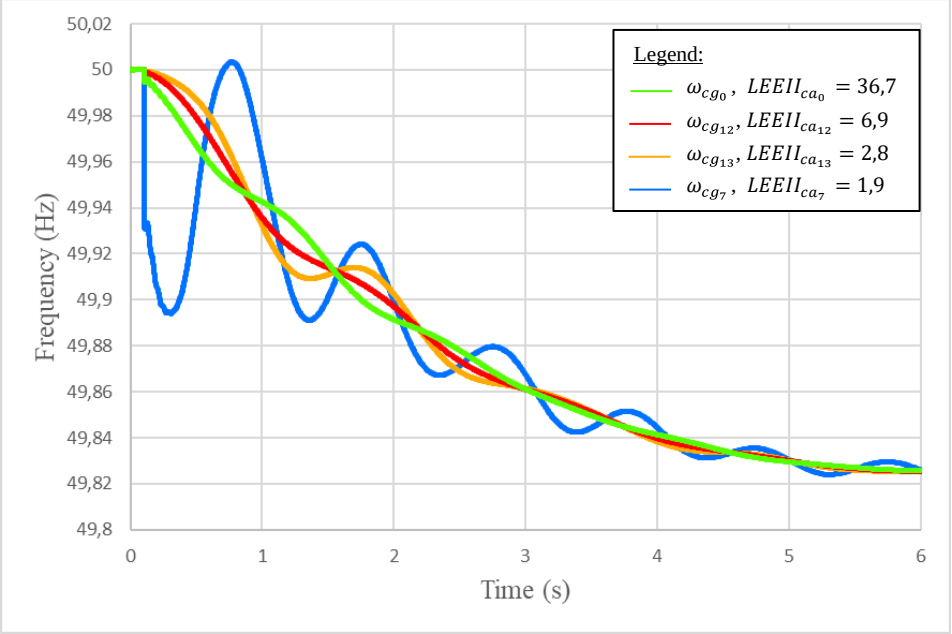

Figure 53: Validation results: Time-response of the COI-based frequency for 4 different f-areas | ΔP contingency at ca_7.

The results from Figure 50 to Figure 53 confirm the previously analyzed behavior: the system response after a sudden power imbalance is much worse in the case that it occurs in a f-area with a low LEEII index (see Figure 53) than in another one with high LEEII index (see Figure 50).

Furthermore, the frequency response of different f-areas is quite similar for a single simulation, where the more noticeable differences arise in the first seconds after the sudden power imbalance. Despite slight differences, it is remarkable that, in general, the LEEII index can explain these differences adequately. For instance, in Figure 50, where the ΔP contingency occurs at the ca_0, the strongest f-area, its COI-based frequency shows better performance (green curve) than weaker f-areas such as ca_7 (blue curve). A similar behavior can be observed in Figure 53, where

the ΔP contingency occurs at the ca_7, the weakest f-area. Again, ca_0 shows the better performance since it is the strongest f-area, and ca_{12}, ca_{13} and ca_7 show increasingly worse responses accordingly with their LEEII index values. However, specific exceptions arise in the results of Figure 51 and Figure 52, where ca_7, the weakest f-area, show a slightly better performance than ca_{12} and ca_{13}, which have a higher LEEII index. The reason for this lies in the enormous distance from the event locations, both in the North region of the Chilean NES, to the ca_7, which is the southernmost f-area of the system. Thousands of kilometers cause that active losses in the transmission system, which are neglected in the LEEII index calculation, are enough to attenuate the effects of the ΔP imbalance on ca_7, thus leading to this exceptions.

Once the expected relationship between the proposed LEEII index and the objective local frequency phenomena has been verified, general insights to derive sufficient conditions by which power systems can fall into undesirable activation of protections in terms of the novel index defined are presented in the following based on international thresholds. In particular, the minimum RoCoF required before generation facilities are allowed to trigger their installations to protect their equipment is presented in Figure 54. Note that validation results previously presented in Figure 47 are also included in Figure 54 but without coloring by f-area.

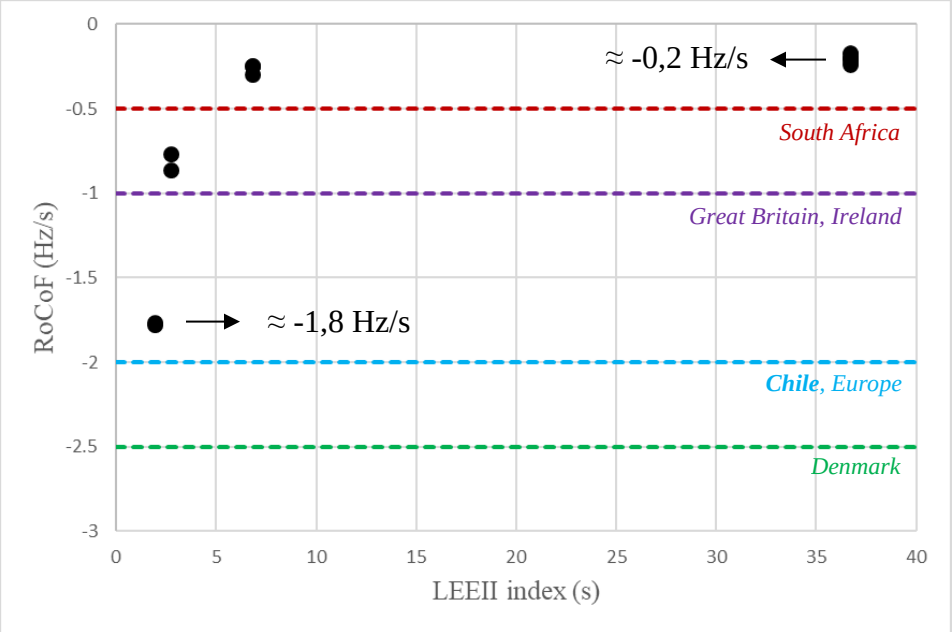

Figure 54: Validation results: LEEII index v/s Local RoCoF and comparison of international RoCoF thresholds.

South Africa's power system holds the more restrictive RoCoF threshold since it has a huge synchronous generation presence and, therefore, high amounts of inertia. In consequence, RoCoF values less than -0,5 Hz/s are already considered critical [41]. Great Britain and Ireland hold a -1 Hz/s RoCoF requirement. In particular, Ireland has changed its regulation from a previous value of -0,125 Hz/s due to a consistent reduction of the system's inertia caused by a continuous replacement of fuel-based synchronous generation with CIGTs [41][42]. Chile's regulation shares a -2 Hz/s threshold with most ENTSO-E's TSOs. Finally, Denmark holds a more permissive value because of the massive penetration of CIGTs in their energy matrix that involves less system inertia.

From Figure 54, it is remarkable to note the wide range of the local RoCoF differences obtained depending on the f-robustness of each f-area. They vary from -1,8 Hz/s to -0,2 Hz/s for a

100 MW ΔP contingency. This range becomes highly relevant when comparing the different international thresholds, i.e., while the system can cleanly ride through a ΔP contingency that occurs in a strong f-area, a power imbalance of the same amount can lead to undesirable activation of RoCoF relays in the case it occurs in a weak f-area. This result verifies that the total inertia of power systems is not enough as an indicator of f-robustness since it can not warn local frequency differences and thus identify local f-areas.

In the case of the Chilean NES, even though it seems that no ΔP contingency leads to an activation of RoCoF protections, consider that the results presented in Figure 54 are normalized to a 100 MW power unbalance. Several generation facilities with an installed capacity above that power may fail and provoke more critical local RoCoF values. Furthermore, it is expected that as the system weakens in the future, these problems will become more critical and arise more frequently. In such a scenario, the development of novel solutions and proper regulations to guarantee a minimum level of f-robustness are required. In this work, it has been proved that only considering the total inertia is insufficient, but a complete approach capable of identifying weak f-areas is required instead. The LEEII index has been validated as a valuable indicator to face this challenge, and the proposed tool has proven its feasibility to be essential for successfully overcoming the issues studied.

6 Conclusions

6.1 Conclusions

This thesis proposes a novel offline tool to identify weak areas in low inertia power systems with high shares of converter-based generation. The investigation objectives have been met, and the different hypothesis has been verified.

This research involved a comprehensive review of the state of the art regarding frequency robustness in CIGTs-dominated power systems and several challenges in low-inertia power systems. In particular, the investigation focused on recent works that have shown that the spatial distribution of the inertia strongly influences the post-fault local frequency dynamics and not just the total inertia of the system. Weak f-areas are characterized by a more critical local RoCoF and higher local frequency oscillations after a sudden ΔP contingency. In this context, some recent publications have proposed different methods to assess the spatial distribution of inertia. However, they are focused on providing a first approach based on specific theoretical developments that have been tested in small academic systems. The lack of a complete definition of a feasible and validated tool to identify weak f-areas motivated the definition of the objectives and the hypothesis in this thesis.

The proposed solution consists of an offline tool capable of automatically identifying weak f-areas. A six-stage methodology was successfully implemented to develop the proposed tool in a real power system case: the Chilean NES. The development involves first identifying coherent f-areas and then quantifying its f-robustness level through the novel LEEII index that considers the spatial distribution of the inertia and the effect and interactions of neighbor areas. Six representative operating conditions that represent worst-case scenarios from a frequency stability perspective were considered, where five of them were used to develop the proposed tool, and the sixth was used to validate its performance.

Several ΔP contingencies were simulated in a detailed dynamic model of the Chilean NES. The results showed significant differences in the local frequency performance of different f-areas, thus verifying that power systems' total inertia is insufficient as an indicator of frequency performance during contingencies. In consequence, hypothesis **H1** has been verified.

The operation of the proposed offline tool was emulated for one critical operating condition. Based on the system state information, weak frequency areas were quickly obtained by fast calculating the LEEII index. Thus, specific objective **S03** has been met. Then, the results of the LEEII index were compared with the results of several ΔP contingencies, and its performance has been validated since it can adequately quantify local f-robustness and identify weak f-areas of the system in terms of the objective local phenomena. F-areas with lower LEEII index values are exposed to a more critical RoCoF and higher local oscillations. Consequently, hypothesis **H2** has been verified, and specific objectives **SO1** and **SO4** have been met.

Sufficient conditions by which the power system can fall into undesirable activation of protections were derived from the proposed LEEII index. General insights were provided based on international thresholds, where Chilean regulation states a minimum required RoCoF of -2 Hz/s before generation facilities are allowed to trigger their equipment. If a sudden ΔP contingency occurs in a weak f-area with a LEEII index lower than 5 s, the event may lead to undesirable activation of RoCoF relays. Consequently, it is recommended to guarantee a minimum value of 5 s to avoid the analyzed issues. Thus, specific objective **SO2** has been met.

Finally, the proposed offline tool has been validated as a screening method to identify weak f-areas in low inertia power systems, thus achieving this investigation's general objective (GO). The solution supports the monitoring of the system state in daily operation, providing the TSOs a helpful tool to face one of the challenges that arise in CIGTs-dominated power systems, which will be key to securing the grid's stability in the future.

6.2 Future Work

Even though this thesis has made a significant contribution providing a first complete approach to identify weak f-areas, further investigation can be carried out to develop novel solutions to face the critical security task of analyzing and quantifying the f-robustness level of CIGTs-dominated power systems. General guidelines of different future research work opportunities are presented in the following.

The proposed LEEII index only considers the inertia coming from SGs and its spatial distribution throughout the grid. However, as the system weakens, TSOs tend to demand FFR contribution from CIGTs. Therefore, a way to incorporate it to determine the f-robustness level for each f-area arises as a relevant aspect to analyze.

This work has made significant advances to explain local frequency differences during the inertial response, i.e., more critical RoCoF and higher frequency oscillations. Both phenomena depend mainly on inertia and its spatial distribution, accurately quantified through the proposed LEEII index. However, to fully determine the power system’s f-robustness, further investigation is needed to define novel complementary indexes to assess the performance of the primary frequency control, considering the spatial distribution of the reserves. This approach would allow explaining frequency Nadir differences depending on the ΔP contingency location, which may be critical to prevent the activation of Under-Frequency Load Shedding Schemes (UFLSSs).

This work has proposed an offline tool to support the short-term operation planning as a security check for the TSO. However, an online identification of weak f-areas can also be valuable for the TSO supporting the real-time monitoring of the system’s conditions. In this case, the solution has to take into account information from the WAMS network and automatically compute novel indexes to identify weak f-areas quickly.

Finally, different approaches could be interesting to implement and compare their performances with the proposed tool. For instance, an AI-based offline tool based on the system state information directly predicts the RoCoF that a certain weak f-area of the system may experience if a sudden ΔP occurs, instead of calculating an indicator of the f-robustness. It is important to note that this kind of solution has some limitations. On the one hand, they require a vast dataset to successfully carry out the learning process, which may be challenging due to the limitations on the execution of dynamic simulations. On the other hand, it is critical to define a way to adapt the tool since the continuous topological changes could make the solution obsolete quickly.

7 Bibliography

[1] Solar Energy Data, Installed Capacity Trends. 2022. International Renewable Energy Agency (IRENA). [online] Available at: https://public.tableau.com/shared/WHQK3R258?:toolbar=n&:display_count=n&:origin=viz_share_link&:embed=y [Accessed 08 January 2022].

[2] Wind Energy Data, Installed Capacity Trends. 2022. International Renewable Energy Agency (IRENA). [online] Available at: https://public.tableau.com/shared/BN6J9YPC3?:toolbar=n&:display_count=n&:origin=viz_share_link&:embed=y [Accessed 08 January 2022].

[3] F. Milano, F. Dörfler, G. Hug, D. J. Hill and G. Verbic, "Foundations and Challenges of Low-Inertia Systems (Invited Paper)", *2018 Power Systems Computation Conference (PSCC)*, pp. 1-25, 2018.

[4] P. Tielens and D. Van Hertem, "The relevance of inertia in power systems," *Renewable and Sustainable Energy Reviews*, vol. 55, 2016.

[5] IEEE/NERC Task Force on Short-Circuit and System Performance Impact of Inverter Based Generation, "Impact of Inverter Based Generation on Bulk Power System Dynamics and Short-Circuit Performance," IEEE Power & Energy Society, 2018.

[6] A. Ulbig, T. S. Borsche, and G. Andersson, "Impact of Low Rotational Inertia on Power System Stability and Operation," *Proceedings of the 19th IFAC World Congress*, 2014.

[7] D. Groß, S. Bolognani, B. K. Poolla, and F. Dörfler, "Increasing the resilience of low-inertia power systems by virtual inertia and damping," *IREP Bulk Power System Dynamics & Control Symposium*, 2017.

[8] B. Kroposki, "Achieving a 100 % Renewable Grid: Operating Electric Power Systems with Extremely High Levels of Variable Renewable Energy", "IEEE Power and Energy Magazine," vol. 15, n 2, pp. 61-73, 2017.

[9] G. Delille, B. Francois, and G. Malarange, "Dynamic Frequency Control Support by Energy Storage to Reduce the Impact of Wind and Solar Generation on Isolated Power System's Inertia," *IEEE Transactions on Sustainable Energy*, vol. 3, 2012.

[10] C. Rahmann and A. Castillo, "Fast Frequency Response Capability of Photovoltaic Power Plants: The Necessity of New Grid Requirements and Definitions," *Energies*, vol. 7, 2014.

[11] P. Kundur, N. J. Balu and M. G. Lauby, "Power system stability and control," vol 7, New York: McGraw-hill, 1994.

[12] L. Fan, "Control and Dynamics in Power Systems and Microgrids," New York, CRC Press, 2017.

[13] Norma Técnica de Seguridad y Calidad de Servicio (NTSyCS), Comisión Nacional de Energía (CNE), Chile, 2014.

[14] RG-CE System Protection & Dynamics Sub Group, "Frequency stability evaluation criteria for the synchronous zone of continental Europe," ENTSO-E, Tech, Rep., 2016. Svenska Kraftnät, Statnett, Fingrid and Energinet.dk, “Challenges and Opportunitiesfor the Nordic Power System”, Tech. Rep., 2016.

[15] System Protection & Dynamics Sub Group, "Dispersed generation impact on CE regionsecurity," ENTSO-E, Tech. Rep., 2014.

[16] J. Beerten, O. Gomis-Bellmunt, X. Guillaud, J. Rimez, A. van der Meer and D. Van Hertem, "Modelling and control of HVDC grids: a key challenge for the future power system," *Power Systems Computation Conference (PSCC*, Wroclaw, Poland, 2014.

[17] C. Rahmann, J. Vega and F. Valencia, "Validity Range of Fundamental Frequency Simulations under High Levels of Variable Generation Technologies," *IREP 10th Bulk Power Systems Dynamics and Control Symposium*, 2017.

[18] B. Alinezhad, G. A. Taylor, O. Bronckart, J. Maricq, and M. Bradley, "Impact of Inertia Distribution on Power System Stability and Operation," *2019 IEEE Milan PowerTech*, Milan, Italy, pp. 1-6, 2019.

[19] Adrees, J. V. Milanovic and P. Mancarella, "Effect of inertia heterogeneity on frequency dynamics of low-inertia power systems," *IET Generation, Transmission & Distribution*, vol. 13, n 14, pp 2951-2958, 2019.

[20] IEC 61400-27-1 Ed. 1: "Wind turbines – part 27-1: electrical simulation models – wind turbines", February 2015.

[21] M. Dreidy, H. Mokhlis, and S. Mekhilef, "Inertia response and frequency control techniques for renewable energy sources: A review," *Renewable and Sustainable Energy Reviews*,vol. 69, 2017.

[22] Y. Sun, Z. Zhang, G. Li, and J. Lin, "Review on frequency control of power systems withwind power penetration," *2010 International Conference on Power System Technology*, pp.1-8, 2010.

[23] F. Diaz-Gonzalez, M. Hau, A. Sumper and O. Gomis-Bellmut, "Participation of wind power plants in system frequency control: Review of grid code requirements and control methods," *Renewable and Sustainable Energy Reviews*, vol. 34, pp. 551-564, 2014.

[24] Fernandez, E. Gomez, E. Muljadi and A. Molina, "Power systems with high renewableenergy sources: A review of inertia and frequency control strategies over time," *Renewable and Sustainable Energy Reviews*, vol 115, 2019.

[25] Y. Xiao, X. Lin, and Y. Wen, "A Framework for Assessing the Inertia Distributionof Power Systems," *2019 IEEE 3rd Conference on Energy Internet and Energy System Integration (EI2)*, pp. 1418-1423, 2019.

[26] F. Zeng, Z. Zhang, Y. Zhou, and S. Qu, "Online Identification of Inertia Distributionin Normal Operating Power System," *IEEE Transactions on Power Systems*, vol. 35, n 4, 2020.

[27] F. Milano and Á. Ortega, "Frequency divider," *IEEE Transactions on Power Systems*, vol 33, n 6, pp. 7249-7257, 2018.

[28] H. Pulgar-Painemal, Y. Wang and H. Silva-Saravia, "On Inertia Distribution, Inter-Area Oscillations, and Location of Electronically-Interfaced Resources," *IEEE Transactions on Power Systems*, vol. 33, n 1, pp. 995-1003, 2018.

[29] Y. Wang, H. Silva-Saravia and H. Pulgar-Painemal, "Estimating inertia distribution to enhance power system dynamics," North American Power Symposium (NAPS), pp. 1-6, 2017.

[30] H. A. Alsafih and R. W. Dunn, "Determination of coherent clusters in a multi-machine power system based on wide-area signal measurements," IEEE PES General Meeting, pp. 1-8, 2010.

[31] O. Oded and L. Rokach, "Clustering methods," Data Mining and Knowledge Discovery Handbook, pp. 321-352, 2006.

[32] F. Nielsen, "Hierarchical Clustering," Introduction to HPC with MPI for Data Science, pp. 195-211, 2016.

[33] E. Allen and I. Marija, "Price-Based Commitment Decisions in the Electricity Market", 1 ed., London: Springer-Verlag London, 1999.

[34] Y. Dvorkin, P. Henneaux, D. Kirschen and H. Pandžić, "Optimizing Primary Response in Preventive Security-Constrained Optimal Power Flow", IEEE Syst. J. pp. 414-423, 2018.

[35] C. Rahmann, D. Ortiz-Villalba, R. Álvarez and M. Salles, "Methodology for Selecting Contingencies for Frequency Stability Studies", 2017 IEEE Power & Energy Society General Meeting, pp. 1-5, 2017.

[36] D. Ortiz-Villalba, C. Rahmann, R. Álvarez, C. A. Canizares and C. Strunck, "Practical Framework for Frequency Stability Studies in Power Systems with Renewable Energy Sources", IEEE Access, pp. 202286-202297, 2020.

[37] Comisión Nacional de Energía (CNE), "Se concreta la Interconexión de los sistemas eléctricos SIC y SING con la presencia de la Presidenta de la República". 2017. [online] Available at: https://www.cne.cl/prensa/prensa-2017/11-noviembre-2017/se-concreta-la-interconexion-de-los-sistemas-electricos-sic-y-sing-con-la-presencia-de-la-presidenta-de-la-republica/ [Accessed 13 March 2022]

[38] Coordinador Eléctrico Nacional (CEN), "Sistema Eléctrico Nacional" . 2022. [online] Available at: https://www.coordinador.cl/sistema-electrico/ [Accessed 13 March 2022]

[39] Ministerio de Energía del Gobierno de Chile, “Estrategia de Descarbonización: Retiro y/o Reconversión de Unidades a Carbón”. 2020. [online] Available at: https://www.energia.gob.cl/sites/default/files/folleto_estrategia_descarbonizacion_cast.pdf [Accessed 13 March 2022]

[40] Coordinador Eléctrico Nacional (CEN), “Base de datos PowerFactory DIgSILENT”. 2021. [online] Available at: https://www.coordinador.cl/operacion/documentos/modelacion-del-sen/modelos-digsilent/base-de-datos-digsilent/ [Accessed 20 November 2021]

[41] Power Planning Associates Limited (PPA Energy), “Rate of Change of Frequency (ROCOF) Review of TSO and Generator Submissions, Final Report”, Guildford, United Kingdom (UK), Tech, 2013.

[42] Q. Hong, M. A. U. Khan, C. Henderson, A. Egea-Álvarez, D. Tzelepis and C. Booth, “Addressing Frequency Control Challenges in Future Low-Inertia Power Systems: A Great Britain Perspective”, Engineering, pp.1057-1063, 2021.